CURRENT STATUS OF MODELING LEAN EXHAUST GAS AFTERTREATMENT CATALYSTS

Anke Güthenke[1,*], Daniel Chatterjee[1], Michel Weibel[1], Bernd Krutzsch[1], Petr Kočí[2], Miloš Marek[2], Isabella Nova[3] and Enrico Tronconi[3]

[1]Daimler AG, Department GR/VPE, 70546 Stuttgart, Germany

[2]Institute of Chemical Technology at Prague, Department of Chemical Engineering, CZ 166 28 Prague, Czech Republic

[3]Dipartimento di Chimica, Materiali e Ingegneria Chimica "G. Natta", Politecnico di Milano, Milan I-20133, Italy

---

*Corresponding author. Tel.: +49 711 17 21911; Fax: +49 711 3052 158 692.
E-mail: anke.guethenke@daimler.com

Advances in Chemical Engineering, vol. 33
ISSN 0065-2377
DOI 10.1016/S0065-2377(07)33003-2

Abstract

Decreasing emission limits lead to the development of combined aftertreatment systems, consisting of combinations of different catalyst technologies and particulate filters. Modeling such systems can contribute considerably in reducing development time and cost. The methodology for developing catalyst models is reviewed and models for the diesel oxidation catalyst (DOC) with hydrocarbon (HC) adsorption, the NO_x storage and reduction catalyst (NSRC) and the urea–selective catalytic reduction system (urea–SCR) are developed. Applications for exhaust aftertreatment system modeling are shown.

I. Introduction

Worldwide emission legislation has become increasingly stringent over the last years. European emission limits for passenger cars and heavy-duty trucks are displayed in Figs. 1 and 2, respectively. For passenger cars, the final values and date for EU V are still under discussion.

For heavy-duty trucks, since 2000, particulate emissions have been reduced by 80%, NO_x will be reduced by 60% in 2008 with EU V. A further reduction of emission limits with EU VI is being considered for 2013 (Schulte-Braucks, 2006).

In the USA, for Tier 2 emission limits different bins have been defined. Passenger cars are certified in any of the available bins by choice of the vehicle manufacturer. With full implementation in 2009, the average NO_x emission of the entire light-duty fleet sold by each manufacturer must meet 0.07 g/mile. For the individual bins, the full useful life emission limits are displayed in Table I. The very strict California low emission vehicle (LEV) II emission standards are covered in the lower number bins to make certification easier for vehicle manufacturers.

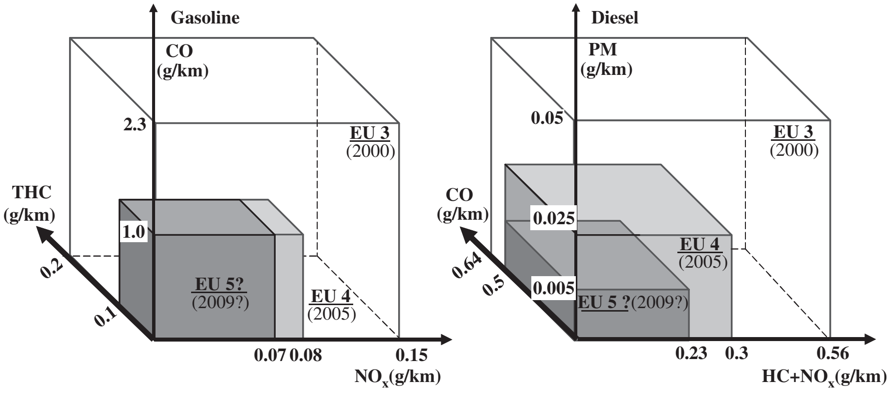

FIG. 1. European emission legislation for passenger cars (Dieselnet, 2007).

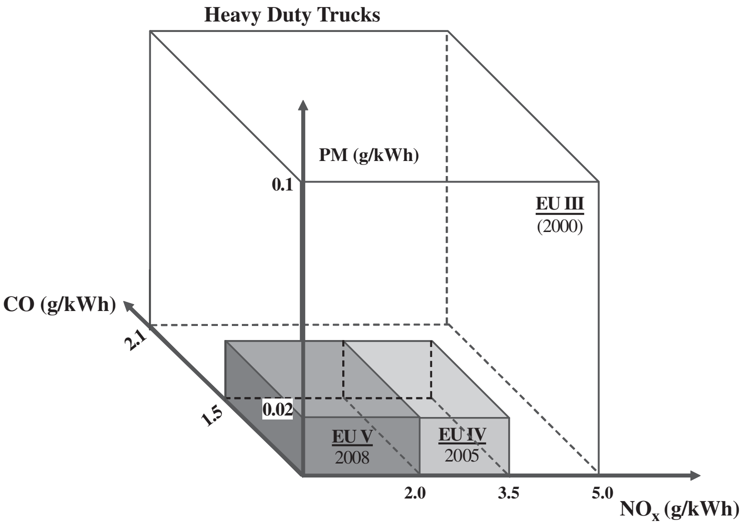

FIG. 2. European emission legislation for heavy-duty trucks—ESC limits (Dieselnet, 2007).

For heavy-duty trucks, US07 legislation demands particulate matter (PM) below 0.01 g/bhp-hr (grams per brake horsepower-hour), NO_x below 0.20 g/bhp-hr and non-methane hydrocarbon (NMHC) below 0.14 g/bhp-hr. The NO_x and NMHC limits will be phased in for diesel engines between 2007 and 2010, based on a percentage of vehicle sales. Additionally, not-to-exceed values of 1.5 times the emission limits are defined, which have to be met for a very large range of engine operating conditions.

Test cycles differ widely for European and US legislation and also for passenger cars and commercial vehicles. For European passenger car

TABLE I

US EPA Passenger Car Tier 2 Emission Standards (Dieselnet, 2007)

Bin	Full useful life				
	NMOG[a](g/mile)	CO (g/mile)	NO_x (g/mile)	PM (g/mile)	HCHO (g/mile)
8b	0.125	4.2	0.2	0.02	0.018
7	0.090	4.2	0.15	0.02	0.018
6	0.090	4.2	0.10	0.01	0.018
5	0.090	2.1	0.07	0.01	0.018
4	0.070	2.1	0.04	0.01	0.011
3	0.055	2.1	0.03	0.01	0.011
2	0.010	2.1	0.02	0.01	0.004
1	0.000	0.0	0.00	0.00	0.000

[a] For diesel fueled vehicle, NMOG (non-methane organic gases) means NMHC (non-methane hydrocarbons).

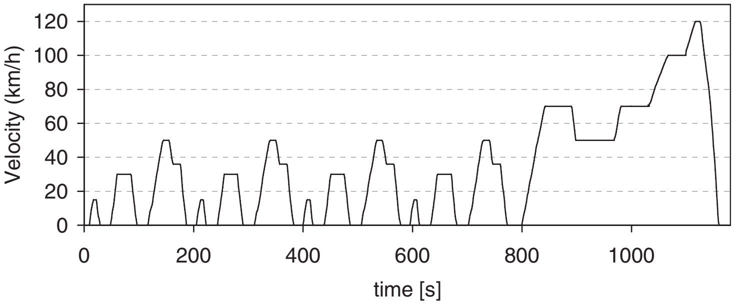

Fig. 3. NEDC—New European Driving Cycle (Dieselnet, 2007).

certification, the new European driving cycle (NEDC) is employed, which is also known as the MVEG-A cycle. Tested on a chassis dynamometer, it consists of four ECE segments to represent urban driving conditions, followed by one EUCD to account for extra urban conditions, as shown in Fig. 3. Emissions are sampled during the cycle according to the constant volume sampling technique and expressed in grams per kilometer for each pollutant.

In the USA, the FTP-75 (Federal Test Procedure) is used for emission certification of light-duty vehicles, consisting of a cold start phase, a transient phase and a hot start phase. It is complemented by two additional test procedures to account for high-speed driving (US06) and the use of air conditioning (SC03). Compared to the NEDC, the FTP-75 is more transient and covers a wider range of engine operating conditions.

For heavy-duty commercial vehicles emission certification, the engine is tested on an engine dynamometer. In the European Stationary Cycle (ESC),

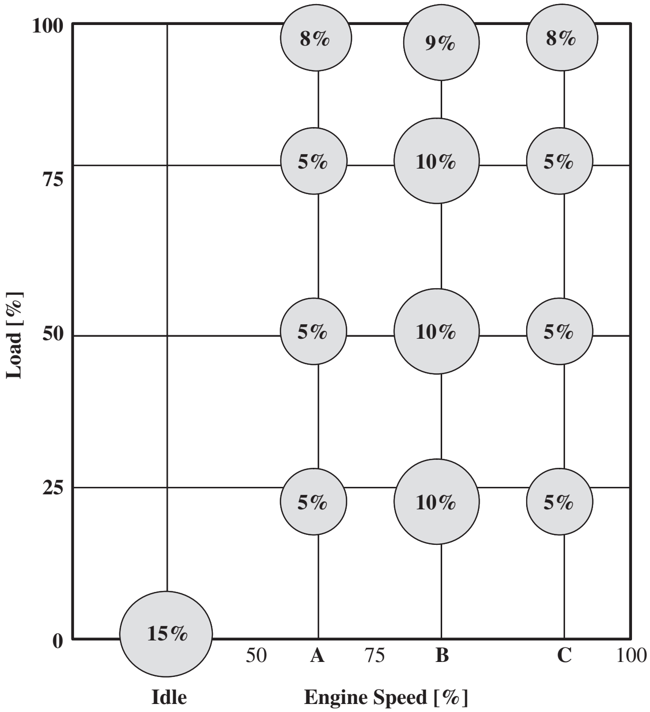

Fig. 4. ESC—European Stationary Cycle, weighing factors are given for the individual points (Dieselnet, 2007).

this is done in 13 steady-state modes, in which emissions are measured and are averaged over the cycle using weighing factors, cf. Fig. 4. Three additional test points are chosen by the tester. The ESC represents relatively high average load and therefore high exhaust gas temperatures. The stationary test is complemented by the European transient cycle (ETC) and the European load response (ELR) test to also account for transient conditions and for the purpose of smoke opacity measurements. The USA FTP-75 transient test for heavy-duty commercial vehicle engines consists of driving conditions representative of urban and freeway traffic, including a cold start. The average load factor is about 20–25% of the maximum horsepower at a given engine speed. A global harmonization of test cycles is under discussion.

To fulfill the increasingly stringent emission limits, two routes are being followed today, mostly simultaneously, which are lowering the engine raw emissions and increasing the efficiency of the exhaust gas aftertreatment. To lower engine raw emissions, the main parameters are air–fuel ratio, the optimization of the combustion chamber shape and intake flow movement, ignition/injection timing, in-cylinder pressure and exhaust gas recirculation.

In commercial vehicle engines, by means of cooled exhaust gas recirculation, in-cylinder temperatures are reduced, leading to lower NO_x, but mostly also to higher particulate emissions. To fulfill future emission standards, a combination of raw emission reduction and exhaust gas aftertreatment is necessary. Decreasing fuel economy with raw emission reduction has to be weighed against catalyst—and especially noble metal—price for exhaust gas aftertreatment.

Exhaust aftertreatment systems are becoming more and more advanced. Combined aftertreatment systems consisting of different catalyst technologies and particulate filter are developed by several vehicle manufacturers. The Bluetec system uses a different combination of technologies for different applications, i.e. vehicles and markets. Since October 2006, the passenger car Mercedes-Benz E320 Bluetec is sold in the US equipped with a combined system consisting of diesel oxidation catalyst (DOC), diesel particulate filter (DPF), NO_x storage and reduction catalyst (NSRC) and selective catalytic reduction (SCR) catalyst to comply with EPA (Environmental Protection Agency, USA) Bin 8 standards. Since 2005, the Mercedes-Benz Actros heavy-duty truck is equipped with EU IV/V compliant Bluetec system, which uses urea–SCR for NO_x reduction.

For the design and optimization of such increasingly complex exhaust aftertreatment systems, a purely experimental approach is very time and cost consuming. The investigation of all possible combinations of catalyst geometries, their position on the exhaust line and the resulting interactions leads to a huge testing effort, which can hardly be conducted in a tight-scheduled development process. Exhaust aftertreatment simulation can make a considerable contribution to the development of complex combined systems.

Different simulation tools are employed in the development of exhaust aftertreatment systems. Spatially 2D or 3D CFD simulation is commonly used to assess the effect of non-uniform flow conditions in pipes and housing and of non-uniform catalyst inlet flow on temperature distribution and reactions inside the monolith, thus enabling geometry optimization.

Spatially one-dimensional (1D) simulation has the advantage of shorter calculation times, enabling the modeling of complete exhaust aftertreatment systems consisting of a combination of different catalysts and particulate filter. The 2D or 3D effects are mostly neglected. The simulation enables a pre-selection of catalyst or particulate filter sizes and geometries before going onto the test bench. Variations of engine out parameters, i.e. raw emissions or exhaust gas temperature and their influence on catalyst or particulate filter performance are assessed. In combined systems, exhaust conditions for a catalyst or particulate filter are influenced by its upstream component and changes in one component affect all others further down the line. Furthermore, the development of operating, regeneration or control strategies for a complete exhaust aftertreatment system can be supported.

II. Simulation of Combined Exhaust Gas Aftertreatment Systems

For the modeling and simulation of combined exhaust gas aftertreatment systems, it is necessary to develop models for the different catalyst and particulate filter technologies. The combination of the individual models in a common software environment facilitates system definition by the user and data transfer between the individual models. A software environment called ExACT (Exhaust Aftertreatment Components Toolbox) has been developed and is used at Daimler AG (Chatterjee *et al.*, 2005, 2006; Güthenke *et al.*, 2007a,b) for this purpose. The software environment is based on Matlab/Simulink (2006) and includes models for different types of catalysts and particulate filters, cf. Fig. 5. Models for three-way catalyst (TWC), NSRC, SCR catalyst and coated DPF ((C)DPF) are included, as well as models for pipes, pipes with changing cross-sections, etc., to enable modeling of a complete exhaust line. Raw emissions are as yet not modeled but specified based on engine out measurements. Temperature and exhaust composition are analyzed between catalysts and at end-of-pipe. Post-processing also allows the analysis of the conditions inside a catalyst or particulate filter, e.g. concerning temperature or species concentration profiles.

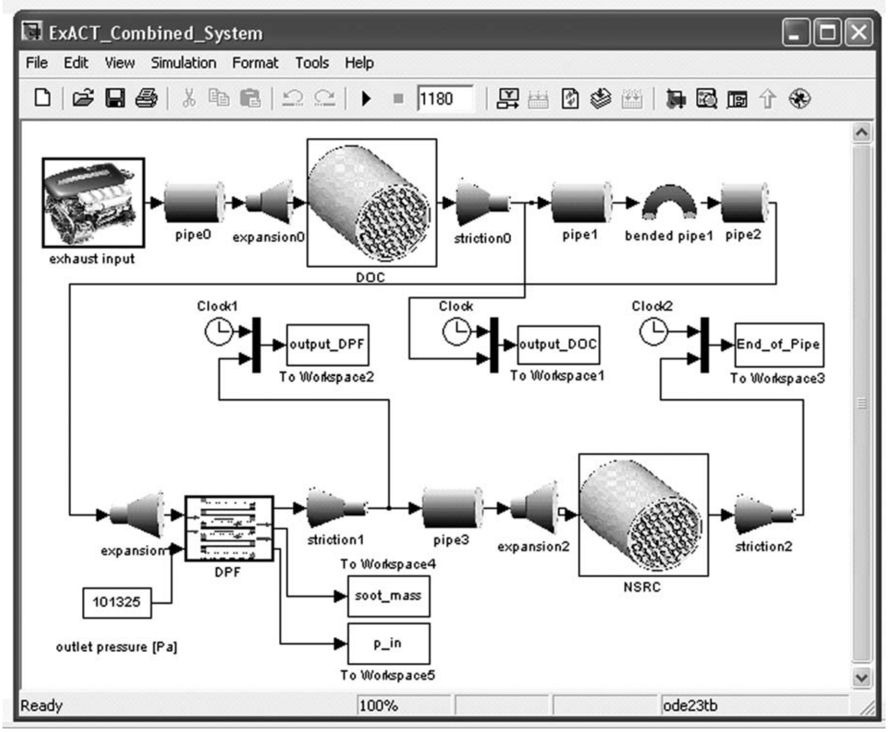

FIG. 5. Example of a combined exhaust gas aftertreatment system model.

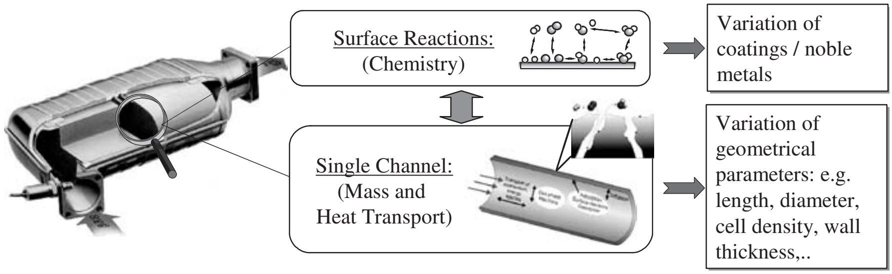

FIG. 6. Scheme of the catalyst model structure.

The catalyst and particulate filter models were developed individually with different university partners. They are described in the following sections. A key issue for all models is robustness and scalability as the applications range from passenger cars to heavy-duty commercial vehicles. The models are physical and chemically based, consisting of a transport model for heat and mass transfer phenomena in the monolith in gas and solid phases, cf. Fig. 6. The monolith reactor modeling is discussed in more detail in Section III.

In the washcoat, reaction rates are modeled via global reaction mechanisms. In such a global or macrokinetic reaction mechanism, several microkinetic adsorption, reaction and desorption steps are "lumped" together, reducing the overall number of kinetic parameters considerably. For some catalysts, e.g. TWC, the elementary steps are relatively well known and information on a microkinetic reaction mechanism including parameters can be found in literature (Braun *et al.*, 2000; Chatterjee *et al.*, 2001). For other catalysts however, e.g. NSRC, there is still a discussion in academia about the elementary steps taking place in the washcoat (Epling *et al.*, 2004a). Therefore, for the development of the catalyst models discussed in the following sections, global reaction kinetic approach was chosen. The developments of global reaction kinetics were however based on chemical knowledge of the system investigated, from literature and laboratory experiments. In the case of NH_3–SCR, the development of detailed, chemically consistent kinetic schemes has been paralleled by a dedicated investigation of their catalytic mechanism under the specific conditions of mobile applications, which differ considerably from those of conventional SCR applications for stationary plants, widely investigated in the past (Ciardelli *et al.*, 2004b; Nova *et al.*, 2006b; Tronconi *et al.*, 2007). The development of global reaction kinetic mechanisms is discussed in Section IV, the reaction mechanisms for the individual catalyst models for selective catalytic reduction catalyst (urea–SCR), NSRC and DOC are explained in Sections V, VI and VII, respectively.

The employed physical and chemically based modeling approach enables a relatively large variation of geometrical catalyst parameters, e.g. catalyst length, diameter, etc., with the global reaction kinetics and therefore the overall catalyst model still remaining valid. Due to the global reaction kinetic approach employed, for a variation of coatings or noble metals, new reaction kinetics or at least kinetic parameters need to be found.

As the models presented in this chapter are relatively complex, they are not used for control purposes in their current status. They can however be used for the development of control models, either by linearization and simplification, or as ‘‘virtual test bench’’. This way, a control model is pre-tuned on the catalyst or system model before parameterization on the ‘‘real’’ test bench, thus saving development time and costs.

The simulation of combined exhaust aftertreatment systems has also been undertaken by Wurzenberger and Peters (2003) and Wurzenberger and Wanker (2005). They focus on the 1D simulation of an urea–SCR system. The system includes a model for NO_2 production on a DOC, a model for urea injection, urea decomposition and hydrolysis catalyst, a model for a vanadium-type SCR catalyst and a model for NH_3 decomposition on a clean-up catalyst. The catalyst models consist of a 1D monolith model with global kinetic reactions on the washcoat surface, kinetic parameters have been taken from literature or adjusted to experimental data from literature. The complete model was implemented in AVL BOOST (2006). AVL BOOST is an engine cycle and gas exchange simulation software tool, which allows for the building of a model of the entire engine.

Another engine cycle and gas exchange simulation software tool which has been extended for exhaust aftertreatment simulation is GT-POWER (2006). This software includes models for engine components as well as templates for DOC, SCR catalyst, NSRC and TWC. Reaction kinetics can be provided by the user, based on templates. Kinetic parameters adaptation is supported with a built-in optimizer tool.

The hydraulic simulation tool AMESim (2006) has also been extended for exhaust aftertreatment simulation, by including routines developed together with IFP (2006). The software includes models for TWC, hydrocarbon (HC) trap, NSRC, oxygen storage, DOC and DPF as well as pipes, etc. Catalysts are modeled via 0D approach, hence all transport effects are lumped into reaction kinetic parameters. These kinetic parameters can be adapted by the user.

III. Monolith Reactor Modeling

In this section the models employed for simulation of catalytic monolith reactor are discussed, focusing on effective description of heat and mass transfer phenomena in monolith channel. The number of different mathematical models developed for converters of automobile exhaust gases over the last decades is huge—cf., e.g. Heck *et al.* (1976), Young and Finlayson (1976), Oh and Cavendish (1982), Zygourakis and Aris (1983), Chen *et al.* (1988), Tronconi and Forzatti (1992), Montreuil *et al.* (1992), Leclerc and Schweich (1993), Lie *et al.* (1993), Pinkas *et al.* (1995), Groppi *et al.* (1995a, b), Kirchner and Eigenberger (1996), Koltsakis *et al.* (1997), Koltsakis and Stamatelos (1997), Jahn *et al.* (1997), Dubien *et al.* (1997), Jirát *et al.* (1999a, b, 2001), Balakotaiah *et al.* (2000), Wanker *et al.* (2000), Hoebink *et al.* (2000), Chatterjee *et al.* (2001), Mukadi and Hayes (2002), Kočí *et al.* (2004a–d) and Tischer and Deutschmann (2005), the reviews by Groppi *et al.* (1999) and Hoebink *et al.* (2006) and numerous references given there. Until mid-1990s the modeling was mostly devoted to simple oxidation or TWCs, however, the developed fundamental physical models and selected reaction kinetics can be utilized also in the modeling of newer catalyst technologies.

Two sub-levels can be recognized in all the models (i) the description of heat and mass transport, ranging from simplified lumped models (cf., e.g. Balakotaiah *et al.*, 2000), via classical heterogeneous 1D plug flow reactor models, to fully distributed models (Tischer and Deutschmann, 2005; Wanker *et al.*, 2000) and (ii) the description of chemical reactions, ranging from single reaction (typically CO oxidation), via multiple reactions with pseudo-stationary Langmuir–Hinshelwood kinetics, addition of non-stationary storage sub-models (e.g. Jirát *et al.* 1999a; Kočí *et al.*, 2004c, 2007b; Koltsakis *et al.*, 1997; Kryl *et al.*, 2005), up to large, completely microkinetic schemes (e.g. Chatterjee *et al.*, 2001; Kočí *et al.*, 2004a, b, d; Mukadi and Hayes, 2002). For the routine use in automotive industry, it is necessary to consider the model as simple as possible, with reasonable computation times, while still retaining the essential reliability. The choice depends on the studied problem and the range of operating conditions.

A. MONOLITH CHANNEL

In many situations, the monolith reactor can be represented by a single channel. This assumption is correct for the isothermal or adiabatic reactor with uniform inlet flow distribution. If the actual conditions in the reactor are significantly different, more parallel channels with heat exchange have to be simulated (cf., e.g. Chen *et al.*, 1988; Jahn *et al.*, 1997, 2001; Tischer and Deutschmann, 2005; Wanker *et al.*, 2000; Young and Finlayson, 1976). In this section we will further discuss effective single channel models.

The most important processes in monolith channel—convection of exhaust gas, heat and mass transfer between the flowing gas and the washcoat, internal diffusion, catalytic reactions in the washcoat, heat and mass accumulation and heat conduction—are schematically depicted in Fig. 7.

The size of the entire monolith converter varies for individual applications (from small close-coupled ones in passenger cars to large ones in heavy-duty trucks) to meet similar space velocities and conversions for differently sized engines. However, cross-sectional channel density around 400 cpsi, diameter

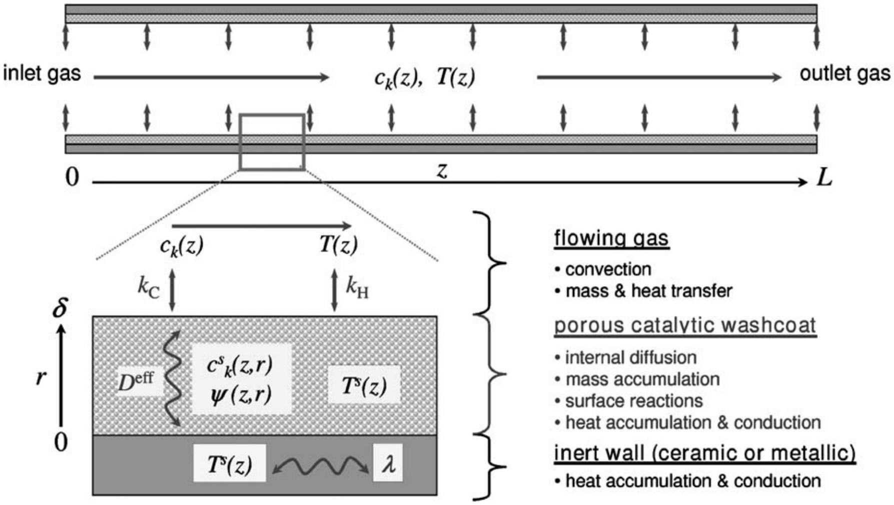

FIG. 7. Monolith channel topology and physical and chemical processes considered in the models (Kočí, 2005).

of the channel around 1 mm, thickness of the washcoat layer in the range 20–80 μm and wall thickness 100–200 μm are similar for most of the applications.

The following, well-acceptable assumptions are applied in the presented models of automobile exhaust gas converters: Ideal gas behavior and constant pressure are considered (system open to ambient atmosphere, very low pressure drop). Relatively low concentration of key reactants enables to approximate diffusion processes by the Fick's law and to assume negligible change in the number of moles caused by the reactions. Axial dispersion and heat conduction effects in the flowing gas can be neglected due to short residence times ($\approx$0.1 s). The description of heat and mass transfer between bulk of flowing gas and catalytic washcoat is approximated by distributed transfer coefficients, calculated from suitable correlations (cf. Section III.C). All physical properties of gas (c_p, ρ, μ, λ, D_k) and solid phase heat capacity are evaluated in dependence on temperature. Effective heat conductivity, density and heat capacity are used for the entire solid phase, which consists of catalytic washcoat layer and monolith substrate (wall).

The reactions take place only in active catalytic layer, the rates R_j are considered individually for each type of the converter (DOC, SCR, NSRC, TWC). The development of suitable reaction schemes and the evaluation of kinetic parameters are discussed generally in Section IV. The details for DOC, NSRC and SCR of NO_x by NH_3 are given in Sections V, VI and VII, respectively. The important species deposited on the catalyst surface are balanced (e.g. HC adsorption in DOC, oxygen and NO_x storage in NSRC, NH_3 adsorption in SCR). Heat transfer by radiation and homogeneous reactions can be omitted for temperatures below 600°C, which is well satisfied for lean exhaust catalysts. Additional assumptions special to the individual models are discussed in the respective sub-sections.

B. SPATIALLY 1D MODEL

In the spatially 1D model of the monolith channel, no transverse concentration gradients inside the catalytic washcoat layer are considered, i.e. the influence of internal diffusion is neglected or included in the employed reaction-kinetic parameters. It may lead to the over-prediction of the achieved conversions, particularly with the increasing thickness of the washcoat layer (cf., e.g., Aris, 1975; Kryl *et al.*, 2005; Tronconi and Beretta, 1999; Zygourakis and Aris, 1983). To overcome this limitation, the effectiveness-factor concept can be used in a limited extent (cf. Section III.D). Despite the drawbacks coming from the fact that internal diffusion effects are implicitly included in the reaction kinetics, the 1D plug-flow model is extensively used in automotive industry, thanks to the reasonable combination of physical reliability and short computation times.

1. *Model Equations*

The following balances are considered in spatially 1D, heterogeneous model of a monolith channel with plug-flow and surface storage of gas components: mass balances in the flowing gas, including accumulation, convection and external mass transfer, Eq. (1); mass balances in the washcoat pores, including accumulation, external mass transfer and catalytic reactions, Eq. (2); mass balances on the catalyst surface, including accumulation, and catalytic reactions, Eq. (3); enthalpy balance of the flowing gas, including accumulation, convection and gas–solid heat transfer, Eq. (4); enthalpy balance of the solid phase, including accumulation, axial heat conduction, gas–solid heat transfer, heat exchange with the surroundings (usually negligible for full-size monolith, more important for small laboratory reactor) and heat source from catalytic reactions, Eq. (5)

$$\frac{\partial c_k(z,t)}{\partial t} = -\frac{\partial (u c_k)}{\partial z} + \frac{k_c a}{\varepsilon^g} c(y_k^s - y_k), \quad k = 1 \ldots K \tag{1}$$

$$\frac{\partial c_k^s(z,t)}{\partial t} = \frac{k_c a}{\varepsilon^s (1-\varepsilon^g)\varphi^s} c(y_k - y_k^s) + \frac{1}{\varepsilon^s} \sum_{j=1}^{J} \nu_{k,j} R_j, \quad k = 1 \ldots K \tag{2}$$

$$\frac{\partial \psi_m(z,t)}{\partial t} = \frac{1}{\Psi_m^{\mathrm{cap}}} \sum_{j=1}^{J} \nu_{m,j}^{\psi} R_j, \quad m = 1 \ldots M \tag{3}$$

$$\rho c_p \frac{\partial T(z,t)}{\partial t} = -u \frac{\partial T}{\partial z} \rho c_p + \frac{k_{\mathrm{h}} a}{\varepsilon^{\mathrm{g}}} (T^{\mathrm{s}} - T) \tag{4}$$

$$\rho^{\mathrm{s}} c_p^{\mathrm{s}} \frac{\partial T^{\mathrm{s}}(z,t)}{\partial t} = \lambda^{\mathrm{s}} \frac{\partial^2 T^{\mathrm{s}}}{\partial z^2} + \frac{k_{\mathrm{h}} a}{(1 - \varepsilon^{\mathrm{g}})} (T - T^{\mathrm{s}}) - W(T^{\mathrm{s}} - T^{\mathrm{e}}) - \varphi^{\mathrm{s}} \sum_{j=1}^{J} \Delta H_{r,j} R_j \tag{5}$$

2. *Boundary Conditions*

$$c_k|_{z=0} = c_k^{\mathrm{in}}(t), \quad k = 1 \ldots K \tag{6}$$

$$T|_{z=0} = T^{\mathrm{in}}(t), \; u|_{z=0} = u^{\mathrm{in}}(t) \tag{7}$$

$$\left.\frac{\partial T^{\mathrm{s}}}{\partial z}\right|_{z=0} = 0, \quad \left.\frac{\partial T^{\mathrm{s}}}{\partial z}\right|_{z=L} = 0 \tag{8}$$

The inlet gas linear velocity u^{in} is calculated from the following equation:

$$u^{\mathrm{in}} = \frac{\dot{V}^{\mathrm{in}}}{S \varepsilon^{\mathrm{g}}} \tag{9}$$

The apparent gas hourly space velocity (SV) is defined at the standard temperature and pressure

$$\mathrm{SV} = \left.\frac{\dot{V}}{V}\right|_{\mathrm{STP}} \tag{10}$$

C. HEAT AND MASS TRANSFER BETWEEN BULK GAS AND CATALYTIC WASHCOAT

Mass and heat transfer between flowing gas and catalytic washcoat layer along the monolith channel are in 1D gas models approximated by distributed transfer coefficients $k_c(z)$ and $k_h(z)$, respectively—cf. Eqs. (1), (2), (4) and (5). The evaluation of transfer coefficients for laminar flow monolith reactors is still under debate. Various experimental and theoretical approaches have been proposed in the literature (cf., e.g. Balakotaiah *et al.*, 2000; Balakotaiah and West, 2002; Groppi *et al.*, 1995a, b; Hayes *et al.*, 2004; Heck *et al.*, 1976; Ramanathan *et al.*, 2003; Shah and London, 1978; Tronconi and Beretta, 1999; Tronconi and Forzatti, 1992; West *et al.*, 2003). Generally, the transfer coefficients can be calculated from the dimensionless Nusselt and Sherwood numbers, Eq. (11), which are determined from the empirically or theoretically derived correlations of the following general type, Eq. (12):

$$k_h(z) = \frac{\mathrm{Nu}\,\lambda^g}{d}, \quad k_c(z) = \frac{\mathrm{Sh}\,D}{d} \tag{11}$$

$$\mathrm{Nu} = f_1(\mathrm{Re}, \mathrm{Pr}, d, z), \quad \mathrm{Sh} = f_2(\mathrm{Re}, \mathrm{Sc}, d, z) \tag{12}$$

$$\mathrm{Re} = \frac{ud}{\mu^g}, \quad \mathrm{Sc} = \frac{\mu^g}{D}, \quad \mathrm{Pr} = \frac{c_p^g \mu^g \rho^g}{\lambda^g} \tag{13}$$

Transfer coefficients in catalytic monolith for automotive applications typically exhibit a maximum at the channel inlet and then decrease relatively fast (within the length of several millimeters) to the limit values for fully developed concentration and temperature profiles in laminar flow. Proper heat and mass transfer coefficients are important for correct prediction of cold-start behavior and catalyst light-off. The basic issue is to obtain accurate asymptotic Nu and Sh numbers for particular shape of the channel and washcoat layer (Hayes *et al.*, 2004; Ramanathan *et al.*, 2003). Even if different correlations provide different k_c and k_h profiles at the inlet region of the monolith, these differences usually have minor influence on the computed outlet values of concentrations and temperature under typical operating conditions.

Recently, a set of correlations including the effect of channel shape has been proposed by Ramanathan *et al.* (2003) on the basis of solution of the Navier–Stokes equations in the channel, with different solutions derived for ignited-reaction and extinct-reaction regimes. The comparison of various empirical and theoretical correlations with experimentally evaluated mass transfer coefficients is given by West *et al.* (2003). The correlations by Ramanathan *et al.* (2003) or Tronconi and Forzatti (1992) have been used in most simulations presented in this chapter.

D. Internal Diffusion in the Washcoat

The catalyst operation not only above, but also around the light-off temperature has been shown to be significantly affected by washcoat diffusion (cf., e.g. Hayes *et al.*, 2004, 2005; Kočí *et al.*, 2004a, b; Kryl *et al.*, 2005; Ramanathan *et al.*, 2003; Tronconi and Beretta, 1999; Zygourakis and Aris, 1983). The internal diffusion effects cannot be simply included into the reaction kinetics particularly in the case of parametric studies on the varying washcoat thickness.

There are two major types of diffusion contributing to mass transport in the monolith washcoat (cf., e.g. Aris, 1975; Froment and Bischoff, 1979, 1990; Poling *et al.*, 2001): volume (molecular) diffusion, Eq. (14), and Knudsen diffusion, Eq. (15), the latter one being dominant in small pores.

$$D_k^{\text{vol}} = \frac{144.9\, T^{1.75}/p}{\left(\omega_k^{1/3} + \omega_{\text{ref}}^{1/3}\right)^2 \sqrt{2/(10^{-3}/W_k + 10^{-3}/W_{\text{ref}})}} \tag{14}$$

$$D_k^{\text{Knudsen}} = \frac{2}{3} r_{\text{p}} \sqrt{\frac{8 R^{\text{g}} T}{\pi W_k}} \tag{15}$$

Using resistance-in-series model (Bosanquet formula), the diffusivity in pore with radius r_{p} is

$$D_k(r_{\text{p}}) = \left(\frac{1}{D_k^{\text{vol}}} + \frac{1}{D_k^{\text{Knudsen}}(r_{\text{p}})}\right)^{-1} \tag{16}$$

Porous catalytic washcoat exhibits bimodal pore size distribution with larger macropores ($r_{\text{p}} \approx 100$–$500\,\text{nm}$) among individual support material particles (e.g. γ-Al_2O_3, zeolites), and small meso-/micropores ($r_{\text{p}} \approx 3$–$6\,\text{nm}$) inside the particles. Typical pore size distribution and electron microscopy images of γ-Al_2O_3-based washcoat can be found, e.g. in Starý *et al.* (2006) and Kočí *et al.* (2006). Different theoretical models applied to this pore size distribution can give relatively large variations of the calculated effective diffusivity value (D^{eff}). The most commonly used approximations are (i) random-pore model (Wakao and Smith, 1962) using two characteristic transport pores (micropores μ and macropores M)

$$D_k^{\text{eff}} = \varepsilon_{\text{M}}^2 D_{\text{M},k} + \varepsilon_\mu^2 D_{\mu,k} + \frac{4(\varepsilon_{\text{M}} - \varepsilon_{\text{M}}^2)}{((1/D_{\text{M},k}) + ((1-\varepsilon_{\text{M}})^2/\varepsilon_\mu^2 D_{\mu,k}))} \tag{17}$$

and (ii) mean transport-pore model using one characteristic pore size r_p and tortuosity parameter (cf., e.g. Froment and Bischoff, 1979, 1990)

$$D_k^{\mathrm{eff}} = \frac{\varepsilon^{\mathrm{s}}}{\tau} D_k(r_{\mathrm{p}}) \tag{18}$$

Experimental determination of effective washcoat diffusivity in cordierite monolith coated by γ-Al_2O_3-based catalyst for automobile exhaust treatment has been done using either chromatographic impulse-response method (Monolith, 2007; Starý *et al.*, 2006) or measurements of steady countercurrent diffusion by modified Wicke–Kallenbach method (Hayes *et al.*, 2000; Zhang *et al.*, 2004). The experimentally observed values of effective diffusivity are around $1 \cdot 10^6\,\mathrm{m}^2/\mathrm{s}$ for CH_4 in γ-Al_2O_3-based washcoat at 298 K and standard pressure. Effective diffusion coefficients in SCR monolith catalysts for stationary deNO$_x$ operation were experimentally determined by Beeckman (1991), who measured the steady diffusion through SCR catalyst walls and found it in agreement with the Wakao–Smith random pore model.

Calculated reaction rates can be in the spatially 1D model corrected using the generalized effectiveness factor (η) approach for non-linear rate laws. The effect of internal diffusion limitations on the apparent reaction rate R^{eff} is then lumped into the parameter η evaluated in dependence on D^{eff}, δ and R_j (cf. Aris, 1975; Froment and Bischoff, 1979, 1990; Leclerc and Schweich, 1993).

$$R_j^{\mathrm{eff}} = \eta_j R_j \tag{19}$$

Under excess of the second reactant (in automobile exhaust gas typically H_2O, CO_2 and for lean-burn engines exhaust specifically also O_2), the effectiveness factor calculation can be simplified by approximating the reaction rate R_j by a pseudo-first-order rate law with respect to the component k using new rate constant $k_{\mathrm{ref},j}$ (evaluated from the original rate law)

$$R_j = k_{\mathrm{ref},j} c_k^{\mathrm{s}} \tag{20}$$

Then the classical Thiele modulus (Φ) and the effectiveness factor (η), expressing the extent of internal diffusion limitations in the catalytic washcoat layer of thickness δ, can be calculated according to (cf. Aris, 1975; Froment and Bischoff, 1979, 1990)

$$\Phi_j = \delta \sqrt{\frac{k_{\mathrm{ref},j}}{D_k^{\mathrm{eff}}}} \tag{21}$$

$$\eta_j = \frac{\tanh \Phi_j}{\Phi_j} \tag{22}$$

Values of effectiveness factors in washcoat layers with non-uniform thickness around the channel perimeter have been studied by Hayes *et al.* (2005). However, the applicability of (even the generalized) effectiveness factor approach is quite limited in complex systems with competing reactions, surface deposition of reaction components, non-linear rate laws and under transient operating conditions (e.g. periodically operated NSRC). Typically, the effectiveness factor method can be used for more accurate prediction of CO, H_2 and HC oxidation light-off and conversions in DOC.

E. Spatially 2D (1D + 1D) Model with Internal Diffusion

When the internal diffusion effects are considered explicitly, concentration variations in the catalytic washcoat layer are modeled both in the axial (z) and the transverse (radial, r) directions. Simple slab geometry is chosen for the washcoat layer, since the ratio of the washcoat thickness to the channel diameter is low. The layer is characterized by its external surface density a and the mean thickness δ. It can be assumed that there are no temperature gradients in the transverse direction within the washcoat layer and in the wall of the channel because of the sufficiently high heat conductivity, cf., e.g. Wanker *et al.* (2000). For the bulk gas, the spatially 1D description with the distributed heat and mass transfer coefficients is used, similarly as in the spatially 1D model.

1. *Model Equations*

The following balances are considered in the spatially 2D (1D + 1D), heterogeneous model of a monolith channel with plug-flow, internal washcoat diffusion and surface deposition of gas components (Kočí *et al.*, 2004a): mass balances in the flowing gas, including accumulation, convection and external mass transfer, Eq. (23); mass balances in the washcoat pores, including accumulation, internal diffusion and catalytic reactions, Eq. (24); mass balances on the catalyst surface, including accumulation, and catalytic reactions Eq. (25); enthalpy balance of the flowing gas, including accumulation, convection and gas–solid heat transfer, Eq. (26); enthalpy balance of the solid phase, including accumulation, axial heat conduction, gas–solid heat transfer, heat exchange with the surroundings and heat source from catalytic reactions, Eq. (27)

$$\frac{\partial c_k(z,t)}{\partial t} = -\frac{\partial (u c_k)}{\partial z} + \frac{k_c a}{\varepsilon^g} c(y_k^s|_{r=\delta} - y_k), \quad k = 1 \ldots K \tag{23}$$

$$\frac{\partial c_k^{\mathrm{s}}(z,r,t)}{\partial t}=\frac{D_k^{\mathrm{eff}}}{\varepsilon^{\mathrm{s}}}\frac{\partial^2 c_k^{\mathrm{s}}}{\partial r^2}+\frac{1}{\varepsilon^{\mathrm{s}}}\sum_{j=1}^{J}\nu_{k,j}R_j,\quad k=1\ldots K \tag{24}$$

$$\frac{\partial \psi_m(z,r,t)}{\partial t}=\frac{1}{\Psi_m^{\mathrm{cap}}}\sum_{j=1}^{J}\nu_{m,j}^{\psi}R_j,\quad m=1\ldots M \tag{25}$$

$$\rho c_p\frac{\partial T(z,t)}{\partial t}=-u\frac{\partial T}{\partial z}\rho c_p+\frac{k_{\mathrm{h}}a}{\varepsilon^{\mathrm{g}}}(T^{\mathrm{s}}-T) \tag{26}$$

$$\begin{aligned}\rho^{\mathrm{s}}c_p^{\mathrm{s}}\frac{\partial T^{\mathrm{s}}(z,t)}{\partial t}&=\lambda^{\mathrm{s}}\frac{\partial^2 T^{\mathrm{s}}}{\partial z^2}+\frac{k_{\mathrm{h}}a}{(1-\varepsilon^{\mathrm{g}})}(T-T^{\mathrm{s}})-W(T^{\mathrm{s}}-T^{\mathrm{e}})\\&\quad-\frac{a}{(1-\varepsilon^{\mathrm{g}})}\sum_{j=1}^{J}\int_{r=0}^{\delta}\Delta H_j R_j dr\end{aligned} \tag{27}$$

2. *Boundary Conditions*

Boundary conditions at the inlet ($z=0$) and at the outlet ($z=L$) of the monolith are the same as for the 1D model, cf. Eqs. (6)–(8). In the catalytic washcoat layer, $r=0$ corresponds to the wall boundary and $r=\delta$ is on the external surface of the washcoat. Boundary conditions for the washcoat layer are then

$$D_k^{\mathrm{eff}}\left.\frac{\partial c_k^{\mathrm{s}}}{\partial r}\right|_{r=\delta-}=k_{\mathrm{c}}c\left(y_k-\left.y_k^{\mathrm{s}}\right|_{r=\delta}\right),\quad k=1\ldots K \tag{28}$$

$$\left.\frac{\partial c_k^{\mathrm{s}}}{\partial r}\right|_{r=0}=0,\quad k=1\ldots K \tag{29}$$

There exists a relation between the volume of catalytic washcoat layer (represented in the 1D model by the volume fraction φ^{s} in the solid phase) and the characteristic thickness of the layer δ used in the spatially 2D model. This relation depends on the chosen washcoat geometry—for slab geometry used here it is

$$\delta a=\varphi^{\mathrm{s}}(1-\varepsilon^{\mathrm{g}}) \tag{30}$$

F. DETAILED 3D MODEL OF POROUS CATALYTIC WASHCOAT

For the detailed study of reaction–transport interactions in the porous catalytic layer, the spatially 3D model computer-reconstructed washcoat section can be employed (Kočí *et al.*, 2006, 2007a). The structure of porous catalyst support is controlled in the course of washcoat preparation on two levels: (i) the level of macropores, influenced by mixing of wet supporting material particles with different sizes followed by specific thermal treatment and (ii) the level of meso-/micropores, determined by the internal nanostructure of the used materials (e.g. alumina, zeolites) and sizes of noble metal crystallites. Information about the porous structure (pore size distribution, typical sizes of particles, etc.) on the micro- and nanoscale levels can be obtained from scanning electron microscopy (SEM), transmission electron microscopy (TEM), or other high-resolution imaging techniques in combination with mercury porosimetry and BET adsorption isotherm data. This information can be used in computer reconstruction of porous catalytic medium. In the reconstructed catalyst, transport (diffusion, permeation, heat conduction) and combined reaction–transport processes can be simulated on detailed level (Kosek *et al.*, 2005).

The computer-reconstructed catalyst is represented by a discrete volume phase function in the form of 3D matrix containing information about the phase in each volume element. Another 3D matrix defines the distribution of active catalytic sites. Macroporosity, sizes of supporting articles and the correlation function describing the macropore size distribution are evaluated from the SEM images of porous catalyst (Kočí *et al.*, 2006; Kosek *et al.*, 2005). Spatially 3D reaction–diffusion system with low concentrations of reactants and products can be described by mass balances in the form of the following partial differential equations (Kočí *et al.*, 2006, 2007a). For gaseous components k

$$\frac{\partial c_k(X,\ Y,\ Z,\ t)}{\partial t} = \frac{D_k^{\mathrm{eff}}}{\varepsilon^{\mathrm{s}}}\left(\frac{\partial^2 c_k}{\partial X^2} + \frac{\partial^2 c_k}{\partial Y^2} + \frac{\partial^2 c_k}{\partial Z^2}\right) + \frac{1}{\varepsilon^{\mathrm{s}}}\sum_{j=1}^{J} \nu_{k,j} R_j, \quad k = 1 \ldots K \tag{31}$$

For surface-deposited components m

$$\frac{\partial \psi_m(X,\ Y,\ Z,\ t)}{\partial t} = \frac{1}{\Psi_m^{\mathrm{cap}}}\sum_{j=1}^{J} \nu_{m,j}^{\psi} R_j, \quad m = 1 \ldots M \tag{32}$$

the given set of partial differential equations is then solved within the spatially 3D section of digitally reconstructed porous catalyst ($X \in \langle X_0, X_1 \rangle$, $Y \in \langle Y_0, Y_1 \rangle$, $Z \in \langle Z_0, Z_1 \rangle$). Examples of the obtained concentration and reaction rate profiles are given in Fig. 8.

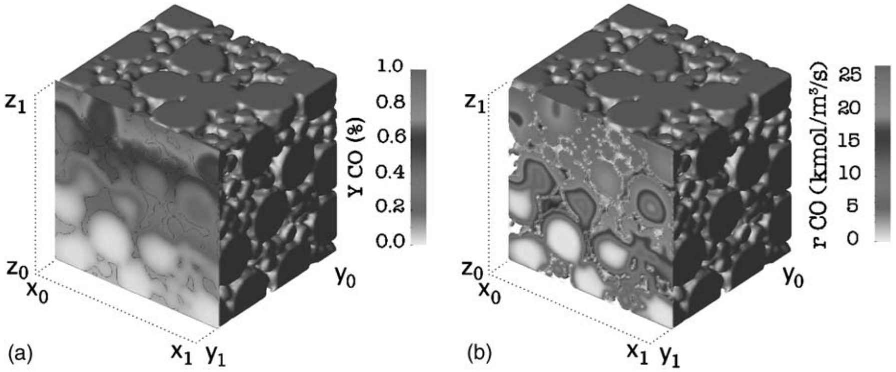

FIG. 8. Typical CO concentration and reaction rate profiles in the porous Pt/γ-Al_2O_3 catalyst reconstructed by particle-packing method. Mean hydraulic diameter of macropores $d_h^M = 300$ nm, macroporosity $\varepsilon^M = 18.1\%$. Free space corresponds to macropores, solid gray corresponds to mesoporous γ-Al_2O_3 with dispersed Pt. Length of the section edge 10 μm. Boundary Z_1:$y_{CO} = 1\%$, $y_{O_2} = 0.5\%$. (a) $T = 513$ K, (b) $T = 533$ K (Kočí *et al.*, 2007a) (see Plate 2 in Color Plate Section at the end of this book).

Two types of concentration gradients can be recognized: (i) the longer range concentration gradient in the local direction Z (corresponding to the global transverse direction r in the 2D model of entire monolith) and (ii) the short-range local gradients within the individual meso-/microporous catalyst particles (Kočí *et al.*, 2007a).

This methodology can be used for the calculation of local reaction rates and effectiveness factors in dependence on gas components concentrations, temperature and porous catalytic layer structure (cf. Fig. 9). The results can then be used as input values for simulations at a larger scale, e.g. the effective reaction rates averaged over the studied washcoat section can be employed as local reaction rates in the 1D model of monolith channel.

G. NUMERICAL SOLUTION

The detailed 3D model of porous catalyst is solved in pseudo-steady state. A large set of non-linear algebraic equations is obtained after equidistant discretization of spatial derivatives. This set can be solved by the Gauss–Seidel iteration method (cf. Kočí *et al.*, 2007a).

The system of hyperbolic and parabolic partial differential equations representing the 1D or 2D model of monolith channel is solved by the finite differences method with adaptive time-step control. An effective numerical solution is based on (i) discretization of continuous coordinates z, r and t, (ii) application of difference approximations of the derivatives, (iii) decomposition of the set of equations for T^s, T, c and c^s, (iv) quasi-linearization of

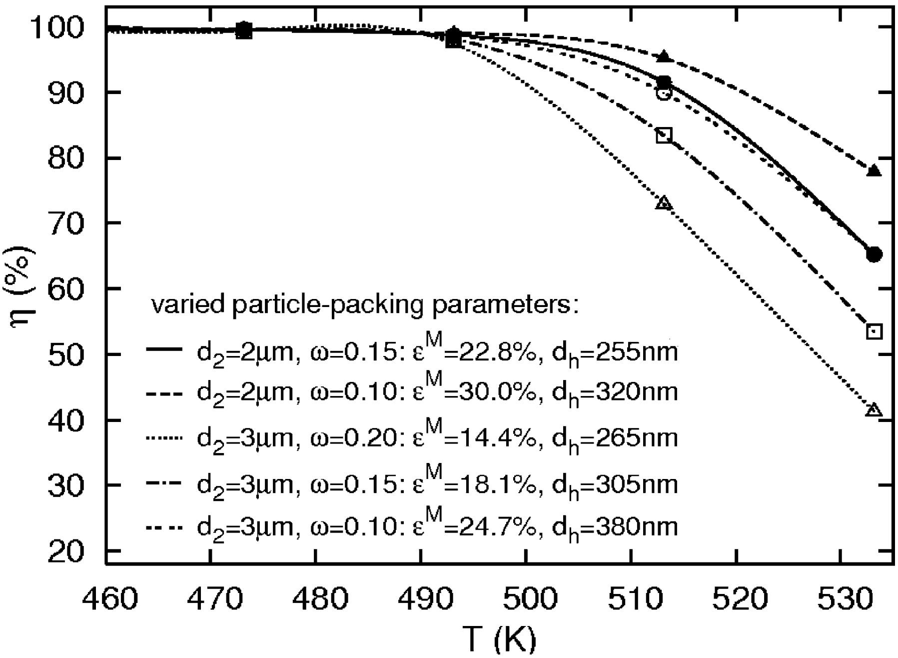

FIG. 9. Influence of local temperature T and varying catalyst structure on the CO oxidation effectiveness factor η. Each Pt/γ-Al_2O_3 catalyst was reconstructed by packing of γ-Al_2O_3 particles of two different sizes with small-to-large particles number 16. Small particles size $d_1 = 1$ μm was kept constant, while large particles size d_2 and particles fractional overlap ω (level of sintering) were varied. Gas concentrations the same as in Fig. 8 (Kočí *et al.*, 2007a).

the reaction terms R_j and (v) solving the resulting systems of linear algebraic equations (Kubíček *et al.*, 1997; Kočí, 2005). Quasi-linearization of reaction rates (first-order Taylor's expansion) and (semi-)implicit approximations of derivatives with respect to time are used for stable integration and to prevent the use of very short time-steps for stiff system. Another numerical approach involves spatial discretization of coordinates z, r and approximation of derivatives based on orthogonal collocation techniques (Finlayson, 1980; Villadsen and Michelsen, 1978; Villadsen and Stewart, 1967).

The solver is implemented in Fortran, using optimized treatment of diagonal-band matrices and analytical derivatives of reaction rates to minimize computation time. The software structure is modular, so that different reaction-kinetic modules for individual types of catalysts can be easily employed in the monolith channel model. The compiled converter models are then linked in the form of dynamic libraries into the common environment (ExACT) under Matlab/Simulink. Such combination enables fast and effective simulation of combined systems of catalytic monolith converters for automobile exhaust treatment.

IV. Development of Global Reaction Kinetics

The aim of the present section is to illustrate the procedures employed for the derivation of dynamic kinetic models appropriate for simulation of exhaust aftertreatment devices according to the converter models illustrated in the previous section. In particular, it will be shown how to derive global reaction kinetics which are based on a fundamental study aimed at the elucidation of the reaction mechanism. In principle, this approach enables a greater model adherence to the real behavior of the reacting system, which should eventually afford better results when validating the model in a wide range of operating conditions, as typically required for automotive applications.

The experimental setup and the testing procedures specifically needed for the dynamic kinetic investigation will be discussed in the following sections, as well as the relevant methods for data analysis and for parameter estimation.

A stage-wise scale-up approach is presented: (A) transient kinetic experiments are first performed in a microreactor over a small sample of catalyst in powder form in order to identify the reaction network and to evaluate the intrinsic kinetics in the absence of diffusional disguises; (B) such rate expressions, as well as the relevant geometrical and morphological characteristics of the monolith catalysts, are then incorporated into a transient mathematical model of monolithic reactors, developed along the lines presented in the previous Section III: this enables an intermediate validation of the kinetics against transient runs performed over small honeycomb catalyst samples (e.g., up to 10 cm^3 in volume) still operated in a lab-scale rig using synthetic gas mixtures; (C) the final validation is eventually based on engine test bench data collected over full-scale monolith converters, using real engine exhaust gases. This approach closely reflects the procedures recently applied in the development of simulation models for the SCR technology (see Section VII).

A. MICROREACTOR SCALE

1. *Experimental*

In the first stage of the investigation the catalyst can be considered in the form of powder in order to derive intrinsic transient kinetics of all the relevant reactive processes. To this purpose, dynamic reactive experiments can be performed in a simple tubular fixed-bed microreactor over small quantities (50–200 mg) of finely powdered catalyst: in principle, this guarantees negligible transport limitations and more controlled conditions (e.g. isothermal catalyst bed), hence enabling a direct estimation of intrinsic rate parameters by kinetic fit. Internal diffusion limitations are particularly relevant to the case of bulk (extruded) monolith catalysts, such as vanadium-based systems for NH_3/urea SCR; however, they may play a role also in washcoated honeycomb catalysts, depending on the thickness of the washcoat layers and on the local reaction rates.

According to this approach, a portion consisting of several grams from the original extruded or washcoated monolith is crushed and sieved to a fine powder of controlled size (e.g. with average particle diameter $< 100\,\mu m$), from which the catalyst sample required for testing should be extracted randomly: this procedure helps to rule out problems related to possible non-homogeneous distributions of the active species in the original monoliths.

In the case of washcoated honeycomb catalysts, differences in mechanical strength between the washcoat layer and the monolith substrate may favor maldistributions of the active phase when grinding and sieving: this should be carefully checked to prevent erroneous evaluations of the intrinsic catalytic activity. For example, iterative grinding of the cuts with bigger particles may be helpful to avoid segregation of sturdier cordierite chunks. Alternatively, one could consider of running kinetic experiments directly over the washcoat precursor powder, if available. While this rules out any maldistribution issue, the observed behavior could still be not fully representative of the intrinsic activity of the monolith catalyst due to the effects of thermal and chemical treatments associated with the washcoat deposition procedures (Chatterjee *et al.*, 2007).

The absence of significant physical limitations during reactive processes in the bed of crushed catalyst powder can be checked a posteriori by classical dimensionless diagnostic criteria (Kapteijn and Moulijn, 1997; Mears, 1971): notice however that such evaluations rigorously apply to steady-state conditions only.

An important requirement of kinetic studies for automotive aftertreatment devices is the capability of performing *dynamic* reactive experiments. Steady-state tests provide useful information for identification of reaction pathway and stoichiometry, but cannot capture the real operating behavior of catalytic converters for vehicles, which is transient in nature. Indeed, this is so not only because of the continuously changing conditions (temperature, composition, flow rate) of the engine exhausts: as extensively addressed in the following sections, the principles of NSRC and SCR applications largely rely on the storage/reaction/release dynamics of NO_x and of NH_3, respectively.

Dynamic kinetic runs can be performed according to, e.g. the transient response method (TRM) (Lietti *et al.*, 1997): it consists in executing stepwise changes of the concentration of one or more species in the feed mixture while continuously monitoring the temporal evolution of the system response. The perturbation of the feed composition is best realized using the fast 4-way pulse valves described in Section VII, which assure constant conditions of pressure and total flow. In this type of experiment the temperature is normally kept constant throughout the run. However, the temperature can be also increased at different constant heating rates during transient experiments of different nature (T-ramps), involving, e.g. temperature programmed desorption (TPD) or temperature programmed reaction (TPR). TPD runs provide information on the storage/release kinetics of species adsorbed onto the catalyst surface, including their T-dependent storage capacity: this is an important element for the design of deNO_x aftertreatment systems such as NSRC or SCR converters; TPR runs as well can supply information concerning the T-dependence of the reaction rates. For all such experiments, an obvious but critical prerequisite is that dead volumes in the test rig be minimized.

Transient experiments also require that the analysis of the outlet gas mixture must be continuous; this determines the choice of suitable gas analyzers with high time resolution, which should allow to monitor the temporal evolution of the largest possible number of species involved in the considered reactions. Measured composition dynamics typically need to be corrected for the transfer functions of the test rig and of the analyzers, as done, e.g. by Oh and Cavendish (1985), Siemund *et al.* (1996) and Nova *et al.* (2006a) on the basis of blank composition step change experiments. The important role of suitable gas analyzers in understanding the dynamic behavior of SCR systems is specifically discussed in (Ciardelli *et al.*, 2007b).

Operating conditions adopted in the transient kinetic runs are selected as similar as possible to those prevailing in the real aftertreatment device: this applies particularly to temperature ranges, feed gas compositions and reactant concentrations. In view of the typical composition of engine exhausts, the kinetic influence of species such as O_2, H_2O, CO_2, CO and HCs should be always considered in principle.

When several species and reactions are involved in the investigated process, the experimental work is best organized according to a hierarchical approach of growing complexity: first the simplest reacting systems (e.g. adsorption/desorption of individual species) are addressed, then the other reactants are included one by one, if possible, to address separately the main reactions. This approach offers a good insight into the individual reaction pathways prevailing in the global system, and can be helpful in reducing the correlation among the parameters estimates in the regression analysis.

In fact the intrinsic rate expressions are derived for each step of the process, and estimation of the intrinsic kinetics is obtained from the fit of different sets of data, according to a specific strategy which reflects the stage-wise approach mentioned above.

The general data set can then be complemented by additional dedicated runs: for example, specifically designed transient experiments can be implemented, too, to explore the system response to perturbations of the reaction conditions (e.g. sensitivity of the global stoichiometries to reaction temperature) and/or to gain more detailed dynamic information on the process.

2. *Data Analysis: Microreactor Model*

In order to estimate the rate parameters of the kinetic expressions derived in the fundamental study, the kinetic runs performed over the powdered catalyst are typically analyzed according to a heterogeneous 1D plug-flow dynamic model of the test microreactor, assuming the catalytic bed to be isothermal and isobaric and based upon the following unsteady material balance equations for gaseous (k) and adsorbed (m) species.

Gaseous phase:

$$\varepsilon^{\mathrm{g}}\frac{\partial c_k}{\partial t} = -u\frac{\partial c_k}{\partial z} - (1-\varepsilon^{\mathrm{g}})\sum_{j=1}^{J} v_{k,j}R_j \quad k = 1\ldots K \tag{33}$$

Adsorbed phase:

$$\Omega_m\frac{\partial \theta_m}{\partial t} = -\sum_{j=1}^{J} v_{m,j}R_j \quad m = 1\ldots M \tag{34}$$

where c_k is the gas-phase concentration of species k, θ_m the surface coverage of species m, ε^{g} the void fraction of the catalyst bed, u the gas linear velocity (m/s), Ω_m the catalyst adsorption capacity of species m (mol/m^{3}cat), R_j the intrinsic rate of reaction j (mol/m^{3}cat/s) and $v_{k,j}$ the stoichiometric coefficient of species k in reaction j.

Examples of derivation of rate expressions $R_j = R_j(T, c_k, \theta_m; \underline{\mathbf{x}})$ are presented in the following sections, depending on the amount of knowledge on the catalytic chemistry, either empirical or mechanistically consistent forms can be adopted.

3. Data Analysis: Parameter Estimation

The rate expressions $R_j = R_j(T, c_k, \theta_m; \underline{\mathbf{x}})$ typically contain functional dependencies on reaction conditions (temperature, gas-phase and surface concentrations of reactants and products) as well as on adaptive parameters $\underline{\mathbf{x}}$ (i.e., selected pre-exponential factors $k_{0,j}$, activation energies E_j, inhibition constants K, effective storage capacities ψ^{eq} and adsorption capacities Ψ^{cap} and Ω). Such rate parameters are estimated by multiresponse non-linear regression according to the integral method of kinetic analysis based on classical least-squares principles (Froment and Bischoff, 1979). The objective function to be minimized in the weighted least squares method is

$$f(\underline{\mathbf{x}}) = \sum_{i=1}^{\mathrm{NS}}\sum_{k=1}^{\mathrm{NY}} w_k\left(y_{i,k}^{\mathrm{exp}} - y_{i,k}^{\mathrm{sim}}(\underline{\mathbf{x}})\right)^2 \tag{35}$$

Here $\underline{\mathbf{x}}$ is the vector of kinetic parameters to be fitted, i the index of the experimental data point and of the corresponding simulation result, w_k denotes the weight of the component k in the sum and y^{exp} and y^{sim} stand for NY experimentally measured and simulated outlet components concentrations, respectively. Experimental responses y^{exp} are typically the temporal evolutions of all the species concentrations detected by the analytical systems at the test reactor outlet for all the NS data points collected in transient runs. Optimized parameter estimates yield the best possible match between y^{exp} and the corresponding responses y^{sim} calculated according to the test reactor model, Eqs. (33)-(34).

In relation to kinetic modeling of aftertreatment devices, the following specific aspects may be worth of note:

- The number of adaptive kinetic parameters **x** can become quite large, due to the large number of reactions involved, each of them being associated at least with one pre-exponential factor and with one activation energy. Accordingly, a sequential approach, aimed at estimating independently the rate parameters of selected blocks of reactions, is generally more advantageous than addressing simultaneously the parameter estimation for the global reacting system, as discussed above.
- Although there are many rate parameters, the degrees of freedom available for their estimation can be also quite large, since they result from the product between the number of experimental responses NY and the number of measured data points NS during the transient kinetic runs. Thus, one can expect in principle a reasonable statistical significance for the parameter estimates in spite of their large number. This should be, however, always checked (Himmelblau, 1970).
- Robust, multimethod regression codes are required to optimize the rate parameters, also in view of possible strong correlations. For example, the BURENL routine, specifically developed for regression analysis of kinetic schemes (Donati and Buzzi-Ferraris, 1974; Villa *et al.*, 1985) has been used in the case of SCR modeling activities. The adaptive simplex optimization method Amoeba was used for minimization of the objective function Eq. (35) when evaluating kinetic parameters for NSRC and DOC.
- Values of kinetic constants are calculated in dependence on temperature according to the Arrhenius law:

$$k_j = k_{0,j} \exp\left(-\frac{E_j}{RT}\right) \tag{36}$$

A useful re-parametrization of Eq. (36) is as follows:

$$k_j = \exp\left[A_j - B_j\left(\frac{1,000}{T} - \frac{1,000}{T_{\mathrm{ref}}}\right)\right] \tag{37}$$

Here T_{ref} is a suitable reference temperature (e.g. the mean temperature in the experimental field) and A_j and B_j the modified adaptive parameters obviously related to the original parameters $k_{0,j}$ and E_j. Replacing Eq. (36) with Eq. (37) can significantly reduce the correlation among the parameter estimates. The physico-chemical consistency of the rate parameter estimates generated by the regression procedure should be always examined in addition to their statistical significance.

B. MONOLITH REACTOR SCALE

1. *Experimental*

In a second and possibly alternative stage of the kinetic investigation, laboratory experiments are performed over the same catalyst as for the microreactor tests, but now in the form of small monolith samples with volumes of few cubic centimeter. Flow rates, as well as catalyst size, are thus typically increased about by a factor of 100 with respect to the microreactor kinetic runs. This experimental scale provides data either for intermediate validation of the intrinsic kinetics from stage one, or directly for kinetic parameter estimation if runs over catalyst powders are omitted.

The up-scaling from microreactor to small monoliths principally deals with the change of geometry (from powdered to honeycomb catalyst) and fluid dynamics (from turbulent flow in packed-bed to laminar flow in monolith channels). In this respect, it involves therefore moving closer to the conditions prevailing in the real full-scale monolithic converter, while still operating, however, under well controlled laboratory conditions, involving, e.g. the use of synthetic gas mixtures.

If kinetic runs over the same catalyst in powder form are available, comparing them with tests over small monolith samples at the same conditions permits also a direct experimental evaluation of the role of diffusion processes in determining the catalytic performances.

2. *Dynamic Monolithic Reactor Model*

This intermediate scale affords a preliminary validation of the intrinsic kinetics determined on the basis of microreactor runs. For this purpose, the rate expressions must be incorporated into a transient two-phase mathematical model of monolith reactors, such as those described in Section III. In case a 2D (1D + 1D) model is adopted, predictive account is possible in principle also for internal diffusion of the reacting species within the porous washcoat or the catalytic walls of the honeycomb matrix.

C. ENGINE TEST BENCH SCALE

In a third stage, test bench experiments are performed over full-scale monolith catalysts feeding real engine exhausts, and the data are used for final validation both of the kinetics and of the converter model. The up-scaling from small honeycombs to the full-scale monolithic converter does not involve changes in the catalyst morphology and in the flow regime, but the catalyst size is increased by two-to-three orders of magnitude. Besides, real engine exhausts are used as feed gases, enabling at this stage verification of possibly overlooked composition effects on the reaction kinetics.

V. Diesel Oxidation Catalyst

A. Functions of DOC

The composition of diesel emissions is more complex than that of the spark ignited gasoline engines. The emissions from diesel engines contain solids (dry carbon and ash), liquids (liquid phase hydrocarbons, H_2SO_4) and gases (HC, CO, NO_x, SO_2). The combinations of solids and liquids in the exhaust form particulates or total particulate matter (TPM). The particulates are composed mainly of dry carbon (soot), liquid phase hydrocarbons and adsorbed sulfuric acid and/or sulfates from the fuel (DieselNet, 2007). Most of the sulfur in the fuel is present in the exhaust as gaseous SO_2, only a small part is oxidized to SO_3 which with water forms condensable sulfuric acid. The liquid hydrocarbons in the particulates originate either from unburned fuel, or from the lubricating oil and other additives. They form the soluble organic fraction (SOF) or volatile organic fraction (VOF).

A standard DOC is able to reduce the TPM emission mass by approximately 30%, but no significant reduction in the number of PM particles is achieved (only SOF is abated). Higher PM conversions up to 70% can be achieved in special flow-through DOC monoliths employing substrates with a complex channel geometry enforcing turbulent flow (Jacobs *et al.*, 2006). Recently, closed wall-flow monoliths—DPF—providing more than 95% efficiency in TPM abatement became standard for particulates aftertreatment (cf., e.g. DieselNet, 2007; Gulati *et al.*, 2006).

Thus, the main function of the DOC is to oxidize CO and unburned HCs. The secondary function, utilized in combined exhaust aftertreatment systems, is the oxidation of NO to NO_2, which then enables optimum operation of the NO_x aftertreatment catalysts placed down the exhaust line (NSRC and/or SCR, cf. Sections VI, VII and VIII, and also DPF).

Exhaust temperatures and concentrations of combustibles from diesel engines are generally lower than those met in gasoline engines, hence a highly active catalyst with low light-off temperature for CO and HC oxidation is required (Farrauto and Kenneth, 1996; Koltsakis *et al.*, 1997). However, the catalyst should have low catalytic activity for the oxidation of sulfur dioxide as resulting sulfates can adsorb onto soot and/or catalytic surface and deactivate the DOC or other catalysts down the exhaust treatment line. Recently, diesel fuels with significantly reduced sulfur content are available in the market—50 ppm wt. S in standard fuel and 15 ppm wt. S in "sulfur-free" fuel (DieselNet, 2007).

At the cold start of the engine the catalyst is not able to oxidize carbon monoxide and hydrocarbons present in the exhaust. Therefore, zeolites are added into γ-Al_2O_3-based catalytic washcoat for HC adsorption at low temperatures, resulting in an integrated adsorber–reactor system (Jirát *et al.*, 2001; Kryl *et al.*, 2005). For optimum operation of such a system, the consecutive HC desorption induced by increasing temperature should not occur earlier than the catalyst light-off.

B. DEVELOPMENT OF A DOC GLOBAL KINETIC MODEL

In this section we shall discuss the development of a global kinetic model for DOC. The basic model reactions considered in the DOC model are summarized in Table II. Here the real HC mixture is modeled by two characteristic hydrocarbons—propene and decane. Propene represents more reactive, light hydrocarbons, which practically do not adsorb during cold start, while decane is a representative of heavier hydrocarbons with significant adsorption on

TABLE II
MODEL REACTIONS FOR THE DIESEL OXIDATION CATALYST

Reaction step	Reaction rate	No.
$CO+\frac{1}{2}O_2\rightarrow CO_2$	$R_1=\frac{k_1 y_{CO} y_{O_2}}{G_1}$	R1
$H_2+\frac{1}{2}O_2\rightarrow H_2O$	$R_2=\frac{k_2 y_{H_2} y_{O_2}}{G_1}$	R2
$C_3H_6+\frac{9}{2}O_2\rightarrow 3H_2O+3CO_2$	$R_3=\frac{k_3 y_{C_3H_6} y_{O_2}}{G_1}$	R3
$C_{10}H_{22}+\frac{31}{2}O_2\rightarrow 11H_2O+10CO_2$	$R_4=\frac{k_4 y_{C_{10}H_{22}} y_{O_2}}{G_2}$	R4
$NO+\frac{1}{2}O_2\leftrightarrow NO_2$	$R_5=\frac{k_5(y_{NO} y_{O_2}^{0.5}-y_{NO_2}/K_{y,5}^{eq})}{G_1}$	R5
$2NO+C_3H_6+\frac{7}{2}O_2\rightarrow 3CO_2+N_2+3H_2O$	$R_6=\frac{K_6 R_2 y_{NO}}{G_3}$	R6
$C_{10}H_{22}+Ze\leftrightarrow C_{10}H_{22}{*}Ze$	$R_7=k_7^{ads}\Psi_{HC}^{cap} y_{C_{10}H_{22}}(1-\psi_{HC})$ $-k_7^{des}\Psi_{HC}^{cap}\psi_{HC}$	R7

Note:

$$G_1=(1+K_{a,1}y_{CO}+K_{a,2}y_{C_3H_6})^2(1+K_{a,3}y_{CO}^2 y_{C_3H_6}^2)(1+K_{a,4}y_{NO_x}^{0.7})T^s$$

$$G_2=1+K_{a,5}y_{C_{10}H_{22}},\quad G_3=(1+K_{a,6}y_{O_2})(1+K_{a,7}y_{NO})$$

All molar fractions y are considered locally in catalyst pores, the superscript "s" is omitted for brevity. If the DOC is operated temporarily also under fuel-rich conditions (e.g. during regeneration of the NSRC or DPF in a combined system) the reactions R6-R7, R8-R9 and R11–R14 in Table III (Section VI) should also be considered.

zeolites and higher light-off temperature. Additional hydrocarbons may be considered to describe the mixture more accurately, e.g. toluene for aromates (cf. Kryl *et al.*, 2005).

Only the reactions taking place under excess of oxygen (lean conditions) are discussed in this section. However, the reactions taking place in the DOC under the fuel-rich conditions should also be considered in the case of a specifically controlled diesel engine with combined exhaust aftertreatment system containing, e.g., periodically operated NSRC or DPF with active regeneration. These additional reactions include: (i) water gas shift and steam reforming, (ii) NO reduction by CO and H_2 and (iii) oxygen storage and reduction. These reactions are discussed in Section VI dedicated to the NSRC (cf. Table III, reactions R6-R7, R8-R9 and R11–R14, respectively).

In the next sections, the reactions from Table II will be discussed in the sequence corresponding to the procedure of kinetic parameter evaluation. At first, parameters of each single reaction are evaluated separately using the data obtained from laboratory experiments with the simplest inlet gas composition (i.e., the basic components plus one variable component). The resulting parameter values are then further tuned according to the results from the measurements focused on particular reaction subsystems (e.g. $HC + O_2 + NO$), where also the inhibition and selectivity constants are evaluated. The complete reaction system is considered in the final step of the data fitting (cf. Kryl *et al.*, 2005).

In the laboratory experiments, DOC monolith samples (length 7.5 cm, diameter 1.4 cm) with rather thin catalyst layer coating ($\approx 25\,\mu m$) were employed to minimize the internal diffusion effects. The samples were placed into a thermostat to suppress the formation of temperature-gradients along the channels. In the course of each experiment, the temperature of the inlet gas and the monolith sample was increased at a constant rate of 10 K/min within the range of 300–800 K. The exhaust gases at the inlet of the converter were simulated by synthetic gas mixtures with defined compositions and flow rates (cf. individual figure captions; all gas mixtures contained 6% CO_2 and 6% H_2O).

1. *HC Adsorption*

Transient deposition of hydrocarbons on zeolites during a cold start operation of the DOC can be modeled by the rate laws based on Langmuir or Temkin mechanism for physical adsorption/desorption (cf., e.g. Goralski *et al.*, 2000; Koltsakis and Stamatelos, 2000; Kruglov and Aris, 1995; Kryl *et al.*, 2005; Twigg, 2006). The rate laws for the adsorption and desorption of hydrocarbons are then

$$R_{\mathrm{HC,\,ads}} = k_{\mathrm{HC,\,ads}} \Psi_{\mathrm{HC}}^{\mathrm{cap}} y_{\mathrm{HC}} (1 - \psi_{\mathrm{HC}}) \tag{38}$$

$$R_{\mathrm{HC,\,des}} = k_{\mathrm{HC,\,des}} \Psi_{\mathrm{HC}}^{\mathrm{cap}}\ \psi_{\mathrm{HC}} \tag{39}$$

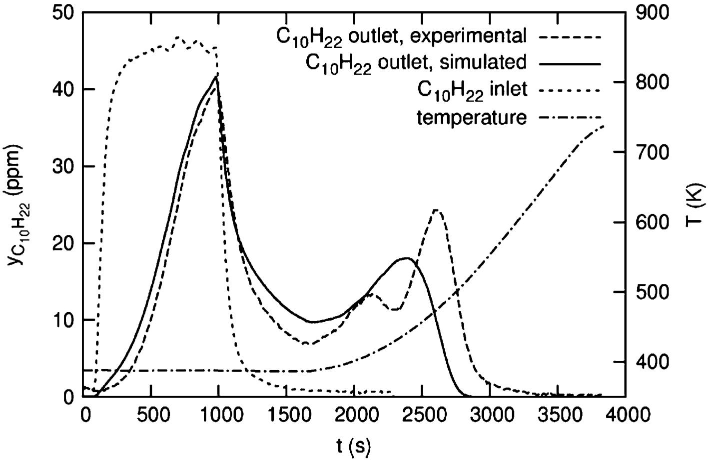

FIG. 10. Evaluation of kinetic parameters for the DOC model—HC adsorption/desorption (reaction R7 in Table II). Comparison of the measured and simulated outlet $C_{10}H_{22}$ concentrations in the course of the adsorption/desorption experiment. Synthetic gas mixture, other gases: 6% CO_2, 6% H_2O, N_2 balance, SV = 30,000 h^{-1} (Kryl *et al.*, 2005). Reprinted with permission from *Ind. Eng. Chem. Res.* **44**, 9524, © 2005 American Chemical Society.

A typical experiment, arranged for the evaluation of kinetic parameters Ψ_{HC}^{cap} (HC adsorption capacity), $k_{HC,\,ads}$ (rate constant for the non-activated adsorption of hydrocarbons) and the rate constant of HC desorption $k_{HC,\,des}(T)$ increasing with temperature according to Eq. (36), is depicted in Fig. 10. First, the catalytic washcoat was purified at 673 K using an inlet gas mixture of 14% O_2 in nitrogen for 10 min to remove all adsorbed HCs and NO_x. Then, after cooling the catalyst in pure N_2 feed, a mixture of HC in nitrogen was introduced into the monolith at a constant temperature of 383 K for 15 min. In the next step, the inlet gas was replaced by pure N_2, and after 10 min, constant temperature conditions were changed to a temperature ramp increasing with 10 K/min. The space velocity was kept constant at 30 000 h^{-1} throughout the experiment (Kryl *et al.*, 2005).

2. *CO and HC Oxidation*

Detailed microkinetic models are available for CO, H_2 and HC oxidation on noble metal(s) (NM)/γ-Al_2O_3-based catalysts (cf., e.g. Chatterjee *et al.*, 2001; Harmsen *et al.*, 2000, 2001; Nibbelke *et al.*, 1998). The model for CO oxidation on Pt sites includes both Langmuir–Hinshelwood and Eley–Rideal pathways (cf., e.g., Froment and Bischoff, 1990). Microkinetic description of the hydrocarbons oxidation is more complicated, particularly due to a large number of different reaction intermediates formed on the catalytic surface. Simplified mechanisms, using just one or two formal surface reaction steps, are thus usually employed for the HC decomposition, and only simpler hydrocarbons are considered—cf., e.g., Harmsen *et al.* (2000, 2001).

The microkinetic models provide quite detailed description of the transients in catalyst operation. However, the number of balanced species and reaction steps is quite high for a realistic exhaust gas composition, due to the explicit consideration of all surface-deposited reaction intermediates. The models using microkinetic reaction schemes may also exhibit quite complex non-linear dynamic behavior (cf., e.g., Kubíček and Marek, 1983; Marek and Schreiber, 1995), including multiplicities of steady states, hysteresis and stable autonomous oscillations. Such behavior has been described and analyzed for a certain range of operation parameters in monolith models ranging from a lumped one (CSTR), to a spatially 2D (1D + 1D) one, both for CO oxidation alone and the complete $CO + O_2 + HC + NO_x$ system (Kočí *et al.*, 2004a, d).

When a simple, fast and robust model with global kinetics is the aim, the reaction kinetics able to predict correctly the rate of CO, H_2 and hydrocarbons oxidation under most conditions met in the DOC consist of semi-empirical, pseudo-steady state kinetic expressions based on Langmuir–Hinshelwood surface reaction mechanism (cf., e.g., Froment and Bischoff, 1990). Such rate laws were proposed for CO and C_3H_6 oxidation in Pt/γ-Al_2O_3 catalytic mufflers in the presence of NO already by Voltz *et al.* (1973) and since then this type of kinetics has been successfully employed in many models of oxidation and three-way catalytic monolith converters

$$R_{CO} = \frac{k_{CO} y_{CO} y_{O_2}}{G_1} \tag{40}$$

$$R_{C_3H_6} = \frac{k_{C_3H_6} y_{C_3H_6} y_{O_2}}{G_1} \tag{41}$$

$$G_1 = (1 + K_{a,1} y_{CO} + K_{a,2} y_{C_3H_6})^2 (1 + K_{a,3} y_{CO}^2 y_{C_3H_6}^2)(1 + K_{a,4} y_{NO_x}^{0.7}) T \tag{42}$$

The values of kinetic parameters (pre-exponential factors $k_{0,j}$ and activation energies E_j of rate constants k and inhibition constant K_a) can for a particular catalyst be determined by weighted least squares method, Eq. (35), from the light-off or complete ignition–extinction curves measured in experiments with slowly varying one inlet gas variable—temperature or concentration of one component (cf., e.g., Ansell *et al.*, 1996; Dubien *et al.*, 1997; Dvořák *et al.*, 1994; Kryl *et al*, 2005; Kočí *et al.*, 2004c, 2007b; Pinkas *et al.*, 1995).

Examples of light-off experiments for CO and $C_{10}H_{22}$ are given in Fig. 11 together with the results of the 1D model using global DOC kinetics. In the case of decane, the adsorption has to be considered with the kinetic parameters already evaluated from the adsorption/desorption experiments

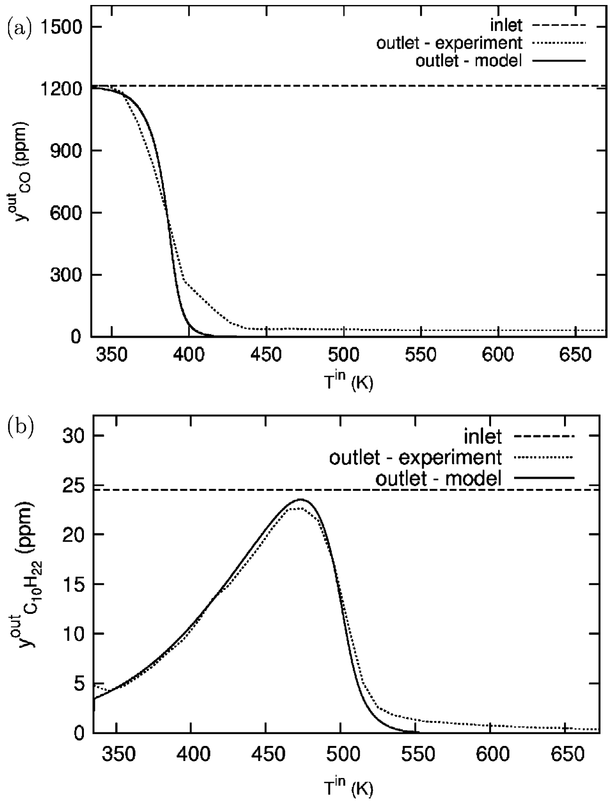

FIG. 11. Evaluation of kinetic parameters for the DOC model—CO and HC oxidation. Comparison of experimentally observed and simulated outlet concentrations in the course of the oxidation light-off for simple mixtures: (a) CO, reaction R1; (b) $C_{10}H_{22}$, reactions R4 and R7 (cf. Table II). Lab experiments with isothermal monolith sample using synthetic gas mixtures (14% O_2, 6% CO_2, 6% H_2O, N_2 balance). Rate of temperature increase 10 K/min, SV = 30,000 h^{-1} (Kryl *et al.*, 2005). Reprinted with permission from *Ind. Eng. Chem. Res.* **44**, 9524, © 2005 American Chemical Society.

(cf. Fig. 10). During the kinetic parameter evaluation procedure, the experiments are performed first for individual reactions. After the evaluation of the rate and self-inhibition constants for CO and individual HCs, the remaining inhibition constants are evaluated from the experiments with the combined mixtures.

Particular care should be given to the inhibition parameters if the DOC is operated also under temporarily rich conditions (i.e., with NSRC or DPF). The light-off temperature varies significantly for lean and rich exhaust gas and depends also on NO_x concentration (cf. Fig. 21 in Section VI on the NSRC kinetics).

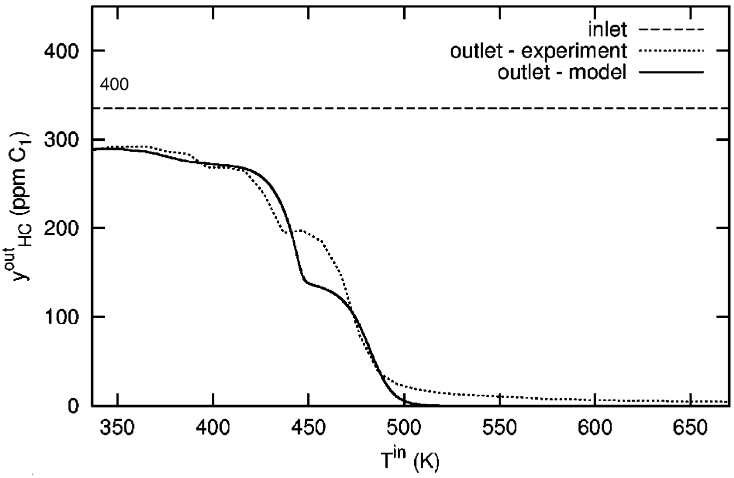

FIG. 12. Comparison of the measured and simulated light-off of a more complex HC mixture. DOC monolith sample with pre-adsorbed hydrocarbons (initial $\psi_{HC} = 0.3$). Lab experiment with isothermal monolith sample using synthetic gas mixture (1,200 ppm CO, 55 ppm C_3H_6, 10 ppm $C_{10}H_{22}$, 10 ppm $C_6H_5CH_3$, 140 ppm NO, 14% O_2, 6% CO_2, 6% H_2O, N_2 balance). Rate of temperature increase 10 K/min, SV = 30,000 h^{-1} (Kryl *et al.*, 2005). Reprinted with permission from *Ind. Eng. Chem. Res.* **44**, 9524, © 2005 American Chemical Society.

The typical evolution of the outlet HC concentrations in the course of the complex mixture light-off is shown in Fig. 12. Here the values of kinetic parameters obtained from the experiments with individual mixtures have been kept constant and the experiment was used for the kinetics validation. We can observe the adsorption at lower temperatures, followed by the two steps corresponding to the ignition of the "fast" (C_3H_6) and "slow" ($C_{10}H_{22}$) hydrocarbons, respectively. Eventually, an HC desorption peak can be observed during the light-off for the catalysts with high HC adsorption capacity and lower noble metal activity (Jirát *et al.*, 1999b; Kryl *et al.*, 2005).

3. NO Oxidation to NO_2

The NO oxidation to NO_2 is a reversible reaction limited by thermodynamic equilibrium. The typical dependence of the NO_2 outlet concentration on temperature is shown in Fig. 13. At low temperatures, NO_2 is thermodynamically more stable than NO but the reaction rate is rather slow. At higher temperatures, the reaction rate increases, but concurrently the NO_2 formation becomes limited by thermodynamic equilibrium. Thus, the outlet NO_2 concentration from the DOC typically exhibits a maximum at intermediate temperatures.

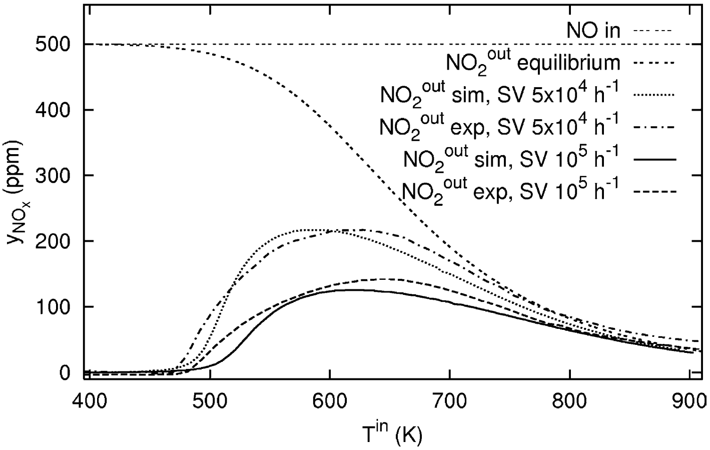

FIG. 13. Evaluation of kinetic parameters for the DOC model—NO oxidation (reaction R5 in Table II). Comparison of measured and simulated outlet NO_x concentrations in the course of temperature ramp (2 K/min) for two different space velocities (SV = 50,000 and 100,000 h^{-1}). Lab experiment with isothermal monolith sample using synthetic gas mixture (100 ppm CO, 100 ppm C_3H_6, 500 ppm NO, 8% O_2, 8% CO_2, 8% H_2O, N_2 balance).

The actual NO/NO_2 ratio in the exhaust gas significantly influences the NO_x reactions in catalysts positioned downstream the exhaust treatment line, particularly the NO_x storage in the NSRC (cf. Section VI), the oxidation of PM in DPF (cf., e.g., the review by Gulati *et al.*, 2006) and the SCR of NO_x by ammonia in the urea–SCR catalyst (cf. Sections VII and VIII).

The global rate law considering the reaction equilibrium constant K^{eq} is employed quite often in automotive exhaust catalyst models because it ensures the following thermodynamic limitations in a wide range of operating conditions:

$$R_{NO/NO_2} = k_{NO/NO_2} \frac{(y_{NO} y_{O_2}^{0.5} - y_{NO_2}/K^{eq})}{G} \tag{43}$$

The term G—e.g., in the form given in Eq. (42)—accounting for the inhibition by HC and CO should not be omitted on the right-hand side of Eq. (43). The NO oxidation rate is influenced by these components present in the complete exhaust gas mixture, which can be observed during cold start and in rich exhaust peaks.

The value of reaction rate Eq. (43) can be negative when NO_2 present in the mixture is transformed to NO via backward reaction, typically at higher temperatures. A comparison of measured and simulated outlet NO_2 concentrations in dependence on temperature can be seen for two different space velocities in Fig. 13. The pre-exponential factor $k_{0,j}$ and activation energy E_j of the kinetic constant k_{NO/NO_2} in the global rate law were evaluated by the weighted least squares method, Eq. (35).

4. Lean NO_X Reduction by HC

NO_x reduction conversions met in the DOC are quite low. Excess of air in burned lean fuel mixture results in excess of oxygen in the exhaust. Under such conditions, the reducing components naturally present in diesel exhaust (CO, H_2 and HC) are readily oxidized by the excessive oxygen and NO_x remains unreduced. However, the unburned hydrocarbons still exhibit a certain activity for NO reduction on NM/γ-Al_2O_3 and NM/zeolites catalysts under lean conditions (HC–SCR). Many efforts have been put into the investigation of different NM-based or alternative catalysts tailored for the HC–SCR reaction and the development of reliable reaction mechanisms—cf., e.g., Joubert *et al.* (2006) and the reviews by Burch *et al.* (2002) and Burch (2004).

However, there are several major drawbacks that hinder practical application of this NO_x reduction method in automobile exhaust aftertreatment: (i) The NO reduction activity is typically limited to a certain temperature window, for NM-based catalysts it is around the light-off—cf. Fig. 14 and Ansell *et al.* (1996), Jirát *et al.* (1999b), Burch *et al.* (2002) and Joubert *et al.* (2006). (ii) With low HC concentrations and the exhaust composition met in modern diesel engines, the achieved NO_x conversions in real driving cycles are quite low (typically around 5–10%, cf., e.g., Kryl *et al*, 2005). (iii) The selectivity of NO_x reduction is problematic, N_2O may form up to 50% of the product (Burch *et al.*, 2002; Joubert *et al.*, 2006). Alternative (Cu-, Co-, Ag-, etc., based) catalysts may provide a wider temperature window or better selectivity for

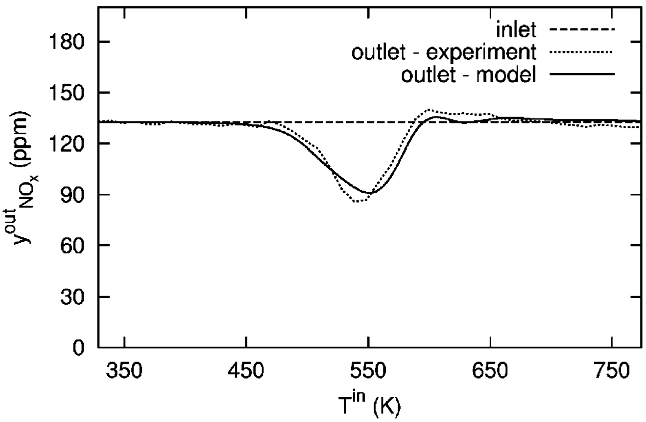

FIG. 14. Evaluation of kinetic parameters for the DOC model—lean NO_x reduction (reaction R5 in Table II). Comparison of measured and simulated outlet NO_x concentrations in course of a temperature ramp (10 K/min). Lab experiment with isothermal monolith sample using synthetic gas mixture (1,200 ppm CO, 55 ppm C_3H_6, 10 ppm $C_{10}H_{22}$, 10 ppm $C_6H_5CH_3$, 140 ppm NO, 14% O_2, 6% CO_2, 6% H_2O, N_2 balance), SV = 30,000 h^{-1} (Kryl *et al.*, 2005). Reprinted with permission from *Indus. Eng. Chem. Res.* **44**, 9524, © 2005 American Chemical Society.

HC–SCR under specific situations, but none of them exhibits sufficient activity and durability in the entire range of operating conditions met in automobile exhaust treatment (cf. the reviews by Burch, 2004; Burch *et al.*, 2002).

Thus, special converters and advanced engine control techniques are necessary to meet the upcoming stringent NO_x emission limits. Two types of catalytic deNO_x systems for mobile applications—NSRC using periodic lean/rich operation and the SCR of NO_x by NH_3 (urea–SCR)—are discussed in Sections VI and VII, respectively.

A global kinetic expression for HC–SCR of NO was proposed by Ansell *et al.* (1996). Starting from the selectivity approach, the NO reduction rate is derived from the total rate of HC oxidation under lean conditions, i.e., the sum of the HC oxidation by O_2 (major part) and the HC oxidation by NO (minor part). The rate of NO reduction is then calculated from

$$R_{\mathrm{NO,HC-SCR}} = R_{\mathrm{C_3H_6oxidation}} \frac{K_{\mathrm{NO,HC-SCR}}\, y_{\mathrm{NO}}}{(1 + K_{\mathrm{a,O_2}})(1 + K_{\mathrm{a,NO}})} \tag{44}$$

This type of rate law is employed in the global DOC kinetic model given in Table II (cf. reaction R5). A typical evolution of the outlet NO_x concentration in the course of a slow temperature ramp is shown in Fig. 14. From this type of experiment, the selectivity and inhibition constants $K(T)$ are evaluated, considering exponential temperature dependence, Eq. (36). Again, simpler $HC + O_2 + NO$ reaction mixtures with single hydrocarbon are examined first, followed by more complex inlet gas compositions.

C. Validation and Applications of the DOC Global Kinetic Model

Application studies with the DOC model were performed using engine test bench measurements with a 6-cylinder turbocharged passenger car diesel engine. A small DOC (with the volume of approximately 0.6 dm^3) was located close to the engine, directly after the turbocharger, resulting in high space velocities (average SV = 115,000 h^{-1}, maximum up to SV = 450,000 h^{-1}) and very steep temperature gradients. These conditions made it quite demanding for simulation study of the dynamic behavior. The measured inlet and outlet temperatures in the course of an NEDC can be seen in Fig. 15, together with the evolution of the outlet temperature predicted by the 1D DOC model. We can observe that even for the close-coupled catalyst, the exhaust temperature during the first, urban driving part is quite low. On the contrary, relatively high temperature peaks can be observed in the final, extra-urban driving part. Downstream this close-coupled DOC, several configurations of other catalysts—a larger DOC, NSRC or SCR—were tested for research purposes (they will not be discussed further in this section).

Several DOCs based on similar washcoat formulation but with varying noble-metal loading (90–150 $\mathrm{g/ft}^3$ monolith) and catalyst ageing status were

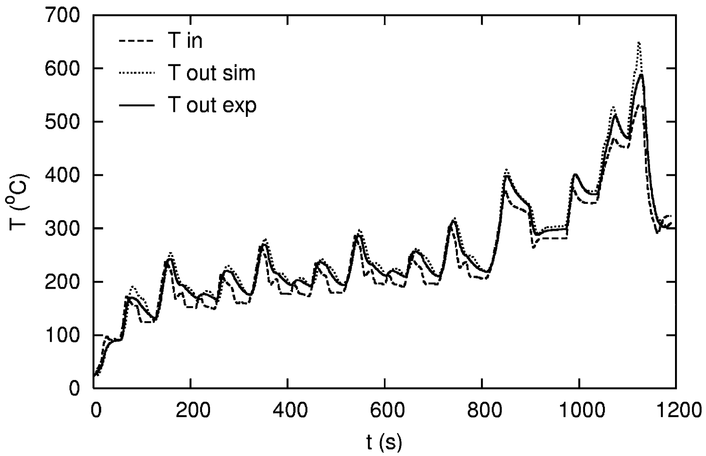

FIG. 15. DOC model validation—Measured and simulated temperatures during the NEDC. Close-coupled monolith.

studied. All monoliths used the same cordierite substrate with 400 cpsi. The original set of kinetic parameters evaluated from the laboratory experiments with the standard catalyst was calibrated individually for each catalyst by fitting only the pre-exponential factors $k_{0,j}$ of the rate constants k_j to one set of the NEDC measurements including cold start. Considering catalysts with the same washcoat structure and comparable NM dispersion (ageing level), the pre-exponential factors $k_{0,j}$ can be estimated as approximately proportional to the noble metal concentration in the washcoat.

With the DOC model calibrated for each catalyst with respect to the individual ageing status and noble metal loading, different driving cycles were studied, including FTP, US-06 and NEDC. The simulation results were validated by the corresponding measurements. The examples of simulation and experimental results for the NEDC are given in Fig. 16. The model describes the HC adsorption effect during cold start, light-off and the achieved HC conversions throughout the driving cycle for varying NM loadings and catalyst ageing levels very well.

A set-up with pre-heating during the cold start was also examined. In this case, a small uncoated metal catalyst (Emitec) was mounted before the DOC as an electrical pre-heater with power 2,000 W. The aim was to study the effect of temperature increase on DOC performance during the driving cycles. The effect of increased temperature on HC light-off after cold start follows from the comparison of Fig. 16 left top and left bottom.

A typical evolution of the concentration profiles of the adsorbed hydrocarbons in course of the NEDC, predicted by the DOC model, is illustrated in Fig. 17. This simulation is performed for a main under-floor DOC

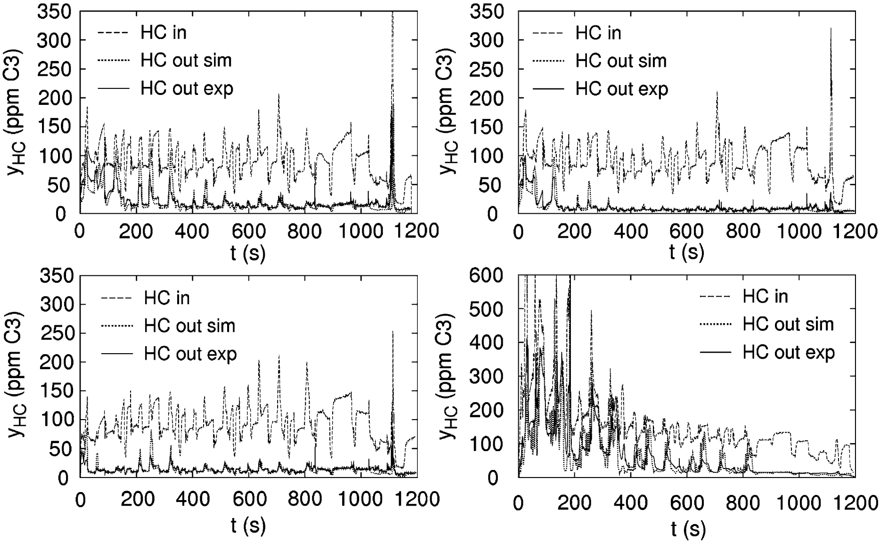

FIG. 16. DOC model validation—Measured and simulated HC concentrations during the NEDC for a close-coupled DOC monolith. Integral HC conversions X evaluated from experiment and simulation data are compared in parentheses. Top left: Pt loading 90 g/ft^3, fresh ($X^{\text{exp}} = 74.0\%$, $X^{\text{sim}} = 75.7\%$). Top right: Pt loading 140 g/ft^3, fresh ($X^{\text{exp}} = 86.7\%$, $X^{\text{sim}} = 87.6\%$). Bottom left: Pt loading 90 g/ft^3, fresh, with electrical pre-heater upstream ($X^{\text{exp}} = 83.1\%$, $X^{\text{sim}} = 84.9\%$). Bottom right: Pt loading 150 g/ft^3, aged, different engine control (raw emissions) used for this driving cycle test ($X^{\text{exp}} = 55.6\%$, $X^{\text{sim}} = 59.9\%$).

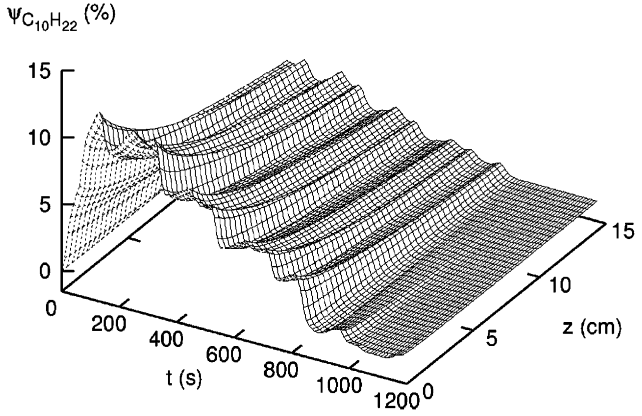

FIG. 17. Typical evolution of the concentration profiles for the adsorbed HC, predicted by the DOC model in course of the NEDC driving cycle (Kryl *et al.*, 2005).

without a close-coupled pre-catalyst, resulting in lower temperatures throughout the driving cycle. We can observe first the adsorption of hydrocarbons during the cold-start, which is reflected in the increase of the surface concentration ψ_{HC}. As the temperature increases, desorption takes place and the surface HC concentration gradually decreases. The complete removal of the heavier hydrocarbons can be observed in the extra-urban part of the driving cycle (after $t = 800\,\mathrm{s}$), when higher temperatures are met (cf. also Fig. 15).

VI. NO_x Storage and Reduction Catalyst

From the reaction-kinetic modeling point of view, the NSRC, sometimes called lean NO_x trap (LNT) or NO_x adsorber, is the most complex of the currently used automobile exhaust converters. A variety of different physical and chemical processes and the number of gas and surface components participating in typical periodic lean/rich operation form a large and closely linked system.

A. NO_x STORAGE AND REDUCTION PRINCIPLES

Primary application of the NSRC is the elimination of NO_x emissions from diesel and lean-burn gasoline engines, where direct NO_x reduction is difficult. It is operated in periodic lean/rich regime: in the course of a long lean phase (economical engine operation with lean fuel mixture, excess of air and O_2, typically lasting for several minutes) NO_x are adsorbed (stored) on the catalyst surface. Then, the accumulated NO_x are reduced within a short rich phase (injection of rich fuel mixture, excess of reducing components—CO, H_2 and HC, lasting for several seconds). A scheme of the processes on the NSRC surface during lean/rich operation is given in Fig. 18. The typical evolution of outlet NO_x concentrations in the course of stabilized periodic lean/rich operation of the NSRC is depicted in Fig. 19.

Rich conditions in the exhaust are achieved by advanced control of fuel injection, exhaust gas recirculation (EGR) management, or fuel by-passing (Dieselnet, 2007). The enrichment phases increase fuel consumption slightly, usually by 3–4%. In gasoline lean-burn engines, fuel enrichment is natural within peak-load operation (acceleration). Catalyst durability is influenced mainly by the decrease of active NO_x storage capacity, caused by thermal ageing and by sulfur poisoning. Thus, a low-sulfur fuel and proper catalyst de-sulfurization strategies have to be used (DieselNet, 2007).

The NSRC concept has been derived from the TWC—cf. Takahashi *et al.* (1996). Thus, the catalyst is also active in CO and HC oxidation reactions, as

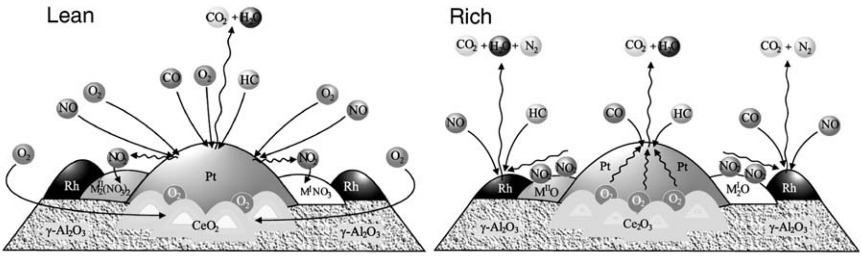

FIG. 18. Scheme of adsorption, desorption and reaction processes on the surface of the NSRC during lean and rich conditions (Kočí, 2005) (see Plate 3 in Color Plate Section at the end of this book).

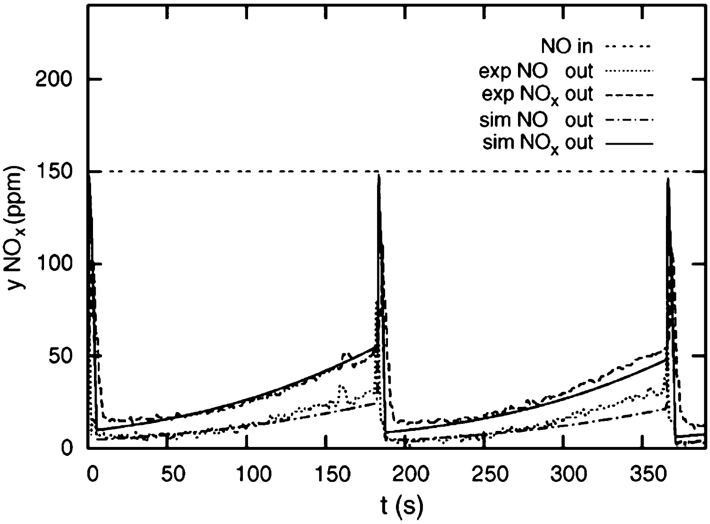

FIG. 19. Typical evolution of outlet NO_x concentrations in the course of stabilized periodic lean/rich operation of the NSRC. $T^{in} = 350°C$, lean phase 180s, rich phase 2s, SV = 30,000 h^{-1} (Kočí *et al.*, 2007b).

well as NO_x reduction under stoichiometric conditions. Typical NSRC formulation is NM/AM/Ce–ZrO_x/γ–Al_2O_3, where NM = Pt, Pd and/or Rh and AM = alkali or alkaline-earth metals (Ba, K, etc.). The noble metals form active catalytic centers for redox reactions, while the AM provide the NO_x storage capacity. Oxygen storage capacity of the Ce–Zr oxides complicates the desired NO_x reduction function during the rich phase by competitive consumption of the supplied reductants. However, the mixed Ce–Zr oxides are still present in most NSRC due to their stabilization effect on washcoat porous structure and dispersion of active components (Kašpar *et al.*, 2003).

B. DISCUSSION ON SURFACE REACTION MECHANISMS

Since the first introduction of NSRC in Japan in 1994 (Takahashi *et al.*, 1996), there has been a large, exponentially increasing number of publications dealing with different aspects of the NO_x storage and reduction catalysis—cf., e.g., the reviews by Epling *et al.* (2004a) and Burch (2004). Here we shall discuss briefly only the issues important for the development of an effective and robust mathematical model of an NSRC, which can be used for simulations in the ExACT.

Many apparent discrepancies can be found in the experimental results reported in literature for NSRC operation. They are usually caused by inconsistent experimental conditions, which have to be taken into account carefully (cf. Burch, 2004). Actual temperature, non-isothermal conditions in the test reactor, the composition of the gas mixture (presence of CO_2 and H_2O, ratio of NO/NO_2 at the inlet, the used reducing components), transport limitations and dynamics of the measurements are the most important ones.

1. NO_X *Storage: Lean Phase*

Several NO_x adsorbing components with particular temperature dependence of the effective NO_x storage capacity can be used in the NSRC washcoat. Typically, the compounds of alkali and alkaline-earth metals are employed—mostly Ba (lower-temperature operation) and K (high-temperature operation), but also Na, Ca, Li, Mg, etc. The NO_x storage capacity is in relation to the basicity of the used component (Kobayashi *et al.*, 1997). More active NO_x storage components can be (and often are) combined in one washcoat, or separated into different catalytic layers to achieve better performance (Kočí *et al.*, 2004c; Maunula *et al.*, 2001). However, the majority of the researchers consider a model catalyst with only Ba as the NO_x storage component (cf. the review by Epling *et al.*, 2004a).

A detailed sequence for NO_2 storage on BaO has been proposed after experimental observations and density-functional theory calculations by Broqvist *et al.* (2004). It involves the formation of nitrites, followed by the formation of nitrite–nitrate and nitrate–nitrate pairs on the surface, the latter being most stable. The Ba-nitrites–nitrates (NO_2–BaO–NO_2) are then transformed to $Ba(NO_3)_2$ via redox reaction, including consumption of NO_2 and release of NO. Thus, the overall reaction for the NO_2 storage on BaO with this disproportion mechanism can be written as

$$3NO_2 + BaO \rightarrow Ba(NO_3)_2 + NO$$

The same overall reaction can be obtained using a reaction mechanism with intermediate formation of Ba peroxide—cf., e.g., Lietti *et al.* (2001) and Olsson *et al.* (2001). However, it was shown that the formation of the surface peroxide is an endothermic process with respect to the formation of the NO_2–BaO–NO_2 configuration. Based on that, it was suggested that the peroxide formation is unstable toward surface nitrate formation (Broqvist *et al.*, 2004).

Experimental observations indicating the occurrence of multiple NO_x storage sites with possibly different storage mechanisms were reported by Epling *et al.* (2004b). NO_x speciation experiments showed that the NO_2 disproportion mechanism dominates at the later stages of the adsorption process. However, at the early stages of adsorption the stoichiometric relationships for this mechanism are not observed. Experimental evidence strongly suggests that this is due to presence of two distinct types of Ba-storage sites, most likely based on the proximity of Ba and Pt components. For the sites with close contact between Pt and Ba, the adsorbed oxygen can be used for the oxidation of surface nitrites to nitrates, giving the overall reaction

$$2NO_2 + \tfrac{1}{2}O_2 + BaO \rightarrow Ba(NO_3)_2$$

The effect of proximity between Pt and BaO on uptake, release and reduction of NO_x on storage catalysts was investigated by Cant *et al.* (2006). Szanyi *et al.* (2005) studied morphological changes of BaO/Al_2O_3 during NO_2 uptake and release.

Other authors (Kabin *et al.*, 2006; Nova *et al.*, 2004, 2006b) proposed alternative pathways in which, in the presence of oxygen, NO is directly adsorbed to form Ba nitrites which are progressively oxidized to nitrates, without a previous formation of gaseous NO_2. The summary reaction for this NO adsorption route (including the oxidation of nitrites to nitrates) is

$$2NO + \tfrac{3}{2}O_2 + BaO \rightarrow Ba(NO_3)_2$$

In such a mechanism, the presence of noble metals appears to facilitate the formation of intermediate nitrite species, while a close proximity between Pt and Ba seems to play an important role in enhancing this route against the NO_2 disproportion route (Nova *et al.*, 2005). The NO storage mechanism was already included in older semi-empirical NSRC models (e.g., Kočí *et al.*, 2004c; Kojima *et al.*, 2001) reflecting the fact that the experimentally observed NO_x storage cannot be described solely by the NO_2 adsorption route (particularly at lower temperatures).

In contact with gas mixtures containing water and carbon dioxide (which is the case in real automobile exhaust gas), the NO_x storage sites can be in the form of hydroxyls or carbonates, respectively. The following order of stability for different Ba-species have been observed by Lietti *et al.* (2001): $BaO < Ba(OH)_2 < BaCO_3 < Ba(NO_3)_2$. The NO_x storage is then competitive and it is accompanied by the release of H_2O and CO_2. The inhibition of NO_x storage by H_2O and CO_2 was studied, e.g., by Epling *et al.* (2004b). Because H_2O and CO_2 are always present in automobile exhaust gas, their influence on NO_x storage capacity is usually implicitly included in the description of NO_x storage.

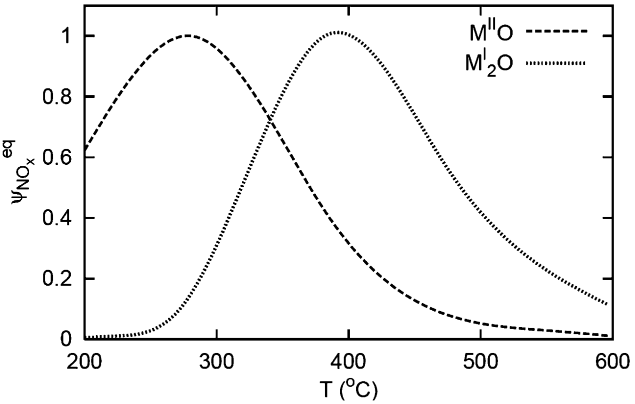

FIG. 20. Typical temperature dependence of the effective NO_x storage capacity for low- and high-temperature NO_x storage components (here denoted $M^{II}O$ and M^{I}_2O, respectively) in the washcoat of a NSRC (Kočí *et al.*, 2004c).

A study dealing with the effect of oxygen content in the gas mixture was carried out already by Takahashi *et al.* (1996). They found that the amount of the stored NO_x increases with the increasing oxygen content in the gas phase. This increase is significant for lower O_2 concentrations, while for higher O_2 content the observed NO_x storage capacity is practically constant. This was confirmed by many other studies (cf. the review by Epling *et al.*, 2004a).

Thermogravimetric measurements of NO_x storage in Ba/Pt/γ-Al_2O_3 catalyst were performed by Muncrief *et al.* (2004). The weight of the sample was followed in the course of NO_x adsorption at different temperatures, and also in the course of periodic lean/rich operation. Formation of carbonates, nitrites and nitrates was considered. From the mass balances it followed that only a minor part of total Ba moles is effectively utilized in the NO_x storage under common operating conditions. The maximum NO_x storage capacity was found to be a decreasing function of temperature (due to decreasing stability of the surface nitrates). However, a major part of the NO_x storage capacity at low temperatures turned out to be inaccessible in practical operation, due to extremely slow saturation (in the order of hours). Considering the effective (utilizable) NO_x storage capacity, a typical dependence with a maximum at intermediate temperatures is observed (cf. Fig. 20).

2. *Reduction of the Stored NO_X: Rich Phase*

Two mechanisms contribute to the removal of the stored NO_x from the surface: (i) chemical reactions with reducing components (CO, H_2, HC) present during the rich phase and (ii) thermal decomposition of surface nitrites and nitrates (heat is liberated by the reaction of CO, H_2 and HC with spare oxygen).

The latter mechanism is significant only for higher temperatures (> 300°C). Nova *et al.* (2006c) demonstrated that the co-presence of the NO_x storage element and noble metal on the same support is necessary for the reduction of the stored nitrates. The effects of various reducing components and noble metals on NO_x storage and reduction operation of $NM/BaCO_3/\gamma\text{-}Al_2O_3$ (NM = Pt, Pd, Rh) were studied, e.g., by Kobayashi *et al.* (1997) and Abdulhamid *et al.* (2006a). The order of the observed NO_x storage capacity in dependence on the used noble metal was Pt > Pd > Rh, while the order of NO_x reduction ability was opposite. Typically, bi-metallic formulations are used in NSRCs. They provide better results than single metal ones in terms of oxidation activity, NO_x trapping, NO_x reduction activity and also in removal of surface sulfur compounds inhibiting the NSRC process (Epling *et al.*, 2004a). The order of activity observed by Abdulhamid *et al.* (2006a) for the NO_x reducing components was $H_2 > CO > C_3H_6 > C_3H_8$.

The influence of rich-phase duration, gas composition and temperature on NO_x conversion over periodic lean/rich operation in the presence of H_2O and CO_2 was studied also by Kočí *et al.* (2007b). They reported *in situ* production of H_2 by the reactions of CO and C_3H_6 with water. A similar extent of NO_x reduction was observed at temperatures above 300°C when using equivalent amounts of H_2, CO and C_3H_6. However, the reduction by hydrogen still resulted in highest NO_x conversions. This observation suggested the presence of internal diffusion limitations in the porous catalytic washcoat (hydrogen exhibits the highest effective diffusivity of the reductants). The typical dependence of the achieved integral NO_x conversion on inlet temperature and length of the rich phase is depicted in Fig. 21 (Kočí *et al.*, 2004c). If the rich

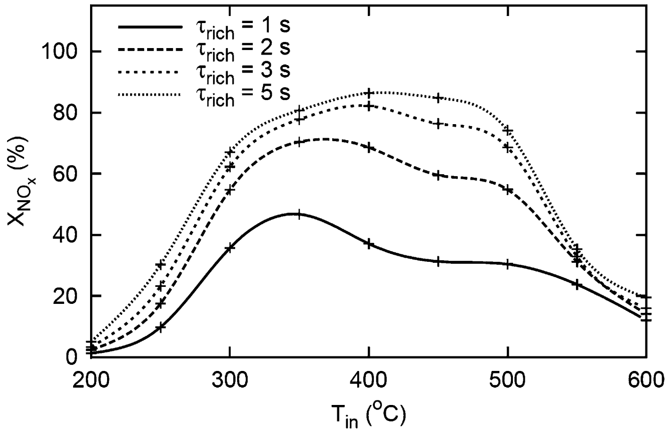

FIG. 21. Typical dependence of the integral NO_x conversion on the length of the rich phase for different temperatures of the inlet gas. Periodic lean/rich operation of the adiabatic, high-temperature NSRC. $\tau_{lean} = 95s$, $SV = 30{,}000\,h^{-1}$ (Kočí *et al.*, 2004c).

phase is too short, then the stored nitrogen oxides are not fully reduced and the number of free storage sites for the next lean phase is lower, resulting in lower NO_x conversion. However, as soon as the NO_x storage capacity is fully regenerated, the application of a longer rich phase is pointless—it increases the fuel consumption and brings no improvement to NO_x storage efficiency.

Choi *et al.* (2006) studied the intra-channel evolution of concentration and temperature profiles during regeneration of monolithic $Pt/K/Al_2O_3$ NSRC by CO in the presence of CO_2 and H_2O and they observed two regeneration phases. The first one was related to the consumption of spare oxygen and evolution of corresponding exotherms caused by $CO+O_2$ and $CO+NO_x$ reactions, with N_2 as major product of NO_x reduction. The second one was characterized by the production of H_2 (water gas shift) and NH_3 as major product of NO_x reduction.

Pihl *et al.* (2006) explained the absence of NH_3 as a by-product of the NO_x reduction during the first part of the regeneration phase by a surface-reduction front moving downstream the reactor, in front of which the formed NH_3 can be re-oxidized back to N_2. Thus, an NH_3 peak in the exhaust is expected to occur after the surface-reduction front reaches the monolith outlet. Cumaranatunge *et al.* (2007) proved experimentally that ammonia is an active intermediate in the regeneration of NSRC with H_2., i.e. H_2 can react with NO_x producing NH_3, which in turn is able to reduce the remaining NO_x stored downstream the reactor. When NH_3 is used directly at the reactor inlet instead of H_2, the NO_x reduction process is equivalent and equally effective.

The dynamics of the entire NSRC regeneration process is further influenced by: (i) the actual status of the surface prior to enrichment (NO_x saturation, ratio of nitrites and nitrates, cf. Forzatti *et al.*, 2006); (ii) surface oxygen storage effects in the NSRC washcoat (Kočí *et al.*, 2007b); (iii) internal transport in the porous catalytic layer, possibly including the transport within the storage nanoparticles (Hepburn *et al.*, 1996, 1998; Tuttlies *et al.*, 2004) and (iv) the presence of two types of NO_x storage sites—"fast" ones in proximity of noble metal sites and "slow", isolated ones (Epling *et al.*, 2004b).

The simultaneous removal of NO_x and soot on $Pt\text{-}Ba/Al_2O_3$ NSRC was investigated by Castoldi *et al.* (2006). They concluded that the presence of soot does not affect the NO_x reduction activity of the NSRC, while the soot combustion is enhanced by the presence of NO_2. This principle has been already utilized by Toyota in the integrated DPNR (diesel particulate and NO_x reduction) system (Nakatani *et al.*, 2002).

Long-term poisoning of the NO_x storage components by sulfur and phosphorus contained in fuel and lubricants leads to gradual decrease of the effective NO_x adsorption capacity. The sulfates formed on the NO_x storage sites are more stable than the nitrates, and special de-sulfurization techniques need to be applied from time to time to keep the NSRC effectiveness on a reasonable level (cf., e.g., Dieselnet, 2007). The NSRC poisoning by different sulfur compounds (SO_2, H_2S and COS) was examined by Amberntsson *et al.* (2002).

Abdulhamid *et al.* (2006b) studied by means of *in situ* FTIR spectroscopy the effects of water on the interaction of SO_2 with $Pt/BaCO_3/Al_2O_3$ NSRC. The mechanisms of sulfur poisoning and regeneration of a commercial NO_x storage catalyst for lean-burn gasoline engines were discussed by Rohr *et al.* (2005). Sakamoto *et al.* (2006) used a Pt/Ba thin-film model catalyst to study NO_x and SO_x adsorption and demonstrated that NO_x and SO_x were adsorbed all over the model catalyst. NO_x desorption occurred preferentially in an area of a few micrometers around the platinum and was suppressed at all other sites, whereas SO_x desorption occurred preferentially in an area a few nanometers wide around the platinum. Matsumoto *et al.* (2000) proposed more sulfur-tolerant NO_x sorbents based on the addition of Ti in the NSRC washcoat ($Pt/Ba/TiO_2/Al_2O_3$).

3. NSRC Kinetic Models

Several different models were proposed for the slow NO_x storage process, while only few details and approximate models are available for the highly transient NO_x reduction within the rich phase, lasting only several seconds. The models can be divided into two groups, depending on whether the internal diffusion in the particles of the NO_x storage material is considered explicitly, or this effect is included implicitly into the evaluated kinetic parameters. The models can be further differentiated by the level of complexity for the reaction kinetics description, i.e., either (simplified) microkinetic scheme or the global kinetics.

One of the first mathematical models for the NSRC was developed by Hepburn *et al.* (1996, 1998), who introduced a shrinking-core model of the mass transport in the NO_x storage material particles (Ba) and validated the results by both laboratory experiments and vehicle test data. Jirát *et al.* (1999a) proposed a model using a global and straightforward description of the NO_x storage and reduction processes incorporating the possible internal diffusion effects into the effective values of the reaction kinetic parameters. This simplified approach was further developed and validated with laboratory and engine test bench data for different types of NO_x storage catalysts by Kočí *et al.* (2004c, 2007b) and Güthenke *et al.* (2007a, b). The intra-particle diffusion model was implemented in global kinetic models by, e.g., Tuttlies *et al.* (2004), Olsson *et al.* (2005) and Scholz *et al.* (2007). In the latter work, three different forms of the NO_x storage sites (surface, bulk and semi-bulk) with independent kinetic parameters were defined.

Olsson *et al.* focused on microkinetic models aiming to describe in detail the transient steps in the NO_x storage and reduction process. First, the NO oxidation sub-model on $Pt/\gamma\text{-}Al_2O_3$ and $Pt/BaO/\gamma\text{-}Al_2O_3$ was developed (Olsson *et al.*, 1999), then the NO_x storage sub-model (Olsson *et al.*, 2001) and finally the mean-field microkinetic NO_x storage and reduction model (Olsson *et al.*, 2002), where NO_x reduction by propene was considered. Intra-particle diffusion was not assumed in this case. However, the detailed microkinetic models, even using a simplified exhaust gas composition and a limited number of possible reaction steps, turned out to be too complicated and time-consuming for routine simulations of automotive exhaust gas converters under the wide range of real operating conditions. This resulted in the development of an independent global kinetic model (Olsson *et al.*, 2005).

Concurrently with the work on the first microkinetic models, the semi-empirical models with global kinetic approach were further developed, using transient kinetics only for the oxygen and NO_x storage/reduction (cf., e.g., Kojima *et al.*, 2001; Kočí *et al.*, 2004c). In this case, a more detailed composition of the exhaust gas (different HCs, CO, H_2, water, etc.) and a wider set of reactions were considered while keeping a relatively low number of kinetic parameters and reasonable computation times. The extensions included the NO_x reduction by individual reductants with different light-off temperatures (CO, H_2 and HC) and the implementation of oxygen storage effects and reactions with water (water gas shift and steam reforming). This type of models focused also on the correct prediction of CO and HC conversions and the corresponding temperature effects, particularly during cold start and rich peaks (Kojima *et al.*, 2001). Empirical temperature dependence of the effective NO_x storage capacity was obtained by interpolating the experimentally evaluated values from isothermal adsorption experiments at individual temperatures.

Sharma *et al.* (2005) developed a 1D two-phase model for the analysis of periodic NO_x storage and reduction by C_3H_6 in a catalytic monolith, based on a simplified kinetic scheme. They focused on the evaluation of temperature and reaction fronts along the monolith and their effect on NO_x conversion. Kim *et al.* (2003) proposed a phenomenological control-oriented lean NO_x trap model.

The global kinetic models using empirical temperature dependence of the effective NO_x storage capacity can be calibrated for different types of the NSRC, containing, e.g., Ba- or K-based NO_x storage components optimized for the low- and high-temperature operation, respectively. Simulations of dynamically operated NSRC with differentiated washcoat (containing two different catalytic layers in one channel) were also performed (Kočí *et al.*, 2004c).

C. Development of Effective NSRC Kinetic Model

We can observe from the above references that different NSRCs share some common properties, but actual kinetic behavior depends on the washcoat structure details and actual state of the catalyst evolved under reaction conditions and also varies due to effects of ageing and poisoning mainly by sulfur-containing species. Hence, robust, partly phenomenological models appear to be useful in modeling commercial catalysts under varying exhaust conditions following from different engine operation characteristics. We shall discuss in the following an example of such a model, its development and application (Kočí *et al.*, 2004c, 2007b; Güthenke *et al.*, 2007a, b).

1. Selection of Model Reactions for the NSRC

The robust NSRC model has to be valid in the complete range of operating conditions encountered in vehicles, considering particularly the wide temperature range from cold start up to 500–600°C. Quite often NSRC models are developed and tested only for the intermediate temperatures (250–400°C), where effective NO_x storage is practically independent of temperature, and the catalyst is above light-off temperature. Furthermore, the model has to describe correctly not only the NO_x storage and reduction phenomena, but also CO and HC light-off and conversions and the related temperature effects (reaction exotherms) that are closely linked.

For example, an incorrect prediction of the CO, H_2 and HC reaction rates with the spare oxygen in the rich phase results in (i) an inaccurate temperature profile inside the reactor with possible differences in the order of several tens of Kelvins and (ii) misleading concentrations of the CO, H_2 and HC available for the reduction of the stored NO_x. These discrepancies may in turn result in a wrong prediction of the NSRC regeneration extent and thus also in an incorrect simulation of the NO_x emissions in the next lean/rich period, regardless of how sophisticated and well calibrated the employed NO_x storage and reduction model is. The other reactions involved in the network are oxygen storage and reduction on the catalyst surface (influencing the balance of the reductants during the rich phase) and reactions of CO and HC with water (*in situ* production of H_2). The balance of H_2 is quite important from the point of view of NO_x reduction selectivity toward NH_3.

The NSRC model reaction scheme can be seen in Table III. The model contains basic CO, H_2, HC and NO oxidation reactions that take place also in the DOC or TWC (reactions R1–R5 in Table III, cf. also Section III), and an oxygen storage sub-model typical for the TWC (reactions R11–R14 in Table III, cf. Kočí *et al.*, 2007b; Koltsakis *et al.*, 1997). NO_x storage, desorption and reduction are described by reactions R15–R23 in Table III. An effective combination of pseudo-stationary kinetics for CO, H_2, HC and NO oxidation, water gas shift and steam reforming (reactions R1–R9) and transient kinetics with an explicit consideration of the most important surface components (oxygen and NO_x storage, reactions R11–R23 in Table III) is proposed (Kočí *et al.*, 2007b). Possible internal diffusion effects for the NO_x storage processes (cf. Section VI.B) are implicitly included in the evaluated kinetic parameters. In this way, the complexity of the reaction scheme and the number of kinetic parameters are kept on a low level, while the model is still able to describe and quantify the most important phenomena of NSRC. This enables fast and efficient dynamic simulations of the NSRC necessary for the routine use in the ExACT software environment (Güthenke *et al.*, 2007a, b).

The oxygen and NO_x storage phenomena are characterized by the maximum effective storage capacities Ψ^{cap}, temperature-dependent relative saturation coverages $\psi^{\mathrm{eq}}(T)$ and kinetic constants $k_j(T)$ determining the dynamics of the

TABLE III

MODEL REACTIONS FOR NO_x STORAGE AND REDUCTION CATALYST

Reaction step	Reaction rate	No.
$CO + \frac{1}{2}O_2 \rightarrow CO_2$	$R_1 = \frac{k_1 y_{CO} y_{O_2}}{G_1}$	R1
$H_2 + \frac{1}{2}O_2 \rightarrow H_2O$	$R_2 = \frac{k_2 y_{H_2} y_{O_2}}{G_1}$	R2
$C_3H_6 + \frac{9}{2}O_2 \rightarrow 3H_2O + 3CO_2$	$R_3 = \frac{k_3 y_{C_3H_6} y_{O_2}}{G_1}$	R3
$C_{10}H_{22} + \frac{31}{2}O_2 \rightarrow 11H_2O + 10CO_2$	$R_4 = \frac{k_4 y_{C_{10}H_{22}} y_{O_2}}{G_2}$	R4
$NO + \frac{1}{2}O_2 \leftrightarrow NO_2$	$R_5 = \frac{k_5 (y_{NO} y_{O_2}^{0.5} - y_{NO_2}/K_{y,5}^{eq})}{G_1}$	R5
$H_2O + CO \leftrightarrow H_2 + CO_2$	$R_6 = k_6 (y_{CO} y_{H_2O} - y_{CO_2} y_{H_2}/K_{y,6}^{eq})$	R6
$3H_2O + C_3H_6 \rightarrow 6H_2 + 3CO$	$R_7 = k_7 (y_{C_3H_6} y_{H_2O} - y_{CO}^3 y_{H_2}^6/(K_{y,7}^{eq} y_{H_2O}^2))$	R7
$NO + CO \rightarrow CO_2 + \frac{1}{2}N_2$	$R_8 = k_8 y_{CO} y_{NO}^{0.5}$	R8
$NO + H_2 \rightarrow H_2O + \frac{1}{2}N_2$	$R_9 = k_9 y_{H_2} y_{NO}^{0.5}$	R9
$9NO + C_3H_6 \rightarrow 3CO_2 + \frac{9}{2}N_2 + 3H_2O$	$R_{10} = k_{10} y_{C_3H_6} y_{NO}^{0.5}$	R10
$Ce_2O_3 + \frac{1}{2}O_2 \rightarrow 2CeO_2$	$R_{11} = k_{11} \Psi_{O_2}^{cap} y_{O_2} (\psi_{O_2}^{eq} - \psi_{O_2})$	R11
$CO + 2CeO_2 \rightarrow CO_2 + Ce_2O_3$	$R_{12} = k_{21} \Psi_{O_2}^{cap} y_{CO} \psi_{O_2}$	R12
$H_2 + 2CeO_2 \rightarrow H_2O + Ce_2O_3$	$R_{13} = k_{13} \Psi_{O_2}^{cap} y_{H_2} \psi_{O_2}$	R13
$\frac{1}{9}C_3H_6 + 2CeO_2 \rightarrow \frac{1}{3}CO_2 + Ce_2O_3 + \frac{1}{3}H_2O$	$R_{14} = k_{14} \Psi_{O_2}^{cap} y_{C_3H_6} \psi_{O_2}$	R14
$2NO_2 + \frac{1}{2}O_2 + BaCO_3 \rightarrow Ba(NO_3)_2 + CO_2$	$R_{15} = k_{15} \Psi_{NO_x}^{cap} y_{NO_2} y_{O_2}^{0.1} (\psi_{NO_x}^{eq} - \psi_{NO_x})^2$	R15
$2NO + \frac{3}{2}O_2 + BaCO_3 \leftrightarrow Ba(NO_3)_2 + CO_2$	$R_{16} = k_{16} \Psi_{NO_x}^{cap} y_{NO} y_{O_2}^{0.1} (\psi_{NO_x}^{eq} - \psi_{NO_x})^2$	R16
$5CO + Ba(NO_3)_2 \rightarrow BaO + 5CO_2 + N_2$	$R_{17} = \frac{k_{17} \Psi_{NO_x}^{cap} y_{CO} \psi_{NO_x}^2}{G_3}$	R17
$5H_2 + Ba(NO_3)_2 \rightarrow BaO + 5H_2O + N_2$	$R_{18} = \frac{k_{18} \Psi_{NO_x}^{cap} y_{H_2} \psi_{NO_x}^2}{G_3}$	R18
$\frac{5}{9}C_3H_6 + Ba(NO_3)_2 \rightarrow BaO + \frac{5}{3}CO_2 + \frac{5}{3}H_2O + N_2$	$R_{19} = \frac{k_{19} \Psi_{NO_x}^{cap} y_{C_3H_6} \psi_{NO_x}^2}{G_3}$	R19
$3CO + Ba(NO_3)_2 \rightarrow BaO + 3CO_2 + 2NO$	$R_{20} = \frac{k_{20} \Psi_{NO_x}^{cap} y_{CO} \psi_{NO_x}^2}{G_4}$	R20
$3H_2 + Ba(NO_3)_2 \rightarrow BaO + 3H_2O + 2NO$	$R_{21} = \frac{k_{21} \Psi_{NO_x}^{cap} y_{H_2} \psi_{NO_x}^2}{G_4}$	R21
$\frac{1}{3}C_3H_6 + Ba(NO_3)_2 \rightarrow BaO + H_2O + 2NO + CO_2$	$R_{22} = \frac{k_{22} \Psi_{NO_x}^{cap} y_{C_3H_6} \psi_{NO_x}^2}{G_4}$	R22
$BaO + CO_2 \rightarrow BaCO_3$	$R_{23} = \sum_{j=17}^{22} R_j$	R23

Note:

$$G_1 = (1 + K_{a,1} y_{CO} + K_{a,2} y_{C_3H_6})^2 (1 + K_{a,3} y_{CO}^2 y_{C_3H_6}^2)(1 + K_{a,4} y_{NO_x}^{0.7}) T^s$$

$$G_2 = 1 + K_{a,5} y_{C_{10}H_{22}}, \ G_3 = 1 + K_{a,6} y_{O_2}, \ G_4 = (1 + 0.1 K_{a,6} y_{O_2})(1 + K_{a,7} y_{NO_x})$$

All molar fractions *y* are considered locally in catalyst pores, the superscript "s" is omitted for brevity.

processes. For the oxygen storage, only the "fast" oxygen storage capacity (Lambrou *et al.*, 2004; Yao and Yu Yao, 1984) is considered because of the rich phase time-scale (several seconds).

For NO_x storage, a model with two types of the NO_x storage sites (the "fast" and "slow" sites) was also considered, however, the average NO_x storage site model employing the empirical second-order rate law (cf. reactions R15–R22 in Table III and Güthenke *et al.*, 2007a, b; Kočí *et al.*, 2007b) turned out to be sufficiently accurate in most of applications, while having less tunable parameters. The NO_x storage rate laws given in Table III are able to predict both the fast NO_x uptake at the beginning of the adsorption phase, and the slow storage process close to the saturation, in agreement with experimental observations (cf. the review by Epling *et al.*, 2004a).

The NO_x storage process cannot be described only by the reaction pathway assuming first NO oxidation to NO_2 and then the consecutive NO_2 storage (the nitrate route only, cf. Section VI.B.1), particularly at lower temperatures when the NO oxidation is slow. Based on experimental results, a second pathway considering the storage of NO (the nitrite route) is present in most of the NSRC models (cf., e.g., Güthenke *et al.*, 2007a, b; Kočí *et al.*, 2004c, 2007b; Olsson *et al.*, 2005; Scholz *et al.*, 2007).

In the presented model (Güthenke *et al.*, 2007a, b; Kočí *et al.*, 2007b) the decomposition of the stored NO_x in the rich phase is considered in two ways—(i) NO desorption (reactions R20–R22 in Table III) followed by the catalytic reduction of the desorbed NO reactions R8–R10 in Table III) and (ii) direct reduction of the stored NO_x (reactions R17–R19 in Table III) accounting for the spill-over from the NO_x storage site to an adjacent NM site (cf. Fig. 18). Three different NO_x reductants are distinguished—H_2, CO and C_3H_6. Individual kinetic parameters, light-off temperatures and effective diffusivities are considered for these model components (cf. Kočí *et al.*, 2007b).

2. *Evaluation of Model Kinetic Parameters*

The model kinetic parameters—rate constants $k_j(T)$, inhibition constants $K_a(T)$, maximum effective storage capacities Ψ^{cap} and temperature-dependent relative saturation coverages $\psi^{eq}(T)$—were fitted by minimization of the weighted least-squares objective function from the measured and simulated data, Eq. (35), employing an adaptive simplex optimization algorithm. This was done successively for the kinetic reactions in Table III to minimize the number of parameters estimated simultaneously (Kočí *et al.*, 2007b): (i) CO, H_2 and HC oxidation light-off, first individually under both lean and rich conditions, then in mixtures including inhibition effects, (ii) water gas shift and steam reforming (hydrogen production) under rich conditions, (iii) NO reduction by CO, H_2 and C_3H_6, (iv) NO/NO_2 transformation, (v) NO_x storage, including temperature dependence of effective NO_x storage capacity, (vi) oxygen storage and reduction, including temperature dependence of effective oxygen storage capacity and (vii) NO_x desorption and reduction by CO, H_2 and C_3H_6 under rich conditions. In each step of the evaluation, the already obtained kinetic parameters have been kept constant.

Laboratory experiments designed to study the transient behavior of an NSRC (Kočí *et al.*, 2007b; Waldbüsser, 2005) were performed to obtain suitable data for the evaluation of the global kinetic parameters. A commercial NO_x storage catalyst material of the type NM/Ba/CeO_2/γ-Al_2O_3 washcoated on a cordierite substrate with wall thickness of 0.11 mm and channel hydraulic diameter of 1.06 mm was investigated. Monolith samples of the size approximately 8 cm^3 were studied in two arrangements: (i) one sample in a quasi-adiabatic microreactor (Daimler AG, Stuttgart; cf. Waldbüsser, 2005) and (ii) three identical samples arranged in series, placed in modular, nearly isothermal steel microreactor (Institute of Chemical Technology, Prague; cf. Kočí *et al.*, 2005, 2007b; Monolith, 2007).

One set of experiments was conducted on fresh catalyst material. Pretreatment of the fresh catalyst samples was 1 h on stream at 500 °C, lean conditions and then 1 h lean/rich operation at 300 °C. After that, no significant change of catalyst activity and very minor change of storage capacity were observed in the course of the experimental series. A second set of experiments was conducted on specifically aged catalyst material, equivalent to a catalyst after 80,000 km passenger car use. The ageing level was obtained by applying DPF regenerations and de-sulfurizations consecutively (Güthenke, 2007b; Waldbüsser, 2005).

The laboratory experiments were performed either with slowly increasing temperature ramp (the light-off experiments for CO, H_2 and HC oxidation, water gas shift and steam reforming, cf. Fig. 22), or with constant inlet temperature (the storage experiments and lean/rich switching, cf. Figs. 24 and 25). Lean exhaust gas was provided by synthetic gases (Kočí *et al.*, 2007b), or by a one cylinder engine at a constant load (Waldbüsser, 2005), rich exhaust was supplied using synthetic gas mixtures.

Examples of light-off experimental data for CO and C_3H_6 oxidation are given in Fig. 22a b, together with the simulated outlet concentrations. The respective kinetic parameters—the rate constants $k_j(T)$ and the inhibition constants $K_a(T)$—were evaluated from experimental data by the weighted least squares method, Eq. (35).

At first, the rate constants were determined from experiments with individual simple lean mixtures (i.e., $CO + O_2$ and $C_3H_6 + O_2$), then the self-inhibition constants were evaluated employing the data measured for simple rich mixtures and finally the cross-inhibition constants were optimized using the results of light-off experiments with complex lean and rich mixtures, without and with NO (Kočí *et al.*, 2007b). The effects of lean vs. rich composition (i.e., self-inhibition by high CO and HC concentrations) and the inhibition by NO can be clearly seen from Fig. 22a and b. The observed light-off temperatures for the individual reductants were always in the order $H_2 < CO < C_3H_6$ at corresponding conditions. The global kinetic model was able to describe the large variations of reaction rate and light-off temperature under the studied lean and rich conditions.

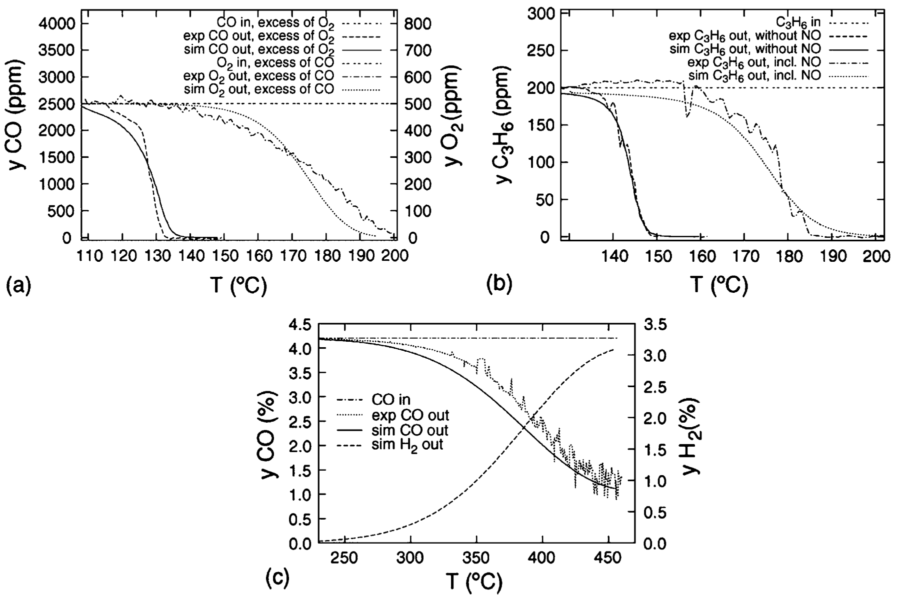

FIG. 22. Experimentally observed and simulated light-off curves for fresh NSRC. (a) CO oxidation, influence of lean (excess of O_2) and rich (excess of CO) conditions. Composition of inlet gas (mol. fractions)—lean mixture: 0.25% CO, 7% O_2; rich mixture: 0.25% CO, 0.05% O_2. (b) C_3H_6 oxidation, influence of inhibition by NO. Composition of inlet gas (mol. fractions): 200 ppm C_3H_6, 0.25% CO, 7% O_2 and 0 or 150 ppm NO. (c) Water gas shift—production of hydrogen, composition of inlet gas (mol. fractions): 4.2% CO, 0.0% O_2. All gas mixtures: 10% H_2O, 10% CO_2 and balance N_2. Temperature ramp 3 K/min (Kočí *et al.*, 2007b).

Water gas shift and steam reforming reactions producing H_2 under rich conditions (reactions R6 and R7 in Table III, respectively) start to be significantly active at the temperatures above 300 °C (cf. Fig. 22c. These reactions result in a different actual CO:C_3H_6:H_2 concentration ratio inside the monolith in comparison with the raw exhaust gas, or the synthetic rich inlet gas mixture used in the lab experiments (Kočí *et al.*, 2007b). The reactions with water are characterized by the evaluated rate constants $k_j(T)$ as well as by the thermodynamic equilibrium constants $K^{eq}(T)$.

The optimum NO_x storage catalyst should exhibit quite low oxygen storage capacity to efficiently utilize the excess of CO, H_2 and HC in the rich phase for the NO_x reduction. However, it is practically impossible to produce the catalyst with zero oxygen storage capacity because Ce–Zr oxides are used for the stabilization of the washcoat structure (Kašpar *et al.*, 2003). Experiments with step changes between oxygen and individual reductants (CO, H_2 and C_3H_6) were performed at different temperatures to study the oxygen storage effects (reactions R11–R14 in Table III). It can be seen from the example given in Fig. 23 that the effective oxygen storage capacity increases monotonously with

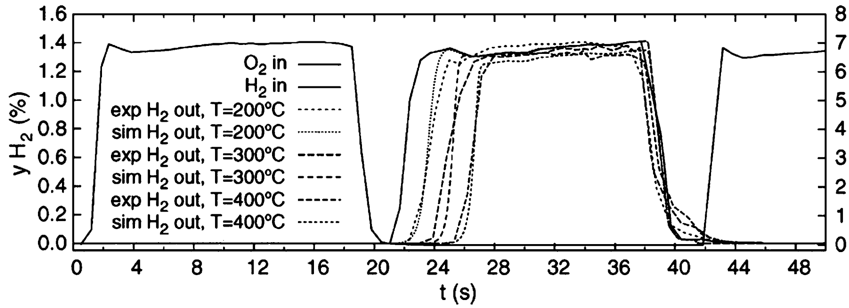

FIG. 23. Experimentally observed and simulated oxygen storage and reduction; fresh NSRC. Composition of inlet gas (mol. fractions)—lean mixture: 7% O_2, 0% H_2; rich mixture: 1.4% H_2, 0% O_2; both mixtures: 10% H_2O, 10% CO_2, balance N_2 (Kočí *et al.*, 2007b).

temperature, which is in agreement with other experimental observations (e.g., Boaro *et al.*, 2004). At higher temperatures, the amount of reductants consumed during the rich phase by reactions with stored oxygen cannot be neglected. From these experiments, the model parameters $\Psi_{O_2}^{cap}$and $\psi_{O_2}^{eq}(T)$ and $k_{11}(T)$–$k_{14}(T)$ are evaluated (Kočí *et al.*, 2007b).

The NO_x storage experiments were performed for temperatures ranging from 150°C to 500°C and space velocities from 30,000 to 90,000 h^{-1}. Prior to the measurements, the catalyst was fully regenerated at 400°C by rich gas mixture with the composition corresponding to an air/fuel ratio of 12.8 for 60 s. For constant lean inlet gas composition, temperature and space velocity, isothermal NO_x adsorption as well as NO/NO_2 transformation were measured to evaluate the NO_x storage dynamics and the storage capacity ($\Psi_{NO_x}^{cap}$and $\psi_{NO_x}^{eq}(T)$) of the catalyst, cf. Fig. 24.

To investigate the regeneration behavior, lean-rich switches were applied periodically. Temperature and space velocity were varied as specified above. Lean and rich phase durations were varied in the range of 60–300 s and 3–7 s, respectively, with the rich phase composition corresponding to an air/fuel ratio between 12.8 and 13.6 (Waldbüsser, 2005). For each experiment, lean/rich switching was repeated until stabilized periodic operation was obtained, cf. Fig. 25. The kinetic parameters for the desorption and reduction of the stored NO_x (reactions R17–R22 in Table III) were evaluated from a set of experiments conducted with several different rich-phase lengths at individual temperatures (Güthenke *et al.*, 2007b).

For the fresh and the specifically aged catalyst materials, the dependence of the normalized NO_x storage capacity on temperature could be kept the same (Güthenke *et al.*, 2007b). This minimized the number of parameters to be re-adapted for two catalysts with different ageing level. Thus, only the maximum NO_x storage capacity Ψ^{cap} and the pre-exponential factors for the reactions R1–R22 had to be re-evaluated, cf. Table III and Eq. (36).

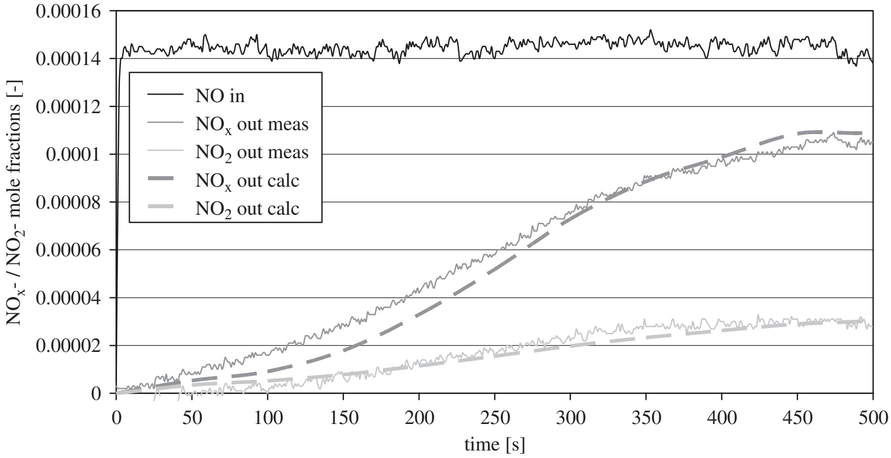

FIG. 24. Fitting of kinetic parameters to isothermal adsorption experiment—comparison of measured (meas) and calculated (calc) outlet NO_x concentrations. Fresh catalyst, $SV = 60{,}000\,h^{-1}$, $T = 200°C$, lean gas composition: 145 ppm NO_x, 4% CO_2, 4% H_2O, 18% O_2 (Güthenke *et al.*, 2007a).

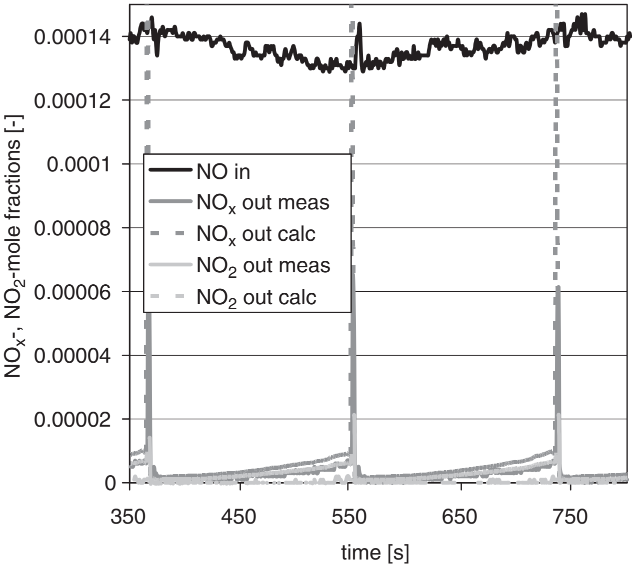

FIG. 25. Evaluation of the kinetic parameters for the stored NO_x reduction. Comparison of the measured and calculated (calc) outlet NO_x concentrations; fresh NSRC. Lean/rich experiment (180s/5s), $SV = 60{,}000\,h^{-1}$, $T^{in} = 350°C$ (Güthenke *et al.*, 2007b). Reprinted with permission from SAE Paper # 2007-01-1117 © 2007 *SAE International.*

D. NSRC Model Validation and Simulation Results

Examples of the results obtained with the spatially 1D model utilizing global NSRC kinetics are given in Figs. 26–33. The reaction kinetic model was validated with real exhaust measurement data from passenger car and heavy-duty commercial vehicle to ensure applicability in the full range of operating conditions encountered. The kinetic equations and the parameters were kept constant for all validation calculations.

For passenger car applications, FTP-75 driving cycle data obtained during vehicle dynamometer test (Waldbüsser, 2005) are shown in Figs. 26–28 (Güthenke *et al.*, 2007a). The NSRC was operated at an average space velocity of 42,000 h^{-1}. The exhaust temperature in front of and behind the NSRC is shown in Fig. 26, the measured and predicted outlet temperatures are in a good agreement. Evolution of the predicted and measured instantaneous NO_x emissions at the NSRC outlet during the test cycle is given in Fig. 27. The corresponding integrated (cumulative) NO_x emissions, including the effect of fluctuating flow-rate, are then depicted in Fig. 28. The cumulative values are normalized by the integrated inlet (raw) NO_x emissions over the complete test cycle. The simulated emissions match the measurement results very well; the agreement was reached also for the CO and HC conversions.

The evolution of the spatially averaged NO_x coverage ψ_{NOx} (i.e., the amount of the NO_x stored in the converter) in the course of the FTP cycle can be seen in Fig. 28. At the test start, the catalyst is fully regenerated. Time intervals with

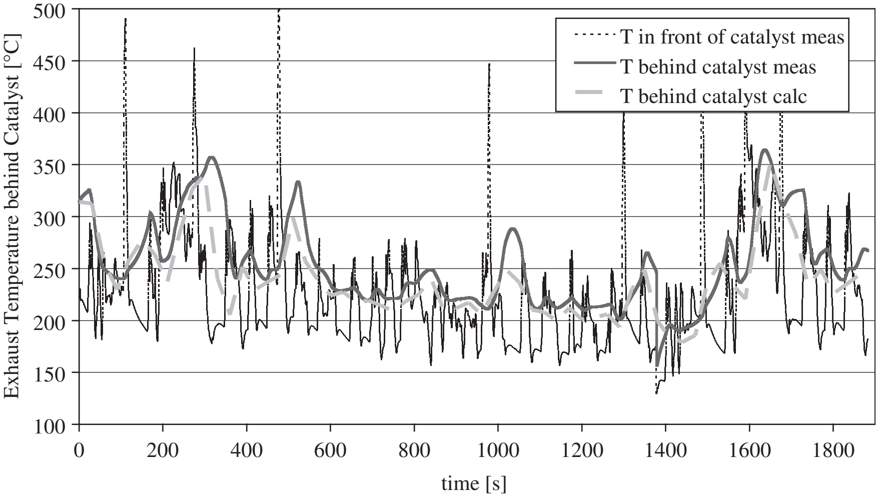

FIG. 26. Validation of the NSRC model for passenger car application—comparison of measured (meas) and calculated (calc) outlet temperatures during the FTP-75 driving cycle; fresh catalyst (Güthenke *et al.*, 2007a) (see Plate 4 in Color Plate Section at the end of this book).

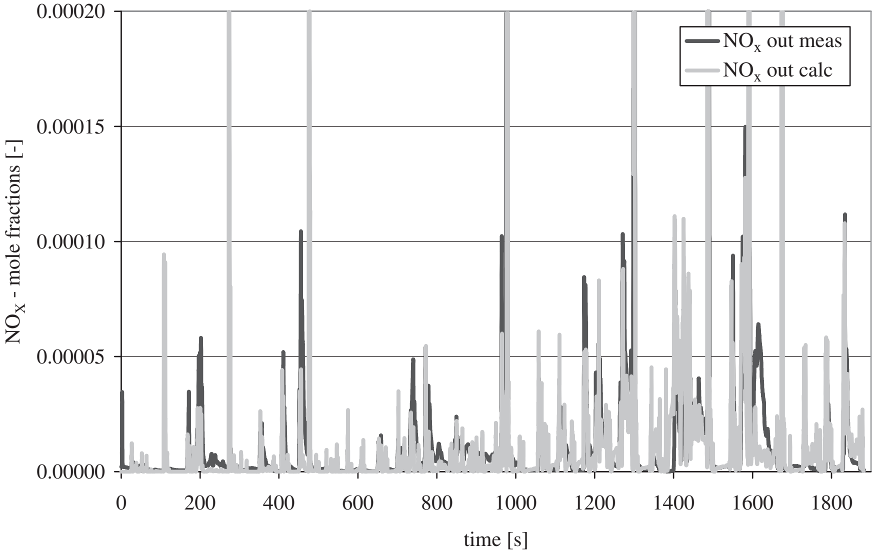

FIG. 27. Validation of the NSRC model for passenger car application—comparison of measured (meas) and calculated (calc) evolution of instantaneous NO$_x$ emissions during the FTP-75 driving cycle; fresh catalyst (Güthenke *et al.*, 2007a). For comparison of respective integral emission data cf. Fig. 28. Integral NO$_x$ conversions X evaluated from experiment and simulation data: $X^{exp} = 88.9\%$, $X^{sim} = 88.3\%$.

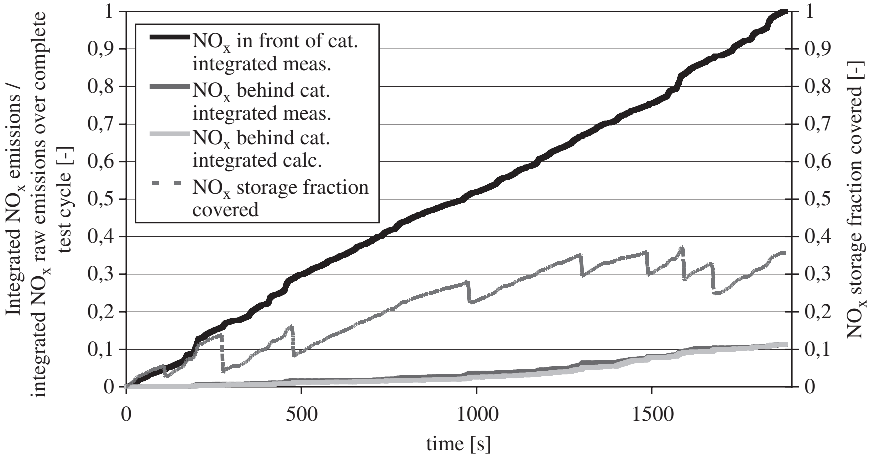

FIG. 28. Validation of the NSRC model for passenger car application—comparison of measured (meas) and calculated (calc) cumulative NO$_x$ emissions for the FTP-75 driving cycle; fresh catalyst (Güthenke *et al.*, 2007a). The covered fraction of the NO$_x$ storage capacity (spatially averaged ψ_{NOx}) is calculated by the model. Integral NO$_x$ conversions X evaluated from experiment and simulation data: $X^{exp} = 88.9\%$, $X^{sim} = 88.3\%$ (see Plate 5 in Color Plate Section at the end of this book).

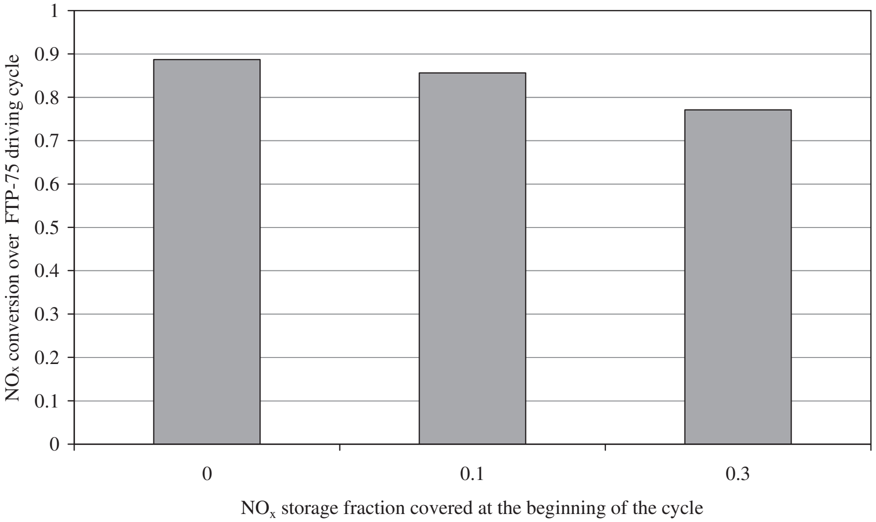

FIG. 29. Predicted variation of the NO_x conversion over the FTP-75 driving cycle in dependence on the catalyst regeneration status at the beginning (i.e., initial ψ_{NO_x}); fresh NSRC (Güthenke *et al.*, 2007a).

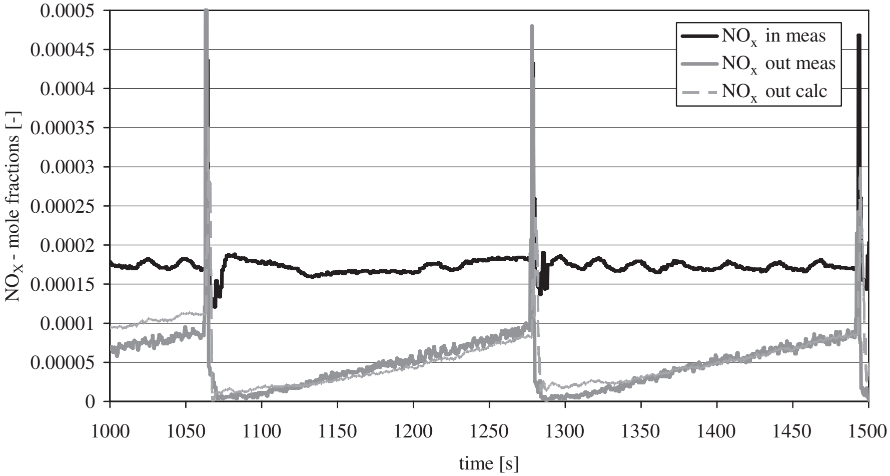

FIG. 30. Validation of the NSRC model for heavy-duty commercial vehicle application—comparison of measured (meas) and calculated (calc) outlet NO_x concentrations for the ESC load point B50; fresh catalyst (Güthenke *et al.*, 2007a).

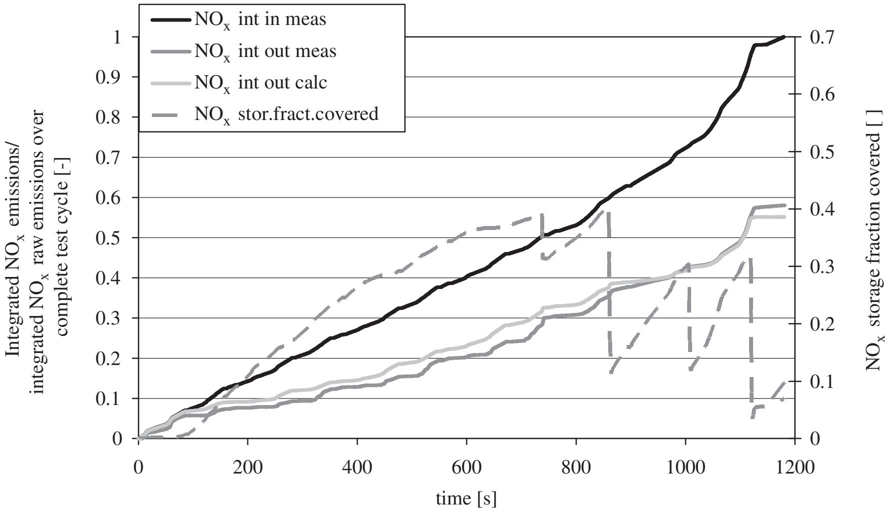

FIG. 31. Validation of the NSRC model for passenger car application—comparison of measured (meas) and calculated (calc) cumulative NO_x emissions for the NEDC driving cycle; aged catalyst (Güthenke *et al.*, 2007b). The covered fraction of the NO_x storage capacity (spatially averaged ψ_{NO_x}) is calculated by the model. Reprinted with permission from SAE Paper # 2007-01-1117 © 2007 *SAE International*. Integral NO_x conversions X evaluated from experiment and simulation data: $X^{exp} = 42.0\%$, $X^{sim} = 44.3\%$.

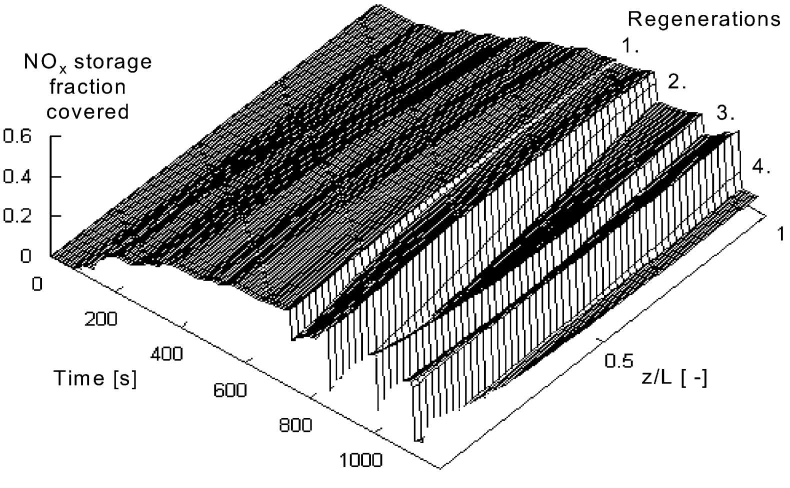

FIG. 32. Computed spatiotemporal concentration profile of the stored NO_x for the NEDC driving cycle; aged NSRC. The z/L stands for the dimensionless spatial coordinate along the monolith: 0 is at the inlet, 1 at the outlet (Güthenke *et al.*, 2007b). Reprinted with permission from SAE Paper # 2007-01-1117 © 2007 *SAE International.*

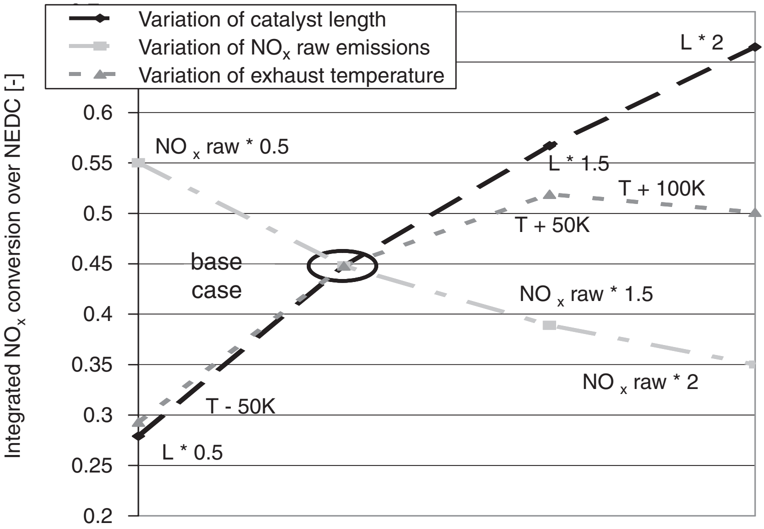

FIG. 33. Influence of catalyst length, NO_x raw emissions and exhaust temperature on the integral NO_x conversion over NEDC; aged NSRC (Güthenke *et al.*, 2007b). Reprinted with permission from SAE Paper # 2007-01-1117 © 2007 *SAE International.*

monotonously increasing NO_x coverage correspond to lean engine operation with NO_x adsorption, while a sudden decrease of the NO_x coverage (i.e., catalyst regeneration) is observed during the short enrichment phases. Variations in rich phase conditions (duration, temperature and gas composition) influence the extent of catalyst regeneration (cf., e.g., Güthenke *et al.*, 2007a, b; Kočí *et al.*, 2004c, 2007b). Effects of different operating/regenerating strategies on the conversion can thus be investigated.

The presented example FTP test is finished with a non-zero NO_x coverage, i.e., the catalyst is not fully regenerated at the end of the driving cycle (cf. Fig. 28). The extent of the regeneration has a significant influence on the NO_x conversions during a NSRC operation, yet it cannot be easily measured. The NSRC model balances the most important surface components (NO_x and O_2) and thus delivers information on the covered NO_x storage fraction. Figure 29 shows the result of a simulation study on the influence of the initial NO_x coverage on the conversions over the following FTP driving cycle (Güthenke *et al.*, 2007a). When the catalyst is not fully regenerated at the end of the previous cycle, the NO_x conversion varies considerably. Such results help to explain unexpected measurement results during the development process and improve long-term reproducibility and predictability of the exhaust system.

For heavy-duty commercial vehicle application, validation data from an engine test bench were used. Two different NSRC volumes were employed, 7 times and 3.5 times larger than that for the passenger car application. Various operating points from ESC measurements (cf. Section II) were simulated, resulting in space velocities ranging from 36,000 to 135,000 h^{-1}. The engine operating points were stationary concerning load and rotations and controlled lean/rich switches were applied until stabilized behavior of the catalyst was reached. The evolution of the NO_x concentrations in front of and behind the NSRC for the operating point B50 is depicted in Fig. 30 (Güthenke *et al.*, 2007a).

An example of the results for the aged NSRC is given in Fig. 31, where the predicted and measured NO_x emissions are compared for a passenger car NEDC. The simulation was performed employing the model parameterization for the specifically aged catalyst material and NEDC vehicle dynamometer measurements (Waldbüsser, 2005) were used for the validation. Keeping the same temperature dependence of the normalized NO_x storage capacity $\psi^{eq}(T)$ for the fresh and the aged catalyst, and using the maximum NO_x storage capacity Ψ^{cap} and the pre-exponential factors for the reactions R1–R22 evaluated from the laboratory experiments, a good agreement between measurements and simulations can be reached (Güthenke *et al.*, 2007b).

The corresponding spatio-temporal concentration profile of the stored NO_x calculated for the studied case is depicted in Fig. 32. The evolution of the exhaust gas temperature is similar to that given for the DOC in Fig. 15 (Section V.C), but at generally lower temperature level than for the close-coupled DOC. Thus, it is quite a demanding task to effectively regenerate the aged NSRC during cold start operation. During the first rich phase only the front of the catalyst is regenerated and the concentration of the stored NO_x decreases only slightly in the rear part of the monolith, where the lowest temperature and concentrations of reductants are met. For the second and the third rich phase, the regeneration is also better at the front than at the rear part of the catalyst. During the last rich phase, almost the entire length of the catalyst is fully regenerated. This is due to a longer rich phase and higher catalyst temperatures met in the extra-urban part of the driving cycle.

On the base case given in Fig. 31, several parametric studies were conducted. Catalyst length and NO_x raw emissions were varied between 0.5 and 2 times the original value. Figure 33 shows that the integrated conversion over the driving cycle increases with increasing catalyst length and decreases with increasing raw emissions. These effects are quite intuitive, however, note that the dependence is not linear. The exhaust temperature was varied with respect to the base case between 50 K less and 100 K more. With the temperature increased by 50 K, the NO_x conversion increases. For the base case temperature profile plus 100 K, it decreases again, as the optimum working temperature of the NSRC is exceeded. Decreased thermal stability of barium nitrates leads to a lower storage capacity (cf. the discussion in Section VI.B.1). The model also gives the possibility to study the effect of concurrent changes. For example, if the NO_x raw emissions are increased by a factor of 1.5 for the studied case, a 2.3 times long NSRC is necessary to achieve the same cumulative NO_x emissions behind catalyst over the NEDC (Güthenke *et al.*, 2007b).

VII. Selective Catalytic Reduction of NO_x by NH_3 (Urea–SCR)

In this section the methods described in Sections III and IV are applied to derive a dynamic numerical model of the SCR of NO–NO_2 with NH_3 over a commercial $V_2O_5/WO_3/TiO_2$ extruded monolith catalyst. The extension of the same dynamic model to a zeolite-based catalyst is currently in progress (Chatterjee *et al.*, 2007).

The SCR with NH_3/urea is emerging as the most promising technology for the abatement of NO_x emissions from diesel vehicles (ACEA, 2003; Heck *et al.*, 2002). This has stimulated a renewed interest in the investigation of fundamental aspects of the SCR catalytic chemistry, also in view of the need of the transportation industry to develop design and simulation tools incorporating SCR kinetic schemes.

Indeed, NH_3–SCR over vanadia-type catalysts, wherein one molecule of NO is reduced by one molecule of ammonia in the presence of oxygen to give harmless dinitrogen and water, according to the standard SCR reaction, R1 in Table IV, has represented for the last two decades the most effective commercial $deNO_x$ process for stack gases from power plants and other stationary sources (Forzatti *et al.*, 2002). However, the specific demands of mobile applications, associated, e.g., with onboard ammonia storage, volume limitations, dynamic operation and extensive functional T-windows, do not permit a straightforward transposition of the technology. Particularly, since the working conditions for mobile applications may be much colder than in stationary installations, the increase of $deNO_x$ activity at low temperatures represents a major development goal. A possible solution to this issue is represented by the so-called fast SCR reaction known since the early 1980s, when Kato and co-workers (Kato *et al.*, 1981) found that the reaction involving an equimolar NO and NO_2 feed mixture, R2 in Table IV, is remarkably faster than the standard SCR, reaction, in the field of low temperatures ($T < 300\,^{\circ}C$). In practical terms, a preoxidation catalyst located upstream of the SCR catalyst

TABLE IV
STANDARD AND FAST SCR REACTIONS

Reaction step		No.
$2NH_3 + 2NO + \frac{1}{2}O_2 \rightarrow 2N_2 + 3H_2O$	Standard SCR reaction	R1
$2NH_3 + NO + NO_2 \rightarrow 2N_2 + 3H_2O$	Fast SCR reaction	R2

could convert a fraction of NO in the engine exhausts to NO_2 in order to approach the optimal NO/NO_2 equimolar feed ratio of the fast SCR reaction (Koebel *et al.*, 2002). Nevertheless addition of NO_2 to the SCR reacting system introduces considerable complexity resulting from the multiplication of primary and secondary reaction routes, and may result in the formation of such undesired byproducts as NH_4NO_3 and N_2O (Ciardelli *et al.*, 2007a; Madia *et al.*, 2002).

In this section we present the derivation of a detailed kinetic model of the full NO/NO_2–NH_3 reacting system over a commercial $V_2O_5/WO_3/TiO_2$ catalyst, whose intrinsic rate expressions have been then incorporated into a transient 2D (1D + 1D) mathematical model of the SCR honeycomb monolith reactor to predict the dynamic behavior of real full-scale converters. The overall reaction scheme adopted in the kinetic model is summarized in Table V, and discussed in details in the following paragraphs. It is worth emphasizing that the present modeling effort relies on (and complements) a fundamental investigation of both the standard and the fast SCR catalytic mechanisms, whose elucidation proved to be critical for effective design and operation of $deNO_x$ aftertreatment devices.

In line with the general guidelines presented in Section IV, the catalyst in powder form has been at first considered in order to estimate the intrinsic SCR kinetics. For the sake of clarity, the experimental work was organized according to a stage-wise approach of growing complexity: first the simplest reacting system NH_3/O_2 was addressed, then NO was included to study the standard SCR reaction only, and finally, with the addition of NO_2, the full NH_3–NO–NO_2/O_2 system was investigated.

In subsequent stages validation experiments were performed over monolith catalyst samples at two different scales: (i) monolith core samples (up to $10\,cm^3$) in a laboratory rig for integral reactor experiments and (ii) full-scale honeycomb monoliths (up to 43 L in size) in engine test bench runs.

TABLE V
MODEL REACTIONS FOR V-BASED SCR CATALYSTS

Reaction step		Reaction rate	No.
$NH_3 \rightarrow NH_3^*$	NH_3 adsorption	R_{ads}	R3
$NH_3^* \rightarrow NH_3$	NH_3 desorption	R_{des}	R4
$NH_3^* + \frac{3}{4}O_2 \rightarrow \frac{1}{2}N_2 + \frac{3}{2}H_2O$	NH_3 oxidation	R_{ox}	R5
$NH_3^* + NO + \frac{1}{4}O_2 \rightarrow N_2 + \frac{3}{2}H_2O$	Standard SCR	R_{NO}	R6
$2NO_2 + H_2O \Leftrightarrow HONO + HNO_3$	NO_2 disproportion	R_{Amm}	R7
$NH_3^* + HONO \rightarrow N_2 + 2H_2O$	Decomposition of Ammonium Nitrite	R_{Nit}	R8
$NH_3^* + HNO_3 \Leftrightarrow NH_4NO_3$	Ammonium nitrate formation/ decomposition	R_{Dec}	R9
$HNO_3 + NO \Leftrightarrow HONO + NO_2$	HNO_3 reduction by NO	R_{Fst}	R10
$NH_3^* + HNO_3 \rightarrow N_2O + 2H_2O$	N_2O formation	R_{N_2O}	R11
$NH_3^* + \frac{3}{4}NO_2 \rightarrow \frac{7}{8}N_2 + \frac{3}{4}H_2O$	NO_2 SCR	R_{NO_2}	R12

While the practical implementation of the SCR deNO$_x$ technology for vehicles relies on using an urea aqueous solution as ammonia carrier, NH$_3$ being generated by decomposition and hydrolysis of urea, the present investigation has been focused on the reactivity of ammonia only: it is believed in fact that decoupling urea decomposition from NH$_3$–NO$_x$ reactions is quite helpful in effectively elucidating SCR chemistry and kinetics.

A. MICROREACTOR SCALE

1. *Testing Procedure*

The transient experiments herein described were carried out over powdered catalyst in a microreactor: a portion consisting of several grams from the original extruded monolith was crushed and sieved to a powder (140–200 mesh). One hundred and sixty milligrams of this powder, diluted with 80 mg of quartz were eventually loaded in the microreactor. Intraparticle gradients and gas–solid mass transfer limitations were ruled out by theoretical criteria (Mears, 1971).

For reproducibility purposes, a specific pre-treatment was performed whenever a fresh catalyst sample was loaded in the reactor. This typically consisted in running a temperature ramp from 50°C to 600°C at 15°C/min while feeding to the reactor 2% of oxygen in helium, with a flow of 150 cm^3/min (STP). After that the temperature was kept at 600°C for about one hour. This treatment assured total desorption of sulphate species, often present in fresh commercial V-based SCR catalysts.

The feed mixture was prepared by combining the pure synthetic reacting gases, namely ammonia, NO, NO$_2$ and oxygen. Contrary to the usual approach in the literature, helium instead of nitrogen was used as inert carrier gas, so that N$_2$, which is the main product of the SCR reaction, could be easily evaluated by the analytical system. Argon was also used as a tracer and internal standard for the analysis. The flow of each component was controlled by means of seven mass-flow meters (Brooks Inst. 5850S) connected to switchboards. Downstream of the mass-flow meters the rig was operated at atmospheric pressure. Water vapor was fed by means of a saturator through which part of the global feed stream was bubbled before entering the reactor.

Transient experiments were performed by means of two 4-way switch valves which allow a rapid cross change between inlets and outlets, so that the reactants are instantaneously fed to or released from the reactor. The same flow rate is always set for the two streams entering each valve, thus ensuring that the only variation affecting the reacting mixture is the change of reactant concentrations.

The microreactor, schematically represented in Fig. 34, consists of a quartz tube (internal diameter 6 mm) inserted in a furnace, through which the reacting

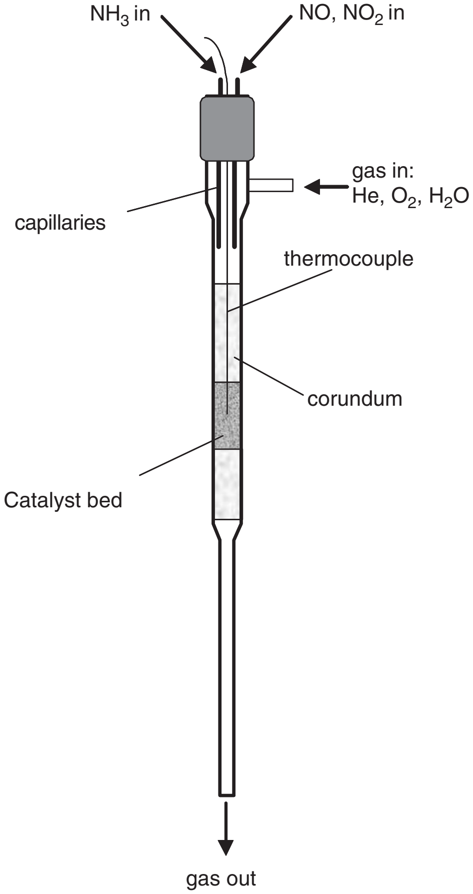

FIG. 34. Schematic diagram of the microreactor for NH_3–SCR kinetic runs.

mixture flows. The catalyst powder is placed at the depth corresponding to the isothermal zone of the furnace, between two layers of inert corundum to favor good mixing of the gaseous species. The reaction temperature is measured and controlled by a thermocouple immersed in the catalyst bed. The outlet gas is then sent to the analytical system. The entire line downstream of the reactor is traced and heated to 200°C in order to prevent deposition of ammonium nitrate, which is a possible product of the reaction between NO_2 and NH_3.

In order to secure a continuous quantitative analysis of the outlet gas mixture, including all the species necessary for the evaluation of the nitrogen atomic balance, namely NH_3, NO, NO_2 (reactants), N_2 and N_2O (products), the gases exiting the reactor were analyzed both by a Mass Spectrometer (MS) (Balzers QMS200) and by a UV analyzer (ABB Limas 11HW) in a parallel arrangement. Moreover a specific cold trap was designed for the quantification of ammonium nitrate, which is formed under particular conditions.

Operating conditions as similar as possible to those of real aftertreatment systems were chosen for the experiments: temperature range = 50–550°C, NO_x concentration range = 0–1,000 ppm, presence of water and oxygen. While real engine exhausts typically contain about 10% v/v of water and oxygen, it was not possible to feed such high concentrations in microreactor runs because of limitations related to the mass spectrometer. The effect of water and oxygen on the SCR reactivity was in any case addressed, and a good compromise was found using feed contents of 1% H_2O and 2% O_2 v/v: such conditions well represent the SCR reactivity under real conditions and at the same time allow the use of a MS analyzer. The effects of higher oxygen and water feed contents were studied at the intermediate scale over monolith core samples. Likewise, hydrocarbons and CO_2 were not added to the feed at the microreactor scale, but their effect on the SCR reactivity over V-based catalysts is known to be negligible, as later confirmed by test bench experiments.

2. NH_3/O_2 *Reacting System*

The experimental investigation started from the study of the simplest reacting system, i.e. including only ammonia and oxygen as reactants (Ciardelli *et al.*, 2004a). Two main catalytic processes are expected to occur in this case, namely the adsorption–desorption of NH_3 (R3 and R4 in Table V), and, at higher temperatures, its oxidation by gaseous oxygen (R5 in Table V). The two processes have been addressed sequentially, as discussed in the following sections.

3. NH_3 *Adsorption–Desorption*

Experimental runs - In order to obtain intrinsic kinetics of the NH_3 adsorption–desorption process as a function of temperature, the dynamics of NH_3 adsorption–desorption were studied over the commercial V-based SCR catalyst adopting the TRM: specifically, the experiments consisted in stepwise feeding 1,000 ppm of NH_3 while flowing oxygen (2%), water (1%) and balance helium at constant temperature. Depending on temperature, different amounts of ammonia were adsorbed onto the catalyst at this stage. When the catalyst adsorption capacity was saturated (outlet ammonia signal approaching the feed level), NH_3 was shut off and desorption of weakly adsorbed ammonia occurred. Then, after interrupting the oxygen feed in order to prevent ammonia oxidation, a temperature ramp at 15°C/min from 50°C to 550°C was run so to provoke complete thermal desorption of ammonia. Such experiments were typically performed at an SV of $92{,}000\,h^{-1}$.

Typical results obtained upon imposing a step change of the NH_3 feed concentration are presented in Fig. 35. The figure shows the evolution of the

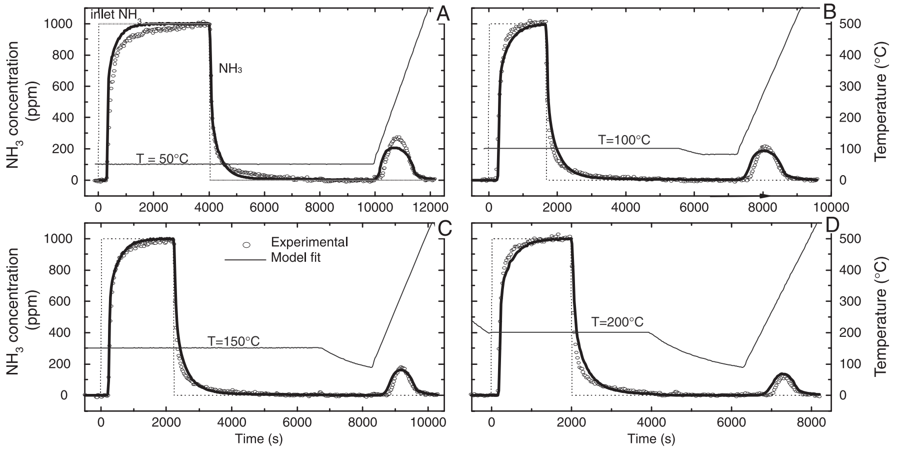

FIG. 35. Fitted results of adsorption–desorption + TPD run: SV = 92,000 h^{-1}; NH_3 = 1,000 ppm, H_2O = 1%, O_2 = 2%. (A) T = 50°C; (B) T = 100°C; (C) T = 150°C; (D) T = 200°C. Symbols: experimental; solid line: calculated.

NH_3 outlet concentration (symbols) monitored upon opening and shutting down the NH_3 feed (dotted line), at four different adsorption temperatures, namely $T = 50, 100, 150, 200$°C, followed by a TPD run.

Considering the experiment performed at 50°C, upon the NH_3 step addition (at $t = 0$ s) the NH_3 reactor outlet concentration shows a dead time, i.e. a period during which the fed NH_3 is completely adsorbed onto the catalyst surface, and then it increases with time, approaching the inlet value of 1,000 ppm after $\approx$3,500 s. Upon NH_3 shut-off ($t = 4{,}000$ s) the reactor outlet NH_3 concentration starts decreasing with time due to the desorption of previously adsorbed NH_3. However, complete desorption of NH_3 is achieved only by performing a TPD run. Indeed, as soon as the catalyst is heated, the NH_3 signal increases again reaching a maximum value at about 250°C, then it drops back to zero for temperatures higher than 450°C.

On increasing the adsorption temperature, shorter dead-times are observed in Fig. 35 (respectively $\approx$280, 220, 190 and 140 s for $T_{\text{ads}} = 50, 100, 150$ and 200°C): thus the amount of NH_3 adsorbed onto the catalyst surface is reduced, in line with the exothermic NH_3 adsorption process. Likewise the TPD runs, whose areas decrease on increasing the adsorption temperature, also confirm the lower storage capacity of the system at higher temperatures.

Kinetic analysis—The model of the test microreactor was based on the following equations, whose symbols are defined in the Notation. They represent the adaptation of the general Eqs. (33) and (34) in Section IV to the specific reacting system herein considered.

NH_3 mass balance (adsorbed phase):

$$\Omega_{\mathrm{NH_3}} \frac{\partial \theta_{\mathrm{NH_3}}}{\partial t} = R_{\mathrm{ads}} - R_{\mathrm{des}} \tag{45}$$

NH_3 mass balance (gas phase):

$$\varepsilon^{\mathrm{g}} \frac{\partial c_{\mathrm{NH_3}}}{\partial t} = -u \frac{\partial c_{\mathrm{NH_3}}}{\partial z} - (1 - \varepsilon^{\mathrm{g}})(R_{\mathrm{ads}} - R_{\mathrm{des}}) \tag{46}$$

Based on literature indications (Lietti *et al.*, 1997, 2000) and supported by preliminary fits of the experimental data, a non-activated NH_3 adsorption process and Temkin-type NH_3 desorption kinetics have been assumed, i.e.

$$R_{\mathrm{ads}} = k_{\mathrm{ads}} c_{\mathrm{NH_3}} (1 - \theta_{\mathrm{NH_3}}) \tag{47}$$

$$R_{\mathrm{des}} = k_{0,\mathrm{des}} \exp\left[-\frac{E_{\mathrm{des}}}{RT} (1 - \alpha \theta_{\mathrm{NH_3}}) \right] \theta_{\mathrm{NH_3}} \tag{48}$$

Figure 35 illustrates the comparison between experimental data (symbols) and model fitting (solid lines) after global non-linear regression on the four runs: a good agreement is evident in all cases. Particularly, the model well reproduces the dead time of the outlet NH_3 gaseous concentration, which is representative of the NH_3 storage capacity. In addition, TPD runs are fairly well fitted in terms of concentration profiles and temperature peaks in a large range of temperatures. The parameter estimates associated with the fit in Fig. 35 well compare with the corresponding estimates obtained in previous works performed over both model and commercial V-based SCR catalysts for stationary applications (Lietti *et al.*, 1997, 2000).

4. NH₃ Oxidation

The reaction of ammonia with oxygen over V-based catalysts produces mainly nitrogen, according to the stoichiometry of R5 in Table V. Analogously to the case of the ammonia adsorption–desorption, specific runs were carried out in order to extract the intrinsic kinetics of ammonia oxidation and at the same time to validate the previously fitted kinetics of the ammonia adsorption–desorption process.

Experiments including both the phases of adsorption–desorption and oxidation of ammonia were hence designed and performed. A typical run is shown in Fig. 36: at temperature of 175°C 1,000 ppm of NH_3 were stepwise fed in a stream of water (1%), oxygen (2%) and balance He, with an SV of $230{,}000\,\mathrm{h}^{-1}$. At time = 3,000 s a temperature ramp at 12°C/min was started. Adsorption of ammonia occurred as soon as NH_3 was admitted to the reactor,

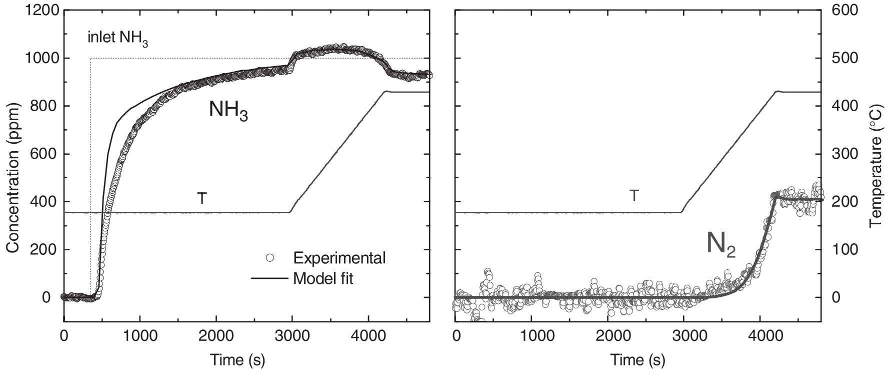

FIG. 36. Fitting of the NH_3 oxidation TPR: $SV = 210{,}000\,h^{-1}$; $NH_3 = 1{,}000$ ppm, $H_2O = 1\%$, $O_2 = 2\%$. T ramp 175–425°C at 12°C/min. Symbols: experimental; solid lines: calculated.

while its desorption was evident during the temperature ramp. Moreover, ammonia oxidation started when the catalyst temperature exceeded 350°C, as apparent from the consumption of ammonia and the production of nitrogen.

The experiment in Fig. 36 has been analyzed according to the usual plug-flow model of the test microreactor. In this case, the ammonia mass balance equations were modified in order to include the oxidation reaction R5 in Table V, which was considered to proceed via adsorbed ammonia NH_3*. Moreover, the mass balance for gaseous nitrogen was introduced

NH_3 mass balance (adsorbed phase):

$$\Omega \frac{\partial \theta}{\partial t} = R_{\mathrm{ads}} - R_{\mathrm{des}} - R_{\mathrm{ox}} \tag{49}$$

NH_3 and N_2 mass balances (gas phase):

$$\varepsilon^{\mathrm{g}} \frac{\partial c_{\mathrm{NH_3}}}{\partial t} = -u \frac{\partial c_{\mathrm{NH_3}}}{\partial z} - (1 - \varepsilon^{\mathrm{g}})(R_{\mathrm{ads}} - R_{\mathrm{des}}) \tag{50}$$

$$\varepsilon^{\mathrm{g}} \frac{\partial c_{\mathrm{N_2}}}{\partial t} = -u \frac{\partial c_{\mathrm{N_2}}}{\partial z} + (1 - \varepsilon^{\mathrm{g}}) \frac{1}{2} R_{\mathrm{ox}} \tag{51}$$

For the rate of ammonia oxidation a simple first-order rate expression in the surface concentration of ammonia has been assumed, which also considers the effect of oxygen, i.e.

$$R_{\mathrm{ox}} = k_{0,\mathrm{ox}} \exp\left(-\frac{E_{\mathrm{ox}}}{RT}\right) \left(\frac{y_{\mathrm{O_2}}}{0.02}\right)^{\beta} \theta_{\mathrm{NH_3}} \tag{52}$$

The kinetic parameters of ammonia oxidation were fitted by multiresponse nonlinear regression, while the parameter estimates for the ammonia adsorption–desorption kinetics were kept unchanged with respect to those obtained from the fit in the previous section. Notably, in this case both the NH_3 and the N_2 outlet concentrations were regarded as regression responses.

Figure 36 shows the result of the fitting in terms of experimental (symbols) and calculated (solid lines) outlet concentrations of NH_3 and nitrogen as a function of time. It is worth of note that the kinetic model is capable to capture both the onset temperature of ammonia oxidation and the slope with which it proceeds upon increasing the temperature. Moreover the ammonia adsorption–desorption dynamics, which are very demanding especially during the T-ramp, were very well predicted, thus validating the fit performed in the previous paragraph at different operating conditions of SV and heating rate.

The parameter estimates associated with the fitting in Fig. 36 well compare with other estimates for NH_3 oxidation over V-based SCR catalysts reported in the literature.

5. *NH_3–NO/O_2 Reacting System*

This represents the typical feed mixture to SCR converters when no oxidation precatalyst is applied, as for instance in the case of NO_x abatement from stationary sources. With such a feed mixture the main $deNO_x$ reaction occurring over V-based catalysts is the so-called standard SCR (R6 in Table V). Transient experiments in a wide range of temperatures (50–550°C) were performed in order to develop a suitable kinetic model of the NH_3–NO/O_2 reacting system. The study of the standard SCR kinetics was particularly focused on the characteristics that are critical for mobile applications, namely the behavior during transient operation and the reactivity in the low temperature region.

6. *Experimental*

The reactivity of the NH_3–NO/O_2 system was studied first by TPR experiments in order to explore the effects of some operative conditions, namely temperature, water and oxygen feed contents and space velocity, on the standard SCR reaction. In this case NH_3 (1,000 ppm) + NO (1,000 ppm) with O_2 (2 or 6% v/v), H_2O (1%) and balance He were initially fed at 50°C and then the catalyst temperature was continuously increased at 2 °C/min up to 450°C.

No significant influence of the water feed content on the standard SCR reaction between 1% and 10% H_2O was found, while a moderate promoting effect of oxygen on the SCR activity was clearly apparent (Chatterjee *et al.*, 2005; Ciardelli *et al.*, 2004a; Nova *et al.*, 2006a; Tronconi *et al.*, 2005). Afterwards the reactivity in dynamic conditions was systematically studied by means of TRM experiments, i.e. by performing step changes of the NH_3 feed

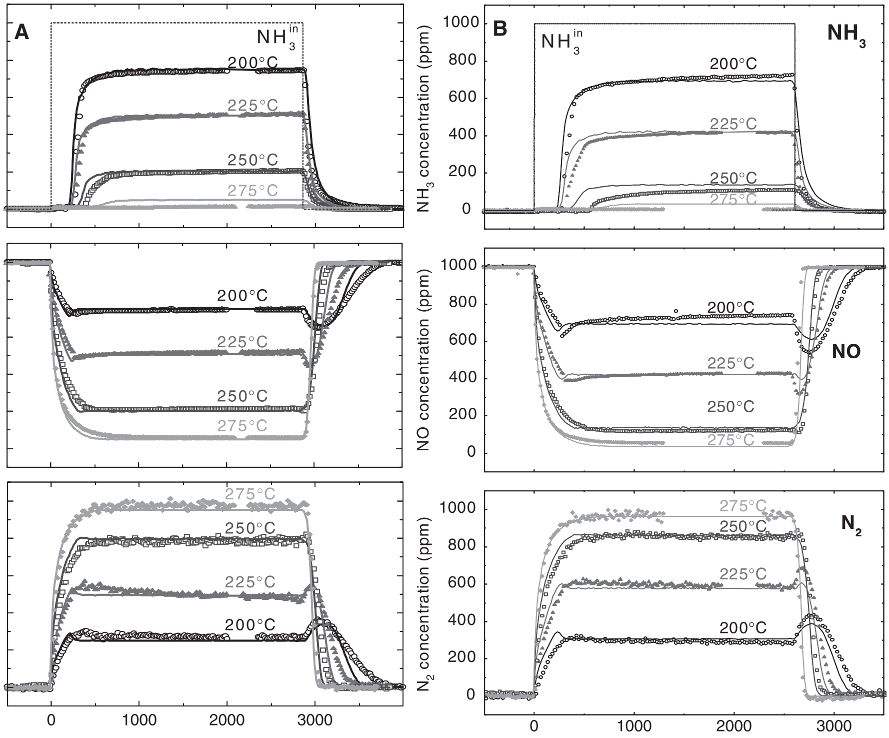

FIG. 37. Transient SCR microreactor experiments with step feed of NH_3 (0–1,000 ppm) in NO (1,000 ppm)/He + H_2O (1% v/v) + He + O_2 (2% v/v) (A) and O_2 (6% v/v (B) and at different temperatures. Symbols: measured concentrations of NH_3, NO, N_2 at reactor outlet. Lines: kinetic fitting using the modified redox rate law, Eq. (57). Reprinted with permission from Nova *et al.* (2006a).

concentration (0 → 1,000 → 0 ppm) at constant NO feed content (1,000 ppm) in the presence of water (1% v/v) and oxygen (2 and 6% v/v). The system was operated at atmospheric pressure with an $SV = 9.2 \times 10^4\,h^{-1}$.

Figure 37A (symbols) displays selected step-response TRM experiments performed with 2% O_2 at different temperatures, namely at 200, 225, 250 and 275 °C, in terms of NH_3, NO and N_2 outlet concentrations vs. time. In the run performed at $T = 250°C$ (squares), upon NH_3 step feed at $t = 0\,s$ the NH_3 outlet concentration trace exhibited a dead time ($\approx 250\,s$) and then slowly grew with time on stream, eventually approaching a steady-state value of about 200 ppm, that is much lower than the ammonia feed concentration level (1,000 ppm). In correspondence to the NH_3 admittance to the reactor, a sudden drop of the NO outlet concentration was observed together with a mirror-like increment of the N_2 concentration, associated with the start-up of the SCR reaction. The levels of NH_3, NO and N_2 at steady state were in fact consistent with the stoichiometry of the standard SCR reaction (R6, Table V), with a conversion close to 80%. Following shutdown of the ammonia feed ($t = 1{,}500\,\mathrm{s}$) the concentrations of NH_3, NO and N_2 slowly recovered their feed levels, as all the ammonia still adsorbed on the catalyst surface was progressively depleted by the reaction with nitric oxide.

The dynamic features described above are common to all the experiments performed in the high temperature range (above 250°C): Fig. 37A (diamonds) shows, e.g., also the run at 275°C, at which temperature almost complete steady-state conversion of the reactants was approached. On the contrary, the experiments performed at lower temperatures, i.e. 225°C (Fig. 37A, triangles) and 200°C (circles), exhibited a different dynamic behavior of NO and N_2 during both the NH_3 start-up phase and the NH_3 shut-off transient. The more significant effect was observed when the NH_3 feed concentration was restored to 0 ppm ($t = 1{,}500\,\mathrm{s}$): the NO outlet concentration first decreased, passed through a minimum and then began to increase due to the depletion of adsorbed ammonia. A symmetrical evolution was observed for N_2, thus proving that during the transient phase of ammonia shutdown, when only adsorbed NH_3 was reacting with NO continuously fed to the reactor, the deNO_x activity of the system was temporarily enhanced until complete depletion of the residual NH_3 on the catalyst surface. This evidently confirms that excess ammonia inhibits the SCR reaction, as already pointed out by several authors (Kapteijn *et al.*, 1993; Koebel and Elsener, 1998; Nova *et al.*, 2000; Willey *et al.*, 1991).

A minor transient feature was also manifested when ammonia was admitted to the reactor ($t = 0\,\mathrm{s}$): the NO outlet concentration immediately decreased, went through a weak minimum near 150 s and finally slightly increased, reaching steady state in correspondence of the end of the ammonia feed phase ($t \approx 2{,}800\,\mathrm{s}$). Again, the nitrogen evolution was symmetrical to that of NO. The same ammonia inhibition effect invoked to explain the enhancement in the deNO_x conversion at ammonia shutdown can explain this transient behavior, too. In fact both features suggest the existence of an optimal ammonia surface concentration, which is lower than the coverage established at steady state.

It is worth of note that such transient effects due to NH_3 inhibition were most evident at the lowest investigated temperature (200°C), but gradually vanished upon increasing the reaction temperature, i.e. reducing the amount of adsorbed NH_3 present on the catalyst surface, and were no longer visible at $T \geq 250\,^{\circ}\mathrm{C}$.

Transient kinetic experiments were performed also in the presence of a higher concentration of oxygen, namely 6% v/v. Results collected at different temperatures are displayed in Fig. 37B (symbols) in terms of NH_3, NO and N_2 outlet concentration traces vs. time ($T = 200$, 225, 250, 275°C). They are qualitatively similar to those with 2% v/v oxygen feed in Fig. 37A and discussed above. Particularly, two different behaviors of the NO and the N_2 concentration traces were again observed when the NH_3 feed was opened up/shut down. In the high-T range, monotonic temporal evolutions were observed: e.g. at NH_3

shutdown they slowly recovered their feed levels, using up the ammonia still adsorbed on the catalyst surface. In the low T-range, again maxima–minima behaviors became apparent: thus, at ammonia shutdown the NO concentration (and symmetrically the N_2 production) decreased at first, went through a minimum, then began to increase and approached its steady-state value. Thus, the higher oxygen content did not alter the dynamic features of the transient experiments, and in particular the ammonia inhibiting action was still evident to a similar extent, particularly at ammonia shut-down.

The main effect of the higher oxygen concentration was a slight enhancement of the SCR conversion, as measured by the steady state levels of ammonia, NO and nitrogen: for example at 250°C, 780 ppm of nitrogen were measured at steady state when 2% oxygen was fed to the reactor (see Fig. 37A), while in the presence of 6% of oxygen the SCR reaction produced 820 ppm of nitrogen (see Fig. 37B).

6. *Kinetic Analysis*

The kinetic analysis of the whole set of transient data collected over the powdered SCR catalyst has been addressed using the dynamic 1D isothermal heterogeneous plug-flow model of the test microreactor (Chatterjee *et al.*, 2005; Ciardelli *et al.*, 2004a) described in Section IV.

The following reactions were included in the kinetic model: NH_3 adsorption (R3 in Table V), NH_3 desorption (R4 in Table IV), NH_3 oxidation (R5 in Table IV) and standard SCR (R6 in Table V). Mass balances for adsorbed ammonia and nitrogen now include the standard SCR reaction. Moreover, the mass balance of gaseous NO was introduced, too

(a) adsorbed phase:

$$\mathrm{NH}_3^* \quad \Omega \frac{\partial \theta_{\mathrm{NH}_3}}{\partial t} = R_{\mathrm{ads}} - R_{\mathrm{des}} - R_{\mathrm{ox}} - R_{\mathrm{NO}} \tag{53}$$

(b) gas phase:

$$\mathrm{NH}_3 \quad \varepsilon^{\mathrm{g}} \frac{\partial c_{\mathrm{NH}_3}}{\partial t} = -u \frac{\partial c_{\mathrm{NH}_3}}{\partial z} - (1-\varepsilon^{\mathrm{g}})(R_{\mathrm{ads}} - R_{\mathrm{des}}) \tag{54}$$

$$\mathrm{N}_2 \quad \varepsilon^{\mathrm{g}} \frac{\partial c_{\mathrm{N}_2}}{\partial t} = -u \frac{\partial c_{\mathrm{N}_2}}{\partial z} + (1-\varepsilon^{\mathrm{g}})\left(R_{\mathrm{NO}} + \frac{1}{2} R_{\mathrm{ox}}\right) \tag{55}$$

$$\mathrm{NO} \quad \varepsilon^{\mathrm{g}} \frac{\partial c_{\mathrm{NO}}}{\partial t} = -u \frac{\partial c_{\mathrm{NO}}}{\partial z} - (1-\varepsilon^{\mathrm{g}}) R_{\mathrm{NO}} \tag{56}$$

The reactions of adsorption–desorption of NH_3 and ammonia oxidation to N_2 were considered with the kinetic expressions shown in Section V.A.2.b.

The peculiar dynamic effect attributed to the inhibition effect of ammonia was accounted for by a dual-site modified redox (MR) rate law (Nova *et al.*, 2006a)

$$R_{NO} = \frac{k_{0,NO} e^{-E_{NO}/RT} c_{NO} \theta_{NH_3}}{\left(1 + K_{NH_3}(\theta_{NH_3}/1 - \theta_{NH_3})\right)\left(1 + k_{O_2}(c_{NO}\theta_{NH_3}/y_{O_2}^{1/4})\right)} \tag{57}$$

The MR rate law relies on the assumption that the SCR reaction is governed by a redox mechanism and therefore predicts a kinetic dependence on oxygen. It has been derived assuming that: (i) two types of sites for NH_3 adsorption (acidic non-reducible sites) and for $NO+NH_3$ activation/reaction (redox sites, associated with vanadium), respectively, prevail on the catalyst surface; (ii) NH_3 blocks the redox sites; (iii) reoxidation of the redox sites is rate controlling.

A global multiresponse non-linear regression was performed to fit Eq. (57) to all the runs with both 2% and 6% v/v O_2 feed content to obtain the estimates of the kinetic parameters (Nova *et al.*, 2006a). Figure 37 (solid lines) illustrates the adequacy of the global fit of the TRM runs with 2 and 6% O_2: the MR rate law can evidently capture the complex maxima–minima NO and N_2 traces (symbols) at low T at both NH_3 startup, that a simple Eley–Rideal (ER), approach based on the equation

$$R_{NO} = k_{0,NO} \exp\left(-\frac{E_{NO}}{RT}\right) c_{NO} \theta_{NH_3} \tag{58}$$

was found unable to reproduce (Nova *et al.*, 2006a).

The MR kinetic model has been then validated on a predictive basis by comparing its simulations with experimental data from microreactor runs consisting of high frequency NH_3 feed pulses in a stream of 1,000 ppm of NO, 2% O_2 and 1% H_2O at 180 °C (Nova *et al.*, 2006a; Tronconi *et al.*, 2005). The experimental signals (see Fig. 38, symbols) were in line with the abovementioned ammonia inhibition effect, exhibiting a characteristic transient behavior characterized by the greatest NO conversion after the NH_3 shut down. The experiments were simulated using both the MR, Eq. (57), and the ER, Eq. (58), rate expressions. The results confirmed that changing the $deNO_x$ rate equation from the ER- to the new MR kinetic model improved significantly the description of fast SCR transients similar to those associated with the operation of SCR aftertreatment devices for vehicles at low temperature.

Accordingly, we conclude that the dual-site MR approach is compatible with the ammonia inhibition effects observed during unsteady SCR experiments, as well as with the oxygen dependence of the SCR kinetics at low temperatures, and can be successfully applied to simulate the complex dynamic behavior of

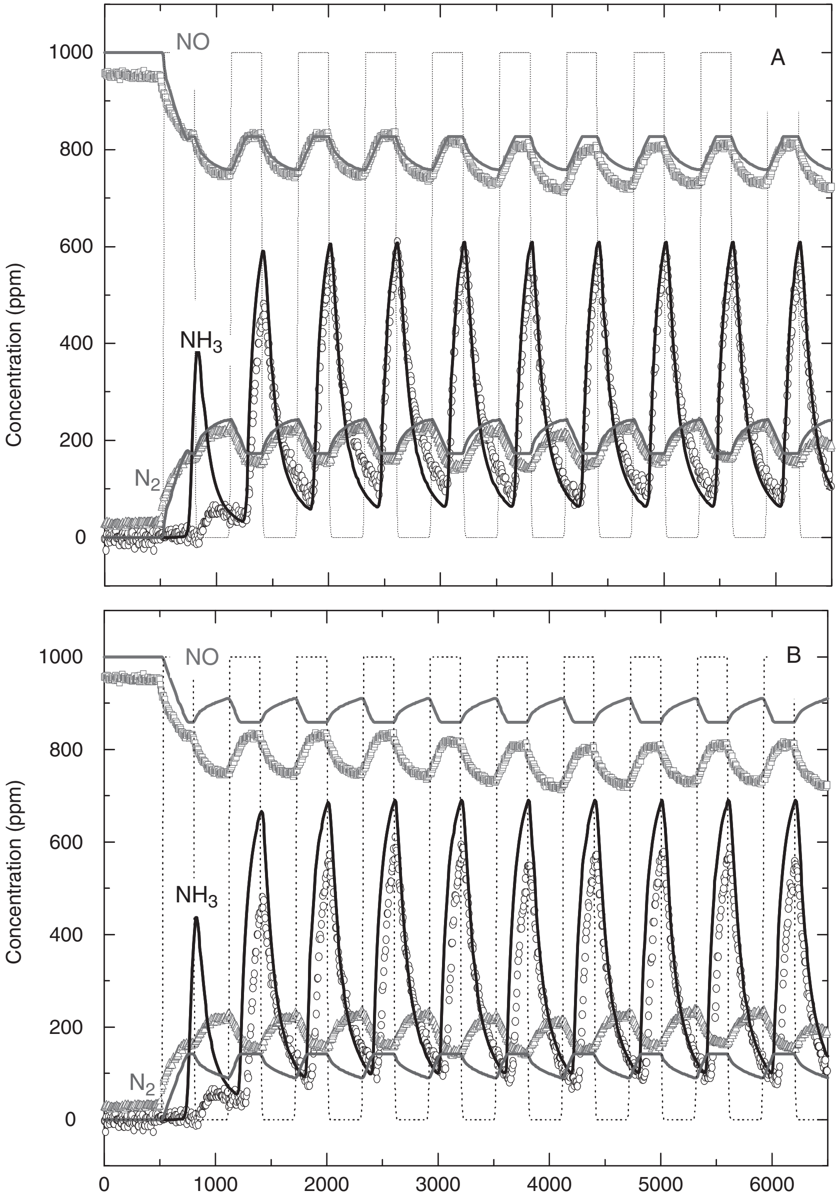

FIG. 38. Transient SCR microreactor experiments with high frequency NH_3 feed pulses (1,000 ppm) in flowing NO (1,000 ppm) + O_2 (2% v/v) and H_2O (1% v/v) + He at 180°C, with pulse frequency: 5 min on/5 min off. Symbols: outlet concentration of ammonia (circles), NO (squares) and N_2 (triangles)—Dotted lines: feed ammonia concentration. Solid lines: (A) simulation using the MR rate law, (B) simulation using the ER rate law.

real exhaust gas aftertreatment systems for vehicles. It is also worth noticing that the redox rate model, Eq. (57), predicts the existence of an optimal ammonia surface coverage at low temperatures, but reduces to the well established Eley–Rideal form at 250 °C and above, i.e. in the range of temperatures typical of SCR stationary applications. In fact, Eley–Rideal kinetics have been successfully adopted in the past for steady-state modeling of SCR installations for power plants (Forzatti *et al.*, 2002; Tronconi and Forzatti, 1992).

7. NH_3–NO–NO_2/O_2 Reacting System

The inclusion of NO_2 among the reactants of the SCR process is strictly connected with the adaptation of such a technology to mobile sources. As a matter of fact NO_x mixtures in combustion exhausts are mainly composed (95%) of NO, thus in the past years the research on SCR has been focused on the reactivity of the NH_3–NO/O_2 system. With regard to onboard applications, however, the presence of a DOC system allows the conversion of part of NO to NO_2 upstream of the SCR catalyst. Thus the amount of NO_2 in the NO_x mixture that enters the SCR catalyst is increased. This becomes an advantage for the deNO_x system as it enhances the low temperature activity, thus helping to overcome one of the biggest limitations of mobile SCR, namely the low NO_x conversions below 250°C. In fact it has been well known since the 1980s that the reaction involving an equimolar NO and NO_2 feed mixture is considerably faster than the standard SCR in the field of low temperatures.

In order to develop a suitable kinetic model of the full NH_3–NO–NO_2/O_2 SCR reacting system, first the active reactions depending on NO/NO_2 feed ratio and temperature were identified; then a dedicated study was performed aimed at clarifying the catalytic mechanism of the fast SCR reaction; on the basis of such a reaction chemistry a detailed kinetic model was eventually derived, whose intrinsic rate parameters were estimated from global non-linear regression of a large set of experimental transient runs.

8. Experimental Methods and Reaction Chemistry

The reactivity study of the NH_3–NO/NO_2 SCR system was at first focused on identifying all of the relevant reactions occurring within the range of operating conditions of industrial interest, as well as on the definition of a global reaction scheme suitable to account for the distribution of the major observed products, namely N_2, NH_4NO_3 and N_2O. Accordingly, a systematic kinetic investigation was carried out over a representative range of temperatures (160–425°C) and over the full range of NO/NO_X feed ratios (from zero to unity) (Ciardelli *et al.*, 2007a).

TRM experiments were performed with the usual procedure, i.e. feeding O_2 (2% v/v), H_2O (1% v/v) and balance He at constant temperature and performing a step change of NO_x inlet concentration ($0 \rightarrow 1{,}000$ ppm using different NO/NO_2 mixtures) while feeding 1,000 ppm of NH_3. After approaching steady state, the NH_3 feed was stepwise shut down. The system was operated at atmospheric pressure and with an SV of 210,000 h^{-1}.

Figure 39 shows, e.g., the transient data collected at 200°C and at 275°C when feeding 1,000 ppm NH_3 + 500 ppm of NO + 500 ppm of NO_2 (NO/NO_2 feed ratio = 1/1) or 1,000 ppm NH_3 + 330 ppm of NO + 670 ppm of NO_2 (NO/NO_2 feed ratio = 1/2), respectively, in terms of outlet concentrations of NO, NO_2, N_2 and NH_3 (symbols) vs. time. In the first case, conversions of roughly 700 ppm of NH_3, 350 ppm of NO, 350 ppm of NO_2, along with production of about 700 ppm of N_2 were measured at steady state. Such values agree with the stoichiometry of the fast SCR reaction. In the second example, at $t = 2{,}800$ s the NO_x mixture (330 ppm of NO + 670 ppm of NO_2) was added to the 1,000 ppm ammonia feed stream at 275°C. At this temperature all of the NO in the feed was converted, while the steady-state concentrations of the other species were about 700 ppm of N_2, 250 ppm of NH_3, 250 ppm of NO_2 and 30 ppm of N_2O. Such values are readily explained if we assume that all NO in the feed reacted according to the fast SCR stoichiometry, whereas the remaining ammonia and NO_2 reacted to give N_2 and N_2O according to the ammonium nitrate formation (R7 + R8 + R9 in Table V) and ammonium nitrate decomposition to N_2O (R11 in Table V).

The TRM experiments performed varying temperature in the range 175–275°C and the NO/NO_x feed ratio are summarized in Fig. 40 in terms of steady-state deNO_x performances (symbols) at different temperatures vs. the NO/NO_x feed ratio. It appears that in all cases, in agreement with results reported by other authors (Kato *et al.*, 1981; Koebel *et al.*, 2002), the highest NO_x conversion was achieved with a 1/1 NO_2/NO feed ratio.

Notice that at low temperature a gain of over 50% in NO_x conversion can be obtained moving from $NO/NO_x = 1$, that is with only NO in the feed, to NO/NO_x ratio = 0.5, i.e. the stoichiometric feed for the fast SCR reaction. However, for $T \geq 350°C$, in the "lean-NO_2" zone 100% of NO_x conversion could be reached because at this high temperature the standard SCR (R6 in Table V) is active enough to consume all of the excess NO, hence the promoting effect of NO_2 was not apparent. Moving toward the left part of Fig. 40, that is the "NO_2-rich" zone, the decrease in conversion is due to the low fraction of NO in the feed, which becomes the limiting reactant of the fast SCR: at low temperature the excess NO_2 then reacts with ammonia according to the ammonium nitrate formation route (R7 + R8 + R9 in Table V) while for $T > 275°C$ the NO_2–SCR, reaction R12 (cf. Table V), occurs. Both these reactions are less effective than the fast SCR (R7 + 2*R8 + R10 in Table V): reaction (R7 + R8 + R9, cf. Table V) results in a conversion of about 50% independent from the operating temperature, while reaction (R12, cf. Table V) cannot reach total NO_x conversion because ammonia becomes the limiting reactant.

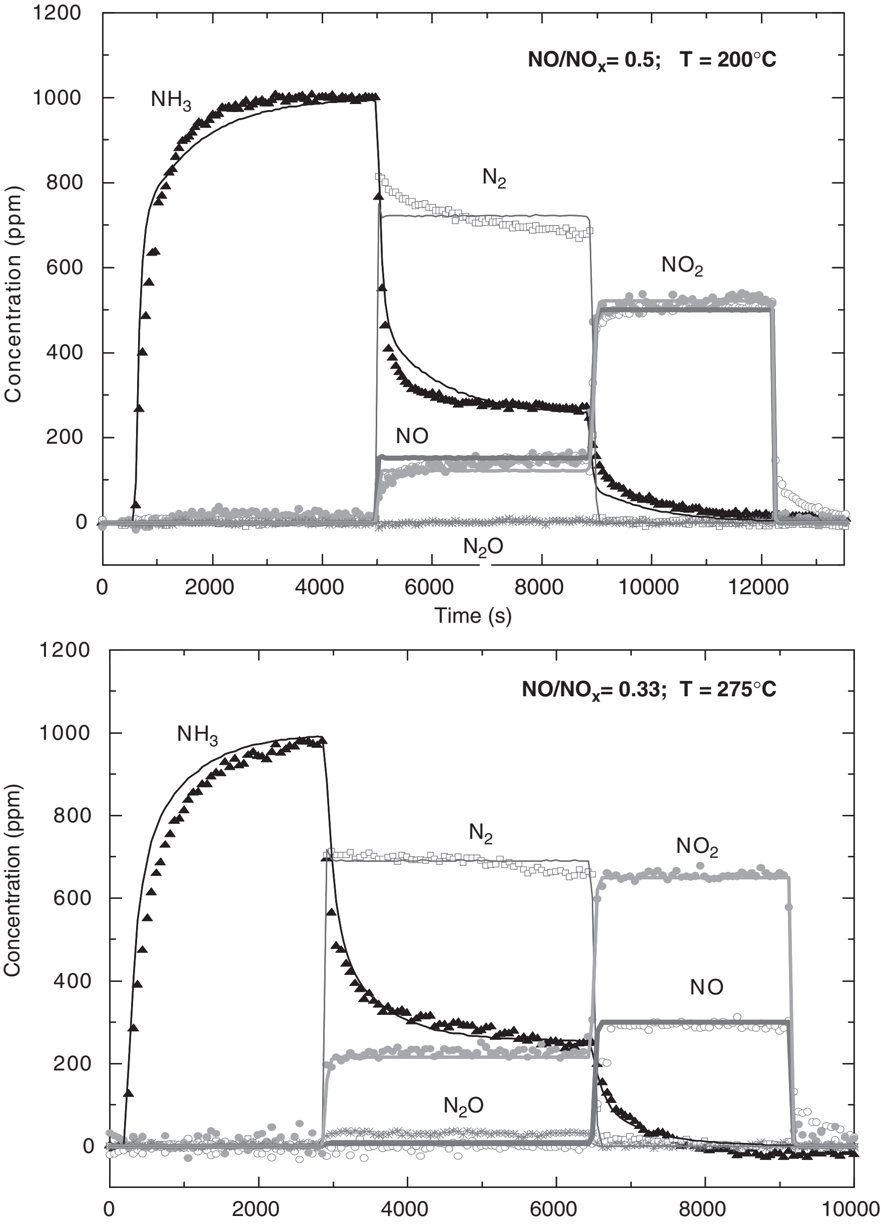

FIG. 39. $NO_x + NH_3$ TRM. Feed: 1,000 ppm NH_3, 1,000 ppm NO_x, 1% H_2O, 2% O_2, balance He, $T = 200$°C, 275°C, $SV = 210{,}000\ h^{-1}$. Symbols—outlet concentration of NH_3 (triangles), NO_2 (full circles), N_2 (squares) and N_2O (stars); solid lines—kinetic fitting.

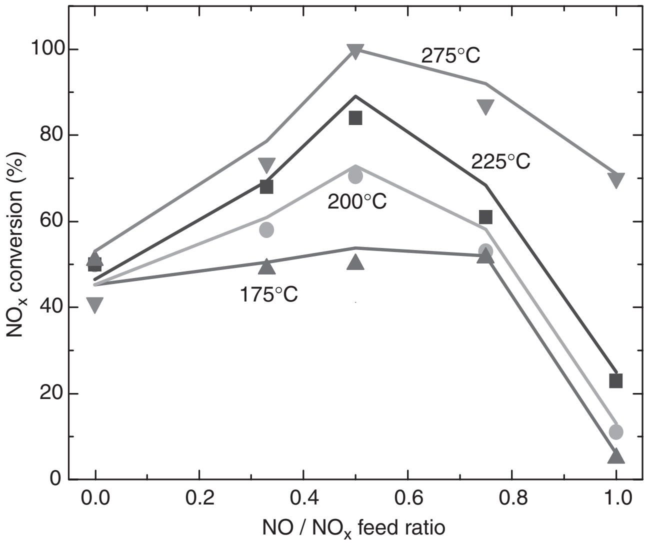

FIG. 40. Measured (symbols) and simulated (lines) steady-state SCR NO_x conversion at different T for varying inlet NO_2/NO_x ratios. Feed: 1,000 ppm NH_3, 1,000 ppm NO_x, 1% H_2O, 2% O_2, balance He, SV = 210,000 h^{-1}.

The analysis of the reactivity data herein reported provided significant insight into the chemistry prevailing over V-based SCR catalysts when feeding NH_3–NO/NO_2 mixtures, which was further extended and validated on the basis of transient response experiments addressing both the overall reactivity in the fast SCR reaction and also individual reaction steps (Ciardelli *et al.*, 2004b; Nova *et al.*, 2006b). One of the most significant findings was the identification of the key role of nitrates as intermediates in the fast SCR: this was clearly demonstrated by a set of specifically designed dynamic experiments, during which NH_4NO_3 was first formed upon the catalyst surface, and then reduced in the presence of NO. Notably, ammonium nitrate had been regarded so far only as a possible undesired by-product formed by a side reaction in parallel to the fast SCR (Madia *et al.*, 2002). One of such experiments is illustrated in Fig. 41 (Nova *et al.*, 2007).

At 150°C, when 1,000 ppm NH_3, 1,000 ppm NO, 500 ppm NO_2 (so with excess NO with respect to fast SCR stoichiometric feed) were fed to the reactor, the steady-state outlet concentrations indicated the simultaneous occurrence of the fast SCR (R7 + 2*R8 + R10 in Table V) (25% NO conversion) and of the ammonium nitrate formation (R7 + R8 + R9 in Table V) (25% NH_3 conversion): under these conditions ammonium nitrate was being partially stored onto the catalyst surface, as demonstrated in (Ciardelli *et al.*, 2004b, 2007a; Nova *et al.*, 2006b). Afterwards, at $t = 3{,}850$ s a T-ramp at 20°C/min was started: increasing consumption of NO and production of N_2 were observed, meaning

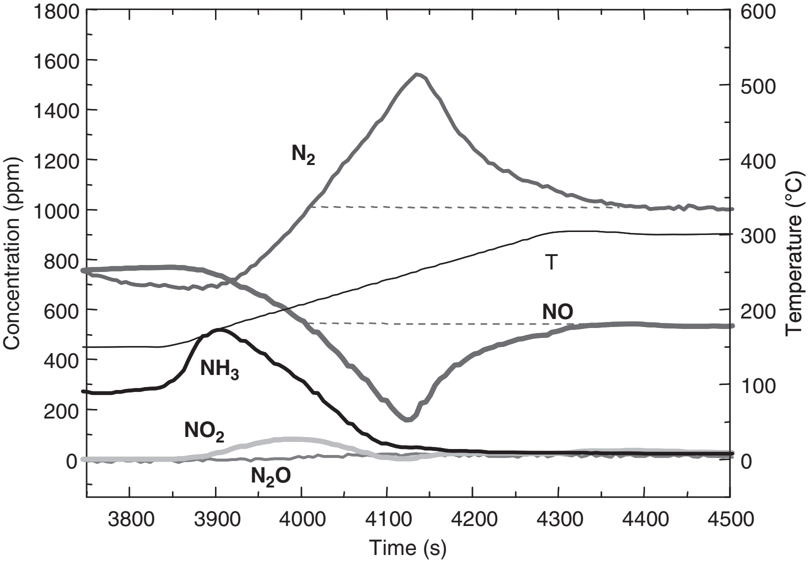

FIG. 41. TPR experiment: 1,000 ppm NH_3, 500 ppm NO_2, 1,000 ppm NO in He at $T = 150°C$; T-ramp 150–300°C at 20°C/min; SV = 92,000 h^{-1}. Reprinted from Nova *et al.* (2007) with kind permission of Springer Science and Business Media.

that the rate of the fast SCR reaction was growing. As the T-ramp started, desorption of NH_3 was also observed, as well as a small production of NO_2. Both such species were then consumed as the temperature was increased further.

The analysis of the transient behavior during the temperature ramp points out that another reaction involving NO consumption must have been occurring in addition to the fast SCR: with a feed mixture of 1,000 ppm NH_3, 1,000 ppm NO and 500 ppm NO_2, the highest possible conversion of NO according to the fast SCR reaction should have been 50%, with a production of 1,000 ppm of N_2 (the dashed lines in Fig. 41 indicate such values). Nevertheless, the measured NO conversion exceeded 50%, reaching a peak of about 80% with a simultaneous production of 1,600 ppm of N_2. Such a behavior is explained by invoking the reaction between ammonium nitrate (which had been previously formed and stored onto the catalyst surface, as mentioned above) and NO, according to the stoichiometry resulting from the combination of R9 reverse and R10 ($-R9 + R10$ in Table V).

The depletion of NH_4NO_3 is responsible for the subsequent drop of NO conversion observed after $t = 4{,}150$ s, and indeed at the end of the experiment steady-state concentrations of reactants and products were eventually in agreement with the occurrence of the fast SCR reaction only. It appears thus that the fast SCR reaction was proceeding only before $t = 4{,}000$ s while, as it became limited by the NO_2 feed concentration, the reaction ($-R9 + R10$, cf. Table V) occurred afterwards. However, no discontinuity and no change of slope can be observed in the neighborhood of $t = 4{,}000\,\mathrm{s}$, thus indicating that the fast SCR reaction and the reaction between NO and NH_4NO_3 share the same rate as well as the same apparent activation energy.

The same conclusion was also achieved performing a transient experiment at constant temperature (170°C) (Ciardelli *et al.*, 2004b; Nova *et al.*, 2006b): the NO conversion levels measured either when the fast SCR reaction was occurring or when the reaction between NO and surface nitrates was occurring were practically unaltered, indicating that the two reactions were actually progressing at the same rate.

Accordingly, it can be ruled out that the reaction between NH_4NO_3 and NO and the fast SCR reaction proceed in parallel: we have proposed an alternative, sequential scheme, whereby the fast SCR reaction results from the formation of nitrate surface species related to NH_4NO_3, reactions (R7 + R8 + R9, Table V), and their subsequent reduction by NO, reaction (R10 in Table V), which is rate determining at low temperature (Ciardelli *et al.*, 2004b).

Thus, the overall reaction scheme of the fast SCR is depicted in Fig. 42, and the roles of the reactants in such scheme can be summarized as follows (Ciardelli *et al.*, 2007a; Nova *et al.*, 2006b):

(i) NO_2 is responsible for the formation of nitrate and nitrite adspecies, likely via disproportion and heterolytic chemisorption (R7 in Table V).
(ii) NO acts as a reductant, converting nitrates to nitrites (R10 in Table V).
(iii) NH_3 eventually reacts with nitrites to give harmless nitrogen and H_2O via decomposition of the unstable ammonium nitrite (R8 in Table V).
(iv) In defect of NO, NH_3 can also react with nitrates to form ammonium nitrate, which, under specific low-T conditions ($T < 170°C$), builds up onto the catalysts (cf. R9, Table V).

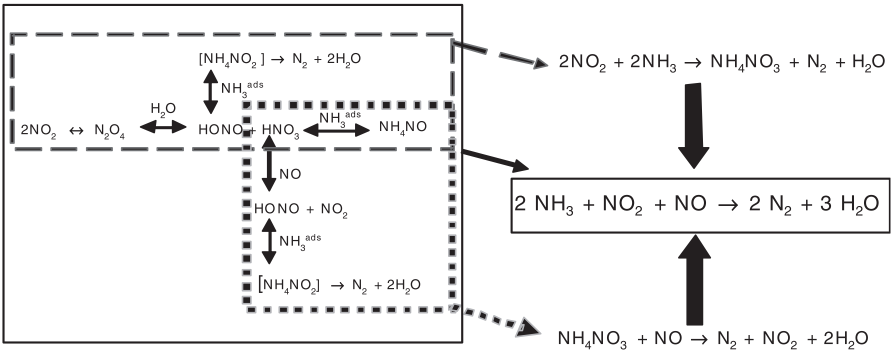

FIG. 42. Chemistry of NH_3–NO_2 (upper dashed box) and NH_3–NO/NO_2 (solid box) SCR reacting systems over V_2O_5–WO_3/TiO_2 SCR catalysts.

A similar reaction scheme has been recently proposed on the basis of an IR study of the NO/NO_2–NH_3 reactivity over a BaNa–Y zeolite SCR catalyst (Yeom *et al.*, 2005).

It is worth emphasizing that the reaction scheme above is able to explain not only the stoichiometry of the fast SCR reaction, and specifically the optimal equimolar NO to NO_2 feed ratio, but also the selectivity to all of the observed products, namely N_2, NH_4NO_3 and N_2O, which derives from thermal decomposition of ammonium nitrate (Ciardelli *et al.*, 2004b, 2007a; Nova *et al.*, 2006b); furthermore it is in agreement with the observed kinetics of the fast SCR reactions, which at low temperature is limited by the rate of the reaction between nitrate and NO.

In additional dedicated mechanistic experiments we found that, contrary to the NH_4NO_3 formation, the rate limiting step (i.e. reaction R10 in Table V) as well as the global fast SCR reaction did not proceed over a V-free WO_3/TiO_2 catalyst, thus identifying the catalytic role of vanadium redox sites in the fast SCR mechanism (Tronconi *et al.*, 2007). It was also proved that surface nitrate species, formed from NO_2, are much more effective than gaseous oxygen in reoxidizing the reduced V-sites, which explains the greatly enhanced deNO$_x$ activity with respect to the standard SCR at low temperature. Accordingly, a unifying mechanistic redox scheme could be proposed for both standard and fast SCR reactions, i.e. for the global NH_3–NO/NO_2 SCR process (Tronconi *et al.*, 2007).

Reactions R13, Table VI and R14, Table VI describe the redox cycle in the NO + NH_3 standard SCR, where reaction (R14, Table VI) is the rate limiting reoxidation step involving gaseous oxygen.

In the case of the NO + NO_2 + NH_3 fast SCR, the reduction of the V-catalyst sites still occurs according to the same global reaction (R13, Table VI), but the rate determining step in the redox process, i.e. the reoxidation of V-sites, is radically changed, being carried out in this case by nitrates according to reaction (R15, Table VI). Nitrates are formed together with nitrites through reaction (R16, Table VI) via disproportion of NO_2, while reaction (R17, Table VI) accounts for the decomposition of nitrites to N_2 via reaction with NH_3.

In agreement with experimental observations (Tronconi *et al.*, 2007), notice that no redox catalyst function is involved in steps (R16, Table VI)

TABLE VI

UNIFYING MECHANISTIC REDOX SCHEME FOR STANDARD AND FAST SCR REACTIONS

Standard SCR	
$NO + NH_3{}^* + V^{5+}{=}O \rightarrow N_2 + H_2O + V^{4+}{-}OH$	R13
$V^{4+}{-}OH + \frac{1}{4}O_2 \rightarrow V^{5+}{=}O + \frac{1}{2}H_2O$	R14
Fast SCR	
$NO + NH_3{}^* + V^{5+}{=}O \rightarrow N_2 + H_2O + V^{4+}{-}OH$	R13
$V^{4+}{-}OH + NO_3^- + H^+ \rightarrow V^{5+}{=}O + NO_2 + H_2O$	R15
$2NO_2 + O^{2-} \leftrightarrow NO_2^- + NO_3^-$	R16
$NO_2^- + NH_3 \rightarrow N_2 + H_2O + O^{2-} + H^+$	R17

and (R17, Table VI), which are assumed to occur over non-reducible oxidic sites (herein represented schematically as O^{2-}) possibly associated with the W- or Ti-catalyst components. A similar sequence has been recently invoked to explain the formation of ammonium nitrate observed over TiO_2 and over zeolites (Yeom *et al.*, 2005), as well as the formation of nitrates from NO_2 over Al_2O_3 (Apostolescu *et al.*, 2004).

Notably, the kinetic scheme herein presented is in complete agreement with the findings on the role of nitrates in the chemistry of the fast SCR reaction presented before.

9. *Kinetic Analysis*

For a comprehensive kinetic description of the NH_3+NO/NO_2 reacting system in a wide range of temperatures and NO_2/NO_x feed ratios a global kinetic model was developed, based on the whole set of reactions in Table V.

The extension of the present model to include the redox features presented in the previous section is currently ongoing.

The ammonia, NO and nitrogen mass balance equations were modified with respect to those already presented in previous sections, in order to include all of the reactions observed in the NH_3–NO/NO_2 reacting system. Moreover, additional mass balances for adsorbed nitrates (θ_{HNO_3}) and for gaseous NO_2, N_2O and HNO_3 were introduced

(a) adsorbed phase:

$$NH_3^* \quad \Omega\frac{\partial\theta_{NH_3}}{\partial t} = R_{ads} - R_{des} - R_{ox} - R_{NO} - R_{NO_2} - R_{nit} - R_{dec} - R_{N_2O} \quad (59)$$

$$NH_4NO_3^* \quad \Omega\frac{\partial\theta_{NH_4NO_3}}{\partial t} = R_{dec} \quad (60)$$

(b) gas phase:

$$NH_3 \quad \varepsilon^g\frac{\partial c_{NH_3}}{\partial t} = -u\frac{\partial c_{NH_3}}{\partial z} - (1-\varepsilon^g)(R_{ads} - R_{des}) \quad (61)$$

$$N_2 \quad \varepsilon^g\frac{\partial c_{N_2}}{\partial t} = -u\frac{\partial c_{N_2}}{\partial z} + (1-\varepsilon^g)\left(\frac{1}{2}R_{ox} + R_{NO} + R_{nit} + \frac{7}{8}R_{NO_2}\right) \quad (62)$$

$$NO \quad \varepsilon^g\frac{\partial c_{NO}}{\partial t} = -u\frac{\partial c_{NO}}{\partial z} - (1-\varepsilon^g)(R_{NO} + R_{FST}) \quad (63)$$

$$NO_2 \quad \varepsilon^g\frac{\partial c_{NO_2}}{\partial t} = -u\frac{\partial c_{NO_2}}{\partial z} - (1-\varepsilon^g)\left(2R_{amm} - R_{FST} + \frac{3}{4}R_{NO_2}\right) \quad (64)$$

$$\mathrm{N_2O} \quad \varepsilon^{g}\frac{\partial c_{\mathrm{N_2O}}}{\partial t} = -u\frac{\partial c_{\mathrm{N_2O}}}{\partial z} + (1-\varepsilon^{g})R_{\mathrm{N_2O}} \tag{65}$$

$$\mathrm{HNO_3} \quad \varepsilon^{g}\frac{\partial c_{\mathrm{HNO_3}}}{\partial t} = -u\frac{\partial c_{\mathrm{HNO_3}}}{\partial z} + (1-\varepsilon^{g})(R_{\mathrm{amm}} - R_{\mathrm{FST}} - R_{\mathrm{N_2O}} - R_{\mathrm{dec}}) \tag{66}$$

A pseudo-steady-state assumption was introduced for HONO, in view of its ready decomposition to N_2

$$\mathrm{HONO} \quad 0 = (R_{\mathrm{amm}} - R_{\mathrm{nit}} + R_{\mathrm{FST}}) \tag{67}$$

Consistently with what reported in the previous sections the NH_3 adsorption, desorption and oxidation rates were fitted by the following expressions, respectively:

$$R_{\mathrm{ads}} = k_{\mathrm{ads}}c_{\mathrm{NH_3}}(1-\theta_{\mathrm{NH_3}}-\theta_{\mathrm{NH_4NO_3}}) \tag{68}$$

$$R_{\mathrm{des}} = k_{0,\mathrm{des}}\exp\left[-\frac{E_{\mathrm{des}}}{RT}(1-\alpha\theta_{\mathrm{NH_3}})\right]\theta_{\mathrm{NH_3}} \tag{48}$$

$$R_{\mathrm{ox}} = k_{0,\mathrm{ox}}\exp\left(-\frac{E_{\mathrm{ox}}}{RT}\right)\left(\frac{y_{\mathrm{O_2}}}{0.02}\right)^{\beta}\theta_{\mathrm{NH_3}} \tag{52}$$

For the standard SCR reaction, the following rate expression was considered,

$$R_{\mathrm{NO}} = k_{0,\mathrm{NO}}\exp\left(-\frac{E_{\mathrm{NO}}}{RT}\right)\gamma_{\mathrm{NO}}c_{\mathrm{NO}}\theta_{\mathrm{NH_3}}\left(\frac{y_{\mathrm{O_2}}}{0.02}\right)^{\beta}$$

$$\gamma_{\mathrm{NO}} = \frac{1}{1+K_{\mathrm{LH}}(\theta_{\mathrm{NH_3}}/(1-\theta_{\mathrm{NH_3}}-\theta_{\mathrm{NH_4NO_3}}))} \tag{69}$$

which represents a simplified form of the MR dual-site redox rate expression, Eq. (57). The following expressions were adopted for the rates of reactions (R7–12, Table V)

$$R_{\mathrm{amm}} = k_{0,\mathrm{amm}}\exp\left(-\frac{E_{\mathrm{amm}}}{RT}\right)\left(y_{\mathrm{H_2O}}c^{2}_{\mathrm{NO_2}} - \frac{c_{\mathrm{HNO_3}}c_{\mathrm{HNO_2}}}{K^{\mathrm{eq}}_{\mathrm{amm}}}\right) \tag{70}$$

$$R_{\mathrm{nit}} = k_{0,\mathrm{nit}}\exp\left(-\frac{E_{\mathrm{nit}}}{RT}\right)\theta_{\mathrm{NH_3}}c_{\mathrm{HNO_2}} \tag{71}$$

$$R_{\mathrm{dec}} = k_{\mathrm{adsnit}}\theta_{\mathrm{NH_3}}c_{\mathrm{HNO_3}} - k_{0,\mathrm{dec}}\exp\left(-\frac{E_{\mathrm{dec}}}{RT}\right)\theta_{\mathrm{NH_4NO_3}} \tag{72}$$

$$R_{\mathrm{FST}} = k_{0,\mathrm{FST}} \exp\left(-\frac{E_{\mathrm{FST}}}{RT}\right)\gamma_{\mathrm{FST}}\left(c_{\mathrm{NO}}c_{\mathrm{HNO_3}} - \frac{c_{\mathrm{NO_2}}c_{\mathrm{HNO_2}}}{K^{\mathrm{eq}}_{\mathrm{FST}}}\right)$$

$$\gamma_{\mathrm{FST}} = \frac{1}{1 + K_{\mathrm{LH_2}}(\theta_{\mathrm{NH_3}}/(1 - \theta_{\mathrm{NH_3}} - \theta_{\mathrm{NH_4NO_3}}))} \tag{73}$$

$$R_{\mathrm{N_2O}} = k_{0,\mathrm{N_2O}} \exp\left(-\frac{E_{\mathrm{N_2O}}}{RT}\right)\theta_{\mathrm{NH_3}}c_{\mathrm{HNO_3}} \tag{74}$$

$$R_{\mathrm{NO_2}} = k_{0,\mathrm{NO_2}} \exp\left(-\frac{E_{\mathrm{NO_2S}}}{RT}\right)\theta_{\mathrm{NH_3}}c_{\mathrm{NO_2}} \tag{75}$$

For Eqs. (48), (52) and (68)–(69), the same rate parameter values were herein adopted as used in the previous work addressing the standard SCR reaction only (Chatterjee *et al.*, 2005; Ciardelli *et al.*, 2004a). A set of 32 experimental runs was used for the estimation of the additional rate parameters for the reactions involving NO_2 according to the procedures described in (Chatterjee *et al.*, 2005, 2006; Ciardelli *et al.*, 2004a).

With respect to the large number of fitting parameters required to account for the comprehensive reaction scheme, and in order to minimize correlations, a sequential fitting strategy was followed (Chatterjee *et al.*, 2006). First, the rate parameters associated with formation, adsorption–desorption of ammonium nitrate, in Eqs. (70)–(72), were estimated by regressions of results from runs with feeds containing $NO_2 + NH_3$ only. In a subsequent stage, the estimates of the rate parameters in Eq. (73) were secured by regression on runs involving $NO + NO_2 + NH_3$ at temperatures below 250°C, where the NO_2 SCR reaction is not active. Finally, the rate parameters for Eqs. (74) and (75), i.e. for the NO_2 SCR and the formation of N_2O, were estimated from the high-temperature TRM runs. As an example, the quality of the fit is illustrated in Fig. 39, where the calculated (lines) and measured (symbols) temporal evolutions of NH_3, NO, NO_2, N_2 and N_2O are reported. A good correlation is indeed obtained between experimental traces and model predictions, thus supporting the adequacy of the kinetic model. Most important for the practical applications herein discussed, Fig. 40 confirm that the proposed rate equations are able to represent effectively the observed influence of the NO_2 feed content on the whole T-range.

A first validation was obtained simulating the results collected at different ammonia to NO_x feed ratios: as an example, in Fig. 43 some of the experimental results (symbols) are compared with the model predictions (line).

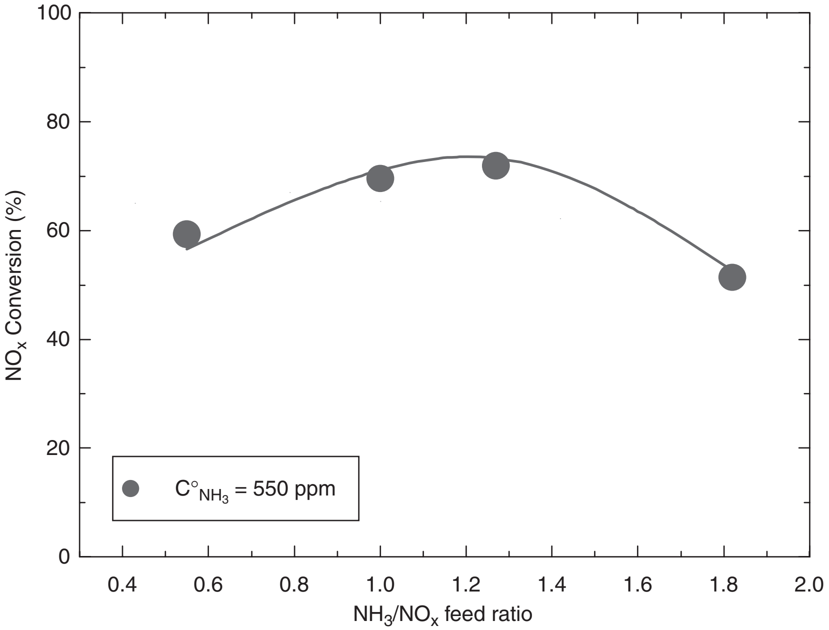

FIG. 43. Steady-state NO conversions vs. NH_3/NO_x feed ratio. SV = 210,000 h^{-1}; $T = 200\,°C$; $C_{O_2} = 2\%$; $C_{H_2O} = 1\%$; $NO/NO_x = 0.5$. Symbols: experimental, solid line: model predictions.

B. MONOLITH REACTOR SCALE

Validation at intermediate scale was first performed by comparing the results of kinetic runs over small honeycomb catalyst samples (volumes in the range 5–20 cm^3) with corresponding model simulations. For these purposes the intrinsic kinetics derived above were incorporated into a fully transient two-phase adiabatic 2D (1D + 1D) mathematical model of SCR monolith reactors (Chatterjee *et al.*, 2005, 2006; Tronconi *et al.*, 1998) specifically adapted for mobile SCR applications, similar to the one described in Section III. Such a model accounts also for intraporous diffusion of reacting and product species within the porous catalytic walls of the honeycomb matrix. Effective intraporous diffusivities were estimated according to Wakao and Smith (1962) on the basis of the experimentally determined morphological characteristics of the catalyst. Additional assumptions include negligible pressure drop and axial dispersion.

1. *Experimental*

Kinetic runs over small monolithic honeycomb catalyst samples were performed in two different rigs at Politecnico di Milano and in the Daimler

AG laboratories in Stuttgart. The experiments were carried out using monolith samples (order of magnitude of honeycomb volumes: 10–20 cm^3) of 200 or 300 cpsi cell density made of the same catalyst material used for the microreactor runs. Runs were carried out under isothermal conditions within the T-range 150–450°C. The space velocity was set between 36,000 and 72,000 h^{-1} by changing the flow rate and the monolith length (22 or 44 mm). The synthetic feed mixture was composed by oxygen (2–10% v/v), water (1–10% v/v), NO (1,000 ppm), NH_3 (800–1,200 ppm) and balance nitrogen. Specific gas analyzers were used to follow the transient behavior of the reactants: in Stuttgart NH_3 was detected by microwave process analysis (Mipan), while NO_x by chemiluminescence techniques using a modified low temperature NO_2 converter (CLD Ecophysics). In Milano a second UV analyzer (ABB Limas 11) was adopted for NO, NO_2 and NH_3, similar to the one installed in the microreactor rig.

Figure 44 illustrates the results of steady-state experiments at different temperatures over a small honeycomb sample (volume ≈ 20 cm^3, 300 cpsi) with a feed flow rate of 9,800 cm^3/min, with composition 1,000 ppm NO, 1,000 ppm

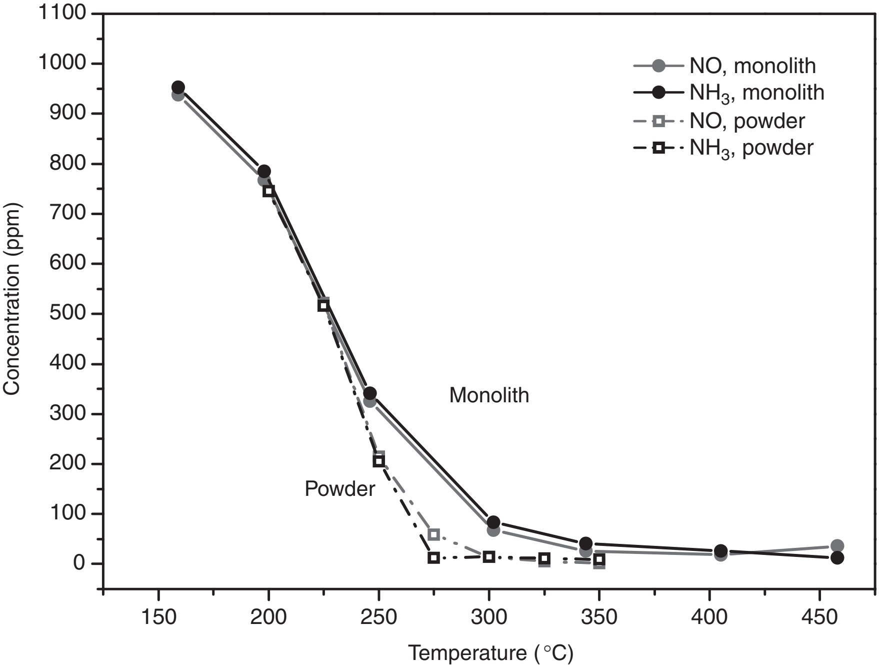

FIG. 44. Steady-state NO and NH_3 concentrations vs. temperature in runs over a small monolith catalyst with 300 cpsi and over the same catalyst crushed to powder. Feed: 1,000 ppm NH_3, 1,000 ppm NO, 1% H_2O, 2% O_2 in N_2; SV = 45,000 cm^3/g/h (STP).

NH_3, 2% O_2, 1% H_2O and balance nitrogen. The solid symbols indicate measured outlet NO and NH_3 concentrations. For comparison purposes, the figure shows also the outlet concentrations measured during identical experiments over the catalyst powder obtained by crushing and sieving the same monolith (open symbols). In this case the flow rate was adjusted to achieve the same space velocity (45,000 $cm^3/g/h^{-1}$) with reference to the active catalyst mass. It is apparent that the data over the monolith and over the powder catalyst are overlapped in the low-T region. At $T >$ 225 °C, however, deviations become apparent, corresponding to lower conversions over the monolith catalyst. Such deviations are attributed to the onset of diffusion limitations in the honeycomb catalyst, which therefore play a significant role in controlling the deNO$_x$ performance over a wide range of temperatures.

As shown in Fig. 45, two series of experiments were performed with different O_2 feed contents: higher NO conversions were observed when 10% O_2 was fed (squares), thus confirming at the monolith scale the promoting effect of oxygen on the standard SCR reaction (R6, Table V) noted in microreactor experiments over the powdered catalysts and discussed in previous sections. Solid lines in Fig. 45 represent the results of model simulation: a very good agreement between experimental and calculated NO$_x$ conversions is observed. The promoting effect of oxygen was also very well predicted.

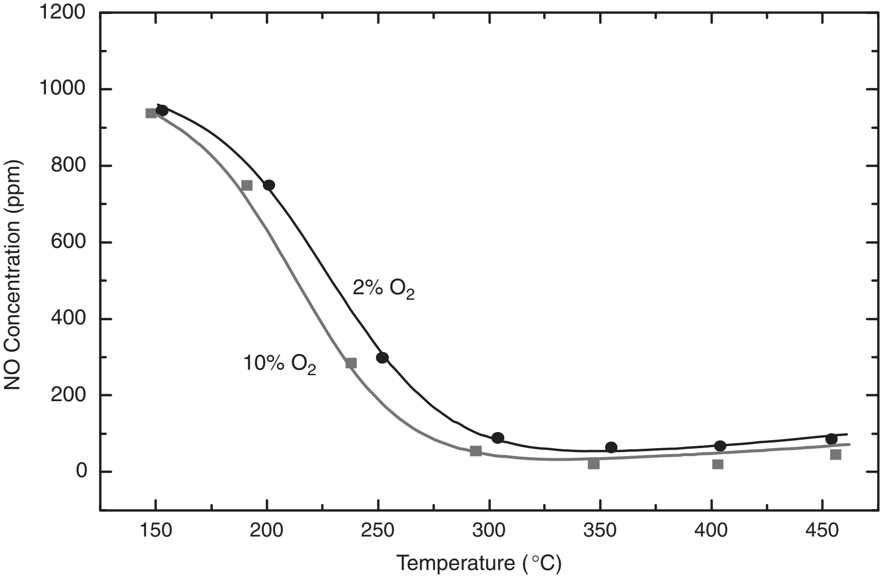

FIG. 45. Steady-state NO concentrations vs. temperature in validation runs over small monolith catalyst sample with 300 cpsi. Feed: 1,000 ppm NH_3, 1,000 ppm NO, 1% H_2O in N_2; black: 2% O_2, red: 10% O_2; SV = 25,000 h^{-1}; symbols: experimental, solid line: model predictions.

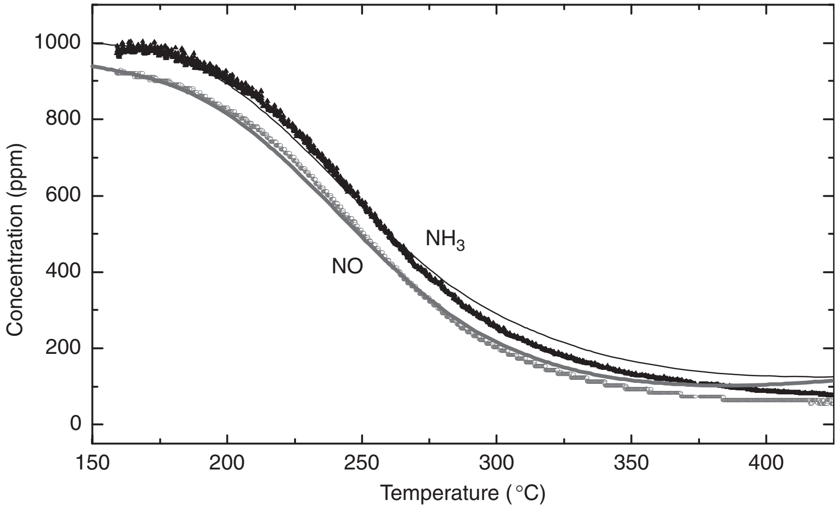

FIG. 46. TPR validation run over small monolith catalyst with 200 cpsi. Feed: 1,020 ppm NH_3, 960 ppm NO, 10% H_2O, 10% O_2 in N_2, SV = 36,000 h^{-1}; symbols: experimental, solid line: model predictions.

Figure 46 presents the comparison between experimental results (symbols), obtained over a different monolith sample (volume $\approx$ 10 cm^3) upon performing a TPR run, and the corresponding model predictions (solid lines): 1,020 ppm of NH_3 and 960 ppm of NO were fed in a stream of 10% H_2O, 10% O_2, balance nitrogen, with an SV = 36,000 h^{-1}.

A temperature ramp (from 100°C to 450°C) was performed. Equimolar conversion of NO and NH_3 was observed, in agreement with the stoichiometry of the standard SCR reaction (R6, Table V). The observed reactivity was again well predicted by the model simulation in the whole T-range.

A third transient experiment is shown in Fig. 47, where again experimental results (symbols) are compared with model simulation (solid lines). At time = 0 s, 1,000 ppm of NH_3 and 1,000 ppm of NO were simultaneously fed to the honeycomb catalyst (5 cm^3) in a stream of 10% H_2O, 10% O_2, balance nitrogen, with an SV = 72,000 h^{-1}. Temperature was set at 250 °C.

After the initial transient, NO and ammonia signals pointed to a steady-state conversion of about 40%. Again the standard SCR stoichiometry was respected. At time of about 300 s, the NH_3 feed was shutoff. Consequently its outlet signal slowly decreased, while NO, after a short transient, reached its feed value of 1,000 ppm. Again, a good correlation between experiment and predictive simulation on the integral monolith reactor level was obtained: the model was able to correctly predict both the steady-state levels of the reactants and their temporal evolution.

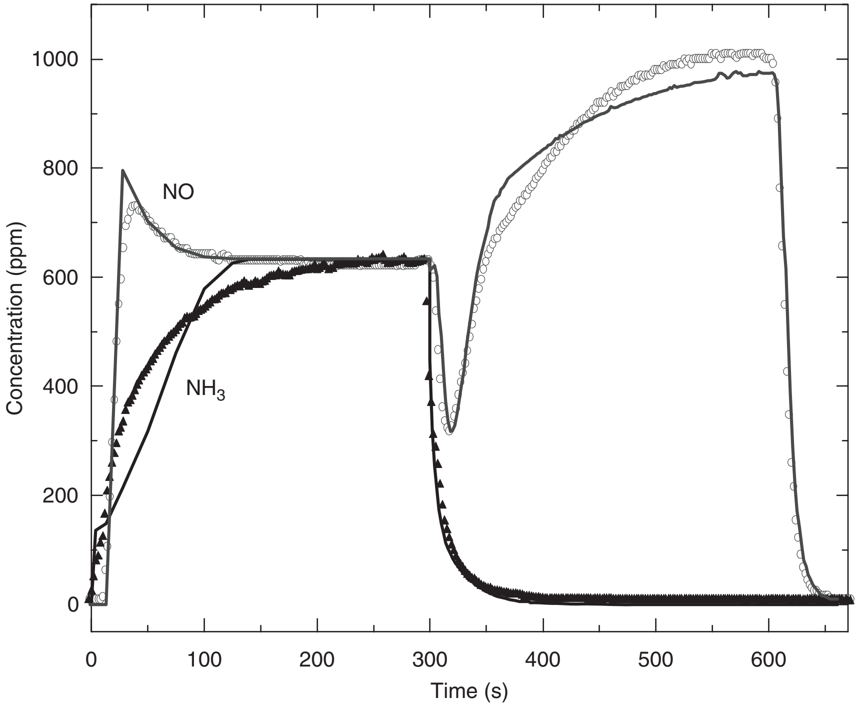

FIG. 47. TRM validation run over a small monolith catalyst with 200 cpsi. Feed: 1,000 ppm NH_3, 1,000 ppm NO, 10% H_2O, 10% O_2 in N_2, $T = 250°C$, $SV = 72{,}000\ h^{-1}$; symbols: experimental, solid line: model fitting.

Altogether, the data reported in this section indicate a very good predictive quality of the model simulations: this implies in the first place that the SCR kinetics estimated over powdered catalyst were successfully validated at this bigger scale. However, the excellent agreement between monolith data and model predictions based on intrinsic kinetics also confirms the accurate model description of physical phenomena, specifically external and intraporous mass transfer, which were not significant in the microreactor runs over the powdered catalyst, but played an important role in the monolith runs, as pointed out by the direct comparison in Fig. 44.

C. ENGINE TEST BENCH SCALE

1. *Heavy-duty Diesel Engine Runs, No DOC*

Different sets of experimental data were used for model validation at real gas scale. Urea was used to supply NH_3: an adequate residence time in the exhaust gas stream was allowed to secure its complete conversion to NH_3 before reaching the SCR catalyst.

A first data set was measured on a heavy-duty diesel engine test bench. Extruded monoliths with 300 cpsi, a wall thickness of 0.32 mm and a diameter of 144 mm were used in these runs. By varying the number of monolith catalyst samples it was possible to test different catalyst volumes (25, 32 and 43 L). The complete SCR catalyst setup resulted in SVs ranging from 21,000 to 40,000 h^{-1}.

In these experiments no oxidation catalyst was positioned upstream of the SCR catalysts; accordingly the NO_2 concentration was always negligible ($\leq 5\%$ v/v of the total NO_X feed content). A set of 100 different engine-operating points was measured and a sampling time of 2 Hz before and after the catalyst system was adopted to measure both temperatures and emissions using a chemiluminescence spectrometer for NO and NO_2 and a diode laser spectrometer for NH_3. A typical test bench experiment started when the engine ran at constant load and speed. After a given time the urea dosing system introduced the reducing agent onto the catalyst, which resulted in an increase of the NO_x conversion after the SCR-catalyst. After that the NH_3 slip behind the catalyst could be measured. Typically, the experiment ran until total NO_x conversion or steady state was established. Validation maps, as illustrated, e.g., in Fig. 48, were generated using the steady state measured engine operating points. In this case the deviation between simulated NO_x conversion and experimental data was typically below 4% (Chatterjee *et al.*, 2005).

Standard European test cycles (ESC and ETC), during which the catalyst outlet temperature varied between 200°C and 350°C, were also performed at this scale. Examples of related simulation results are plotted together with data taken from the transient heavy-duty engine test bench runs in Fig. 48, where NO_x concentrations have been normalized by the maximum inlet value during the test cycles. The comparison between measurement and simulation for the NO_x concentrations downstream of the catalyst reveals an excellent correlation, as pointed out by Fig. 49A (ESC) and B (first 500s of ETC). The overall deNO_x efficiency within the ESC or ETC test cycle is predicted with an error of 3–4% (Chatterjee *et al.*, 2005; Tronconi *et al.*, 2005). Notably, the overall satisfactory agreement of the predictive simulations with data from test runs with real engine exhausts also confirms the negligible influence of such species as CO, CO_2 and hydrocarbons, whose effects were not included in the kinetic investigation.

2. *Heavy-duty Diesel Engine Runs, with DOC*

In a second set of experiments, DOC was placed upstream of the SCR catalyst in order to generate NO_2 by partial oxidation of NO in the engine

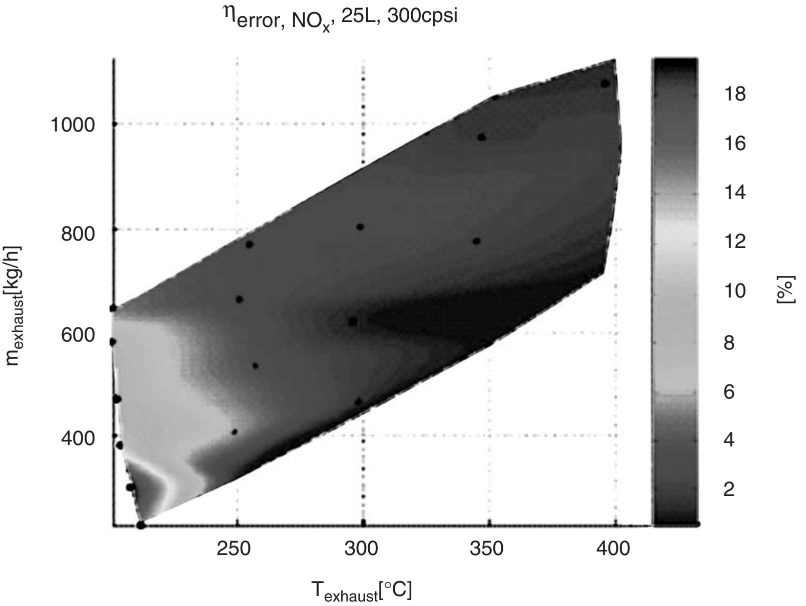

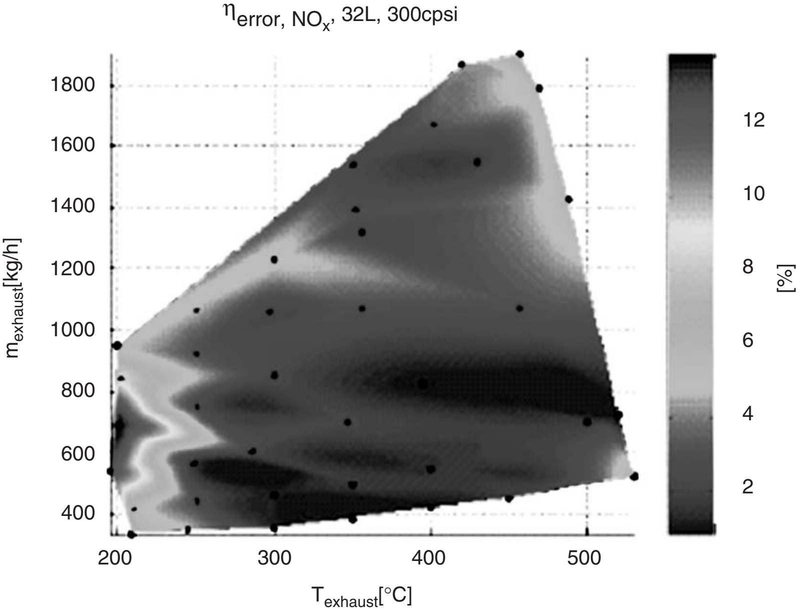

FIG. 48. Mean error for the simulation of the NO_x conversion at steady-state and constant urea dosing conditions as a function of exhausts mass flow and catalyst inlet temperature. Reprinted with permission from SAE Paper # 2005-01-0965 © 2005 *SAE International* (see Plate 6 in Color Plate Section at the end of this book).

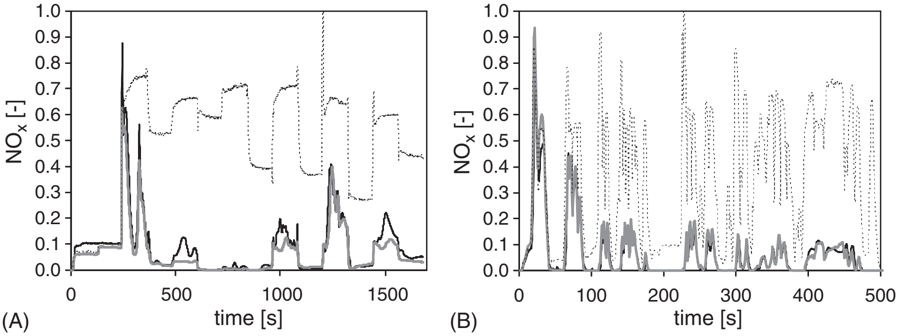

FIG. 49. Normalized NOx concentration at SCR catalyst inlet and outlet of an ESC (A) and an ETC (B) test cycle. Dotted black lines—inlet values, solid black lines—outlet measurement, gray lines—outlet simulation. Reprinted with permission from SAE Paper # 2006-01-0468 © 2006 *SAE International.*

exhausts. Twelve HD engine operating points were measured, covering exhaust temperatures at SCR converter inlet from 200°C to 470°C and NO_2/NO_x feed contents from 3% to 40%.

As shown, e.g., in Fig. 50, a good correlation between simulation and experiment was apparent in all cases, which confirms the good prediction quality of the SCR converter model also in the presence of NO_2. It should be noted that the NO_x conversion curves of these experiments (see e.g. Fig. 50) reveal a typical behavior. After the start of the urea dosage a steep increase in the NO_x conversion rate appears, which is mainly determined by the fast SCR reaction converting all of the available NO_2. In the following time period, the increase of the NO_x conversion is much slower, with the limiting factor being the buildup of stored NH_3.

3. Passenger Car Diesel Engine Runs, with DOC

Finally, a passenger car diesel engine was used in a third set of test bench experiments to test the model under more dynamic conditions. Because of restrictions on the residence time between DOC and SCR catalyst and due to the higher dynamics of the experiments, complete conversion of urea could not be assured in this case, therefore gaseous NH_3 instead of urea was injected after the oxidation catalyst. The SCR catalyst used for these experiments was an extruded monolith with 300 cpsi, a wall thickness of 0.32 mm in a race track shape. The studied SVs ranged from 70,000 to 211,000 h^{-1}, the measured 14 engine operating points covering exhaust temperatures from 230°C to 460°C and NO_2/NO_x ratios from 10% to 44%. In addition to the measurement setup used for the heavy-duty test bench, a mass spectrometer (CIMS) was used for NO, NO_2 and NH_3 (Chatterjee *et al.*, 2006).

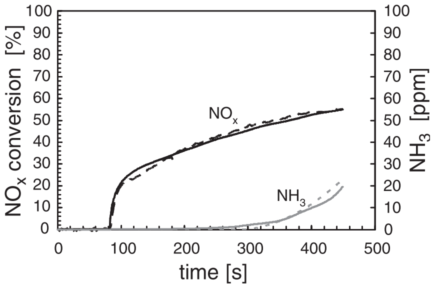

17a) Texh. = 200 °C, NO_2/NO_x = 3%, GHSV = 21500h^{-1} and $\alpha = 1.24$

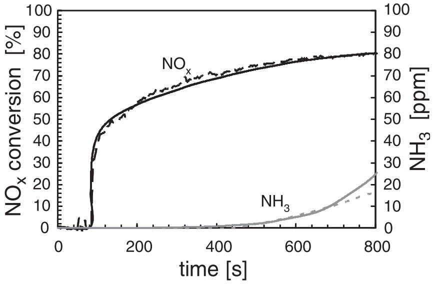

17b) Texh. = 220°C, NO_2/NO_x = 16%, GHSV = 21700h^{-1} and $\alpha = 1.29$

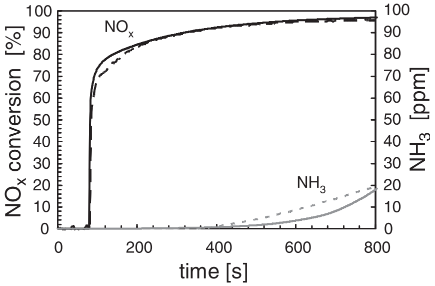

17c) Texh. = 250 °C, NO_2/NO_x = 31%, GHSV = 22400h^{-1} and $\alpha = 1.25$

FIG. 50. Heavy-duty engine test bench measurements. Dotted lines—measurement of NO_x conversion (black) and NH_3 slip (gray); solid lines—simulation of NO_x conversion (black) and NH_3 slip (gray). Reprinted with permission from SAE Paper # 2006-01-0468 © 2006 *SAE International.*

Because of the short NH_3 pulses, no steady state within the SCR catalyst was reached during the experimental runs. Yet, the example presented in Fig. 51 reveals once more a good agreement between simulation and experiment, even under conditions with very short NH_3 pulses. The deviations

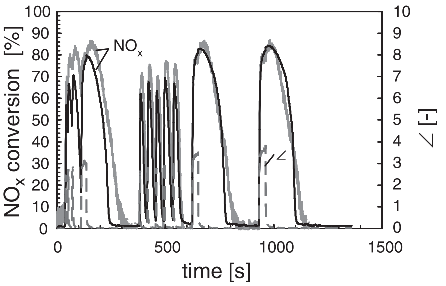

18a) Texh. = 229°C, NO_2/NO_x = 44%,
GHSV = 73200h^{-1}

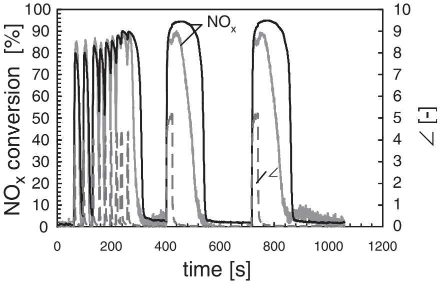

18b) Texh. = 278°C, NO_2/NO_x = 43%,
GHSV = 73800h^{-1}

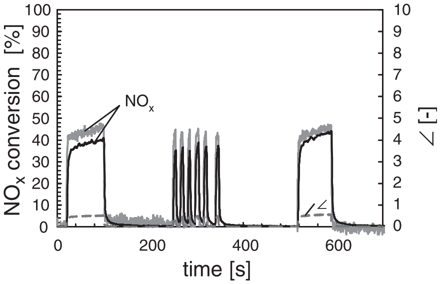

18c) Texh. = 456°C, NO_2/NO_x = 10%,
GHSV = 211000h^{-1}

FIG. 51. Passenger car diesel engine test bench measurements. Solid lines—measured NO_x conversion (gray), simulated NO_x conversion (black); dashed line—measured NH_3 dosing ratio α. Reprinted with permission from SAE Paper # 2006-01-0468 © 2006 *SAE International.*

between measured data and simulations can mainly be attributed to the fact that the measured NH_3 signal at the SCR catalyst inlet was used to calculate the NH_3/NO_x feed value for the simulation. Because of the limited measuring accuracy under such highly transient conditions, some deviations of the measured to the real NH_3/NO_x feed value could not be avoided. The combined exhaust treatment system DOC + SCR is further discussed in the next section.

VIII. Combined Aftertreatment Systems

The different catalyst models within the simulation environment ExACT are used for the simulation of combined aftertreatment systems, when exhaust conditions for a catalyst are influenced by its upstream component and changes in one catalyst affect all components further down the line. An application example is given in the following section and in Chatterjee *et al.* (2006). It investigates a combined system of DOC and SCR catalyst. Further examples for such combined systems to be investigated are DOC and NSRC or combinations of different catalyst technologies with DPF.

As discussed, the low temperature deNO_x efficiency of SCR converters for automotive exhaust aftertreatment can be significantly enhanced by converting part of the nitric oxide to NO_2, e.g. by means of a DOC located upstream of the SCR. In fact, the so-called "fast" SCR reaction, involving the reaction between NH_3 and equimolar amounts of NO and NO_2, can be faster by one order of magnitude than the "standard" SCR in the low-T region (Ciardelli *et al.*, 2007a; Koebel *et al.*, 2001). Effective exploitation of fast SCR reactivity is certainly important
in order to meet the stringent forthcoming automotive NO_x emission limits.

To study the influence of NO_2 on SCR efficiency, ESC and ETC test cycles with 0% and 50% NO_2/NO_x ratio in front of SCR catalyst were simulated. However, during transient test cycle operating conditions, a constant supply of optimum 50% NO_2/NO_x ratio will be difficult to achieve. NO to NO_2 conversion over a DOC is dependent on exhaust temperature, space velocity and exhaust composition. Because of transient operating conditions, it becomes furthermore a function of time. Exploiting the fast SCR reaction is thus limited by the realistically achievable NO_2/NO_x ratio in front of the SCR catalyst. To investigate this, ESC and ETC test cycles were also simulated for a combined system of DOC and SCR, where the NO_2/NO_x ratio in front of the SCR is defined by the NO_2 conversion over the DOC (Fig. 52).

In the simulations, extruded monoliths of commercial V_2O_5–WO_3/TiO_2-type SCR catalyst material with medium–high V content were investigated, with 300 cpsi and a total SCR volume of 18 L. A $NH_3/NO_{x,in}$ dosing ratio of $\alpha = 1$ was used for all simulations, this makes the different simulation cases easier to compare, otherwise the results would be biased by the respective dosing strategy. For the DOC, a Pt-type catalyst was chosen. DOC geometry and volume was adapted for optimum DOC and SCR system performance.

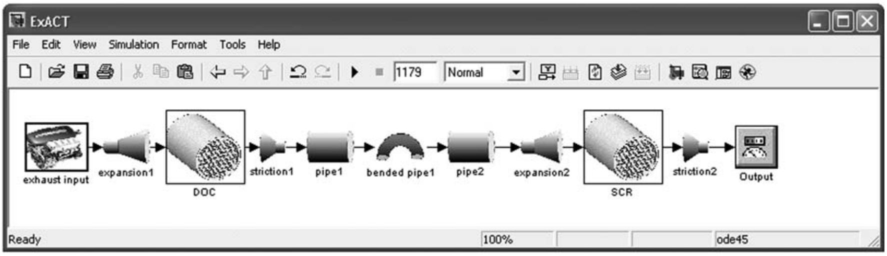

FIG. 52. Combined system model for DOC and SCR.

TABLE VII

TOTAL SIMULATED NO_x CONVERSION EFFICIENCIES FOR SCR WITH 0% NO_2/NO_x INLET, 50% NO_2/NO_x INLET AND FOR DOC AND SCR COMBINED SYSTEM

NO_x conversion	ESC (%)	ETC (%)
0% NO_2/NO_x	90.7	87.5
50% NO_2/NO_x	94.0	94.9
Combined DOC and SCR	93.6	91.8

Source: Chatterjee *et al.* (2006). Reprinted with permission from SAE Paper ♯ 2006-01-0468 © 2006 *SAE International.*

As already discussed, the optimum catalyst efficiency is obtained for a NO_2/NO_x ratio of 50%. The ESC and ETC simulation outputs for these input conditions can be regarded as a benchmark result, disregarding the NH_3 slip. The comparison with the baseline simulation without NO_2 in Fig. 54 reveals that NO_2 improves the SCR efficiency significantly. The total conversion efficiency is increased from 90.7% to 94.0% for the ESC and from 87.5% to 94.9% for the ETC, cf. Table VII. The improvements can mainly be attributed to the higher conversion rates in the colder parts of the test cycles (e.g., 850s–1,000s in the ESC).

ESC and ETC diesel oxidation catalyst simulation results in Fig. 53 show that the NO_2/NO_x ratio behind the DOC varies from 30% to 60% over the ESC and from 10% to 80% over the ETC for the configuration studied, with a mean value of approximately 40%. Using these simulated NO_2/NO_x ratios behind the DOC as input for the SCR test cycle simulations, lower conversion efficiencies are obtained compared to the 50% NO_2 case. However, Fig. 54 and the values in Table VII indicate that there is still a significant increase in the total NO_x conversion compared to the simulation without NO_2 in the inlet feed. This also confirms that the chosen DOC geometry and volume is quite well adapted to the specific application.

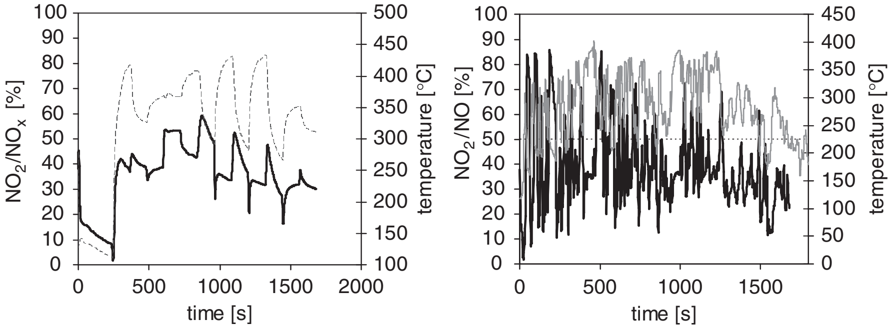

FIG. 53. Simulation of transient NO to NO_2 conversion and temperature at DOC outlet during ESC (left) and ETC (right) test cycle, simulated NO_2/NO_x ratio: solid black line, temperature: dashed gray line (Chatterjee *et al.*, 2006). Reprinted with permission from SAE Paper # 2006-01-0468 © 2006 *SAE International.*

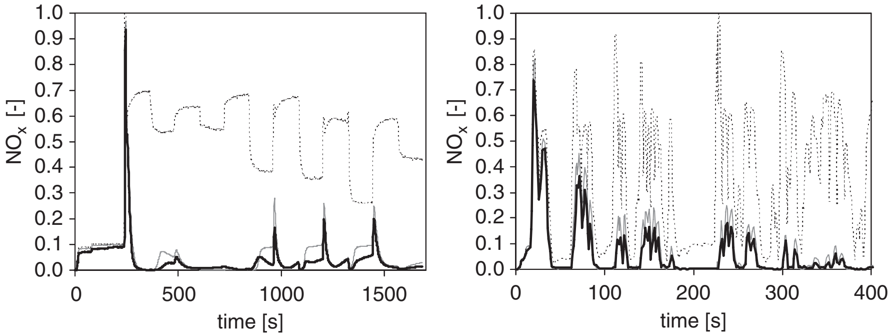

FIG. 54. Normalized NO_x concentrations before and after SCR during ESC (left) and ETC (right) test cycle simulation with $\alpha = 1$ (concentrations normalized by the maximum inlet value). Measured inlet concentration: dotted black line, simulated outlet concentration for NO_2/NO_x inlet = 0: dashed gray line, simulated outlet concentration for NO_2/NO_x inlet simulated with pre-DOC: solid black line (Chatterjee *et al.*, 2006). Reprinted with permission from SAE Paper # 2006-01-0468 © 2006 *SAE International.*

Overall, the simulation results show that NO_2 in the inlet feed of the SCR catalyst offers the potential for improving the NO_x conversion efficiency. Up to 7% improvement were obtained for best case conditions ($\alpha = 1$, $NO_2/NO_x = 50\%$) in the simulation. How much of this improvement can be achieved under application conditions is determined by the design of the DOC (e.g., volume, noble metal loading) and the optimum urea dosage strategy which is needed in order to avoid NH_3 slip.

IX. Summary and Conclusions

Exhaust emission legislation has become more and more stringent over the last years, demanding for lower engine raw emissions and more efficient exhaust converters. Simultaneous low emission limits for different species, e.g. PM and NO_x, lead to the development of combined aftertreatment systems, consisting of different catalyst technologies and particulate filter. Simulation can make a considerable contribution to shorten the time and lower the cost of the system development. In this publication, the current status of exhaust aftertreatment simulation tools used in automotive industry is reviewed. The developed models for DOC with HC adsorption, NSRC and catalyst for SCR of NO_x by NH_3 (urea) were included into the common simulation environment ExACT, which enables simulation of complete combined exhaust aftertreatment systems.

To model mass and energy transport in monolith systems, several approaches are discussed, leading from a representative channel spatially 1D approach to 2D (1D + 1D) modeling explicitly including washcoat diffusion. Correlations are given to describe heat and mass transfer between bulk gas phase and catalytic washcoat. For the detailed study of reaction–transport interactions in the porous catalytic layer, the spatially 3D model of the computer-reconstructed washcoat section can be employed.

The process of the derivation of global reaction kinetics is explained, based on a stage-wise approach. Microreactor experiments on washcoat powder enable the study of the reaction mechanism without diffusion limitations. Reactions are studied individually, first the simplest reacting systems, then adding components toward the full gas mixture. Parameter estimation can be greatly aided by numerical optimization of the resulting least-squares objective function. The resulting kinetic equations can be directly validated on lab scale, performing experiments on small monolith samples with synthetic gas mixtures. The final validation is undertaken with driving cycle dynamometer or engine test bench data, showing the applicability of the model under real exhaust conditions.

The developed model for the DOC describes the most important reactions taking place under lean operating conditions: HC adsorption, CO, H_2, HC and NO oxidation reactions as well as lean NO_x reduction by HC. The kinetic parameters were evaluated from monolith sample lab experiments and validated on passenger car driving cycle measurement data, showing that the model after calibration is well able to describe temperature and species conversion in DOC over wide range of noble metal loadings and catalyst ageing levels.

The NSRC is operated in periodic lean/rich regime: in the course of a long lean phase, typically lasting for several minutes, NO_x are stored on the catalyst surface. Then, the accumulated NO_x are released and reduced within a short rich phase, lasting for several seconds. An effective model for this catalyst has been developed, describing NO_x storage and release on $BaCO_3$ and also including CO, H_2, HC and NO oxidation reactions, water gas shift and steam reforming, oxygen storage and release and NO reduction reactions. The model was designed to efficiently describe the most important phenomena taking place on the NSRC, while at the same time keeping the complexity of the reaction scheme and the number of kinetic parameters on a low level. It was adapted to monolith sample lab experiments and validated on passenger car driving cycle and commercial vehicle engine test bench measurement data, showing its applicability for a wide range of catalyst sizes, operating conditions and catalyst ageing levels. The model was applied to study the influence of catalyst regeneration status, catalyst geometry, exhaust temperature and NO_x raw emissions on NSRC conversion over a complete driving cycle.

The SCR of NO_x with urea has over the last two decades proven to be the most effective commercial deNO_x process for stack gases from power plants and other stationary sources. It is increasingly studied and applied in diesel passenger cars and commercial vehicles, where mostly colder, non-stationary conditions and more complex gas mixtures are encountered. A detailed kinetic model of the complete NO/NO_2–NH_3 reacting system was derived on microreactor scale and validated on monolith samples with synthetic gas mixtures, as well as on commercial vehicle engine test bench and on diesel passenger car dynamometer measurement data. The model is well applicable over this wide range in catalyst sizes and operating conditions.

Finally, an application example for a combined aftertreatment system simulation has been given and discussed, investigating a combination of a DOC and a SCR catalyst. It shows how NO_x conversions in the urea–SCR converter over the ESC and ETC driving cycles can be greatly improved by NO_2 formation in the DOC placed upstream. The system model is used to evaluate DOC size under steady state, but also under transient cycle operation. Further examples for such combined systems which can be investigated are DOC and NSRC or combinations of different catalyst technologies with DPF.

LIST OF SYMBOLS

A. Latin Letters

a	density of external surface area in monolith, m^2/m^3
k_0	pre-exponential factor of reaction, dimension depends on the reaction
c	concentration (bulk gas), mol/m^3

c^{s}	concentration in washcoat pores, mol/m^3
c_p	specific heat capacity of gas, J/kg/K
$c_p{}^{\mathrm{s}}$	effective specific heat capacity of solid phase, J/kg/K
d	monolith channel diameter, m
D	diffusivity, m^2/s
E	activation energy of reaction, J/mol
G	kinetic inhibition term
J	number of reactions
k	kinetic constant of reaction, dimension depends on the reaction
k_{c}	mass transfer coefficient, m/s
k_{h}	heat transfer coefficient, J/m^2/K/s
K	number of gas components
$K_{\mathrm{a}},K_{\mathrm{LH}}$	kinetic inhibition constants
K^{eq}	thermodynamic equilibrium constant
L	length of monolith, m
M	number of surface-deposited components
p	pressure, Pa
r	transverse spatial coordinate in catalytic washcoat layer, m
r_{p}	pore radius, m
R_j	reaction rate, mol/m^3/s (related to washcoat volume)
R	universal gas constant, 8.31434 J/mol/K
S	frontal area of monolith, m^2
SV	gas hourly space velocity, 1/s (defined at standard $T = 273.15\,\mathrm{K}$ and $p = 101{,}325\,\mathrm{Pa}$)
t	time, s
T	temperature of gas, K
T^{s}	temperature of solid phase, K
T^{e}	temperature of surroundings, K
u	linear gas velocity, m/s
V	volume, m^3
$\dot{V}$	volumetric flow rate, m^3/s
w	weight of component in sum of squares, 1
W	effective heat loss coefficient, J/m^3/K/s
X,Y,Z	orthogonal spatial coordinates in 3D washcoat section, m
X	component conversion, 1
$\mathbf{x}$	vector of kinetic parameters to be optimized
y	molar fraction (bulk gas), 1
y^{s}	molar fraction in washcoat pores, mol/m^3
z	spatial coordinate along monolith (axial), m

B. Greek Letters

α	NH_3 dosing ratio in NH_3–SCR, 1
α	parameter for surface coverage dependence in NH_3–SCR kinetics, 1

β	O_2 reaction order in NH_3–SCR kinetics, 1
γ	inhibition term in NH_3–SCR kinetics, 1
ΔH_r	standard reaction enthalpy, J/mol
δ	thickness of catalytic washcoat layer, m
ε^g	open frontal area fraction (monolith), void fraction (catalyst bed), 1
ε^s	porosity of catalytic washcoat layer, 1
η	effectiveness factor, 1
θ	surface coverage of adsorbed component, 1
μ	dynamic viscosity, Pa.s
ν	stoichiometric coefficient, mol//mol
λ	heat conductivity, J/m/K/s
ρ	gas density, kg/m^3
ρ^s	apparent density of solid phase (incl. pores), kg/m^3
τ	tortuosity, 1
φ^s	volume fraction of catalytic washcoat in entire solid phase, 1
Φ	Thiele modulus, 1
ψ	relative surface concentration of stored component, 1
Ψ^{cap}	storage capacity, mol/m^3 (related to catalytic washcoat volume)
ω	volume diffusion constant, m^3/mol
Ω	adsorption capacity, mol/m^3 (related to catalytic washcoat volume)

C. Subscripts and Superscripts

a	denotes inhibition constant in DOC and NSRC kinetics
ads	denotes NH_3 adsorption in NH_3–SCR
adsnit	denotes NH_4NO_3* adsorption in NH_3–SCR
amm	denotes NO_2 disproportion in NH_3–SCR
calc	calculation
dec	denotes NH_4NO_3* desorption in NH_3–SCR
des	denotes NH_3 desorption in NH_3–SCR
eq	equilibrium
exp	experiment
FST	denotes HNO_3 reaction in NH_3–SCR
g	gas
in	inlet
j	index of reaction
k	index of gas component
LH	denotes inhibition constant in NH_3–SCR kinetics
m	index of surface-deposited component
meas	measurement
M	macro
nit	denotes HONO reduction in NH_3–SCR

NO	denotes NO–deNO_x reaction in NH_3–SCR
NO_2	denotes direct NO_2–deNO_x reaction in NH_3–SCR
N_2O	denotes N_2O formation in NH_3–SCR
μ	micro
out	outlet
ox	denotes NH_3 oxidation in NH_3–SCR
ref	reference
s	solid phase (washcoat and monolith substrate)
sim	simulation
vol	volume
w	washcoat
wt	weight

ABBREVIATIONS

1D	spatially one-dimensional
cpsi	channels per square inch (cross-sectional monolith channel density)
(C)DPF	(Coated) diesel particulate filter
DOC	diesel oxidation catalyst
deNO_x	abatement of nitrogen oxides
EPA	Environmental Protection Agency (USA)
ESC	European stationary driving cycle (for heavy-duty vehicles)
ETC	European transient driving cycle (for heavy-duty vehicles)
ExACT	Exhaust Aftertreatment Components Toolbox
FTP	Federal test procedure, US driving cycle
g/bhp-hr	grams per brake horsepower-hour
HC	hydrocarbon(s)
LEV	low emission vehicle
LNT	lean NO_x trap (equivalent to NSRC)
MR	modified redox mechanism in SCR
NEDC	new European driving cycle
NM	noble metal(s)
NMHC	non-methane hydrocarbons
NMOG	non-methane organic gases
NO_x	nitrogen oxides, NO and NO_2 only
NSRC	NO_x storage and reduction catalyst
PM	particulate matter
SC03	US driving cycle with air-conditioning device switched on
SCR	selective catalytic reduction of NO_x
SOF	soluble organic fraction in TPM

TPM	total particulate matter
TPD	temperature-programmed desorption (temperature ramp)
TPR	temperature-programmed reaction (temperature ramp)
TRM	transient response method
TWC	three-way catalyst
US06	US highway driving cycle

ACKNOWLEDGMENTS

Miloš Marek and Petr Kočí thank to Teuvo Maunula and Matti Härkönen from Ecocat Oy for the co-operation and discussions that supported the development of the NSRC and DOC kinetic models.

REFERENCES

Abdulhamid, H., Dawody, J., Fridell, E., and Skoglundh, M. *J. Catal.* **244**, 169 (2006a).

Abdulhamid, H., Fridell, E., Dawody, J., and Skoglundh, M. J. *J. Catal.* **241**, 200 (2006b).

ACEA. Final report on selective catalytic reduction—June 2003. http://europa.eu.int/comm/enterprise/automotive/mveg_meetings/meeting94/scr_paper_final.pdf (2003).

Amberntsson, A., Skoglundh, M., Jonsson, M., and Fridell, E. *Catal. Today* **73**, 279 (2002).

AMESim. http://www.amesim.com/applications/automotive/exhaust-aftertreat.aspx (2006).

Ansell, G. P., Benett, P. S., Cox, Y. P., Frost, Y. C., Gray, P. G., Jones, A. -M., Rajaram, R. R., Walker, A. P., Litorell, M., and Smedler, G. *Appl. Catal. B: Environ.* **10**, 183 (1996).

Apostolescu, N., Schroder, T., and Kureti, S. *App.Catal. B: Environ.* **51**, 43 (2004).

Aris, R., "The Mathematical Theory of Diffusion and Reaction in Permeable Catalysts", vols. 1 and 2, Oxford University Press, London (1975).

AVL BOOST. http://www.avl.com (2006).

Balakotaiah, V., Nikunj, G., and West, D. H. *Chem. Eng. Sci.* **55**, 5367 (2000).

Balakotaiah, V., and West, D. H. *Chem. Eng. Sci.* **57**, 1269 (2002).

Beeckman, J. W. *Ind. Eng. Chem. Res.* **30**, 428 (1991).

Boaro, M., Giordano, F., Recchia, S., Dal Santo, V., Giona, M., and Trovarelli, A. *Appl. Catal. B: Environ.* **52**, 225 (2004).

Braun, J., Hauber, T., Toebben, H., Zacke, P., Chatterjee, D., Deutschmann, O., and Warnatz, J. SAE Technical Paper 2000-01-0211 (2000).

Broqvist, P., Grönbeck, H., Fridell, E., and Panas, I. *Catal. Today* **96**, 71 (2004).

Burch, R. *Catal. Rev.* **46**, 271 (2004).

Burch, R., Breen, J. P., and Meunier, F. C. *Appl. Catal. B: Environ.* **39**, 283 (2002).

Cant, N. W., Liu, I. O. Y., and Patterson, M. J. *J. Catal.* **243**, 309 (2006).

Castoldi, L., Matarrese, R., Lietti, L., and Forzatti, P. *Appl. Catal. B: Environ.* **64**, 25 (2006).

Chatterjee, D., Burkardt, T., Bandl-Konrad, B., Braun, T., Tronconi, E., Nova, I., and Ciardelli, C. SAE Technical Paper 2005-01-1965 (2005).

Chatterjee, D., Burkhardt, T., Weibel, M., Nova, I., Grossale, A., and Tronconi, E. SAE Technical Paper 2007-01-1136 (2007).

Chatterjee, D., Burkardt, T., Weibel, M., Tronconi, E., Nova, I., and Ciardelli, C. SAE Technical Paper 2006-01-0468 (2006).

Chatterjee, D., Deutschmann, O., and Warnatz, J. *Faraday Discuss.* **119**, 371 (2001).

Chen, D. K. S., Oh, S. H., Bisset, E. J., and van Ostrom, D. L. SAE Technical Paper 880282 (1988).

Choi, J.-S., Partridge, W. P., Epling, W. S., Currier, N. W., and Yonushonis, T. M. *Catal. Today* **114**, 102 (2006).

Ciardelli, C., Nova, I., Tronconi, E., Ascherfeld, M., and Fabinski, W. *Top. Catal.* **42–43**, 161 (2007b).

Ciardelli, C., Nova, I., Tronconi, E., Bandl-Konrad, B., and Chatterjee, D. *Chem. Commun.* **2718**, (2004b).

Ciardelli, C., Nova, I., Tronconi, E., Bandl-Konrad, B., Chatterjee, D., Weibel, M., and Krutzsch, B. *Appl. Catal. B: Environ.* **70**, 80 (2007a).

Ciardelli, C., Nova, I., Tronconi, E., Konrad, B., Chatterjee, D., Ecke, K., and Weibel, M. *Chem. Eng. Sci.* **59**, 5301 (2004a).

Cumaranatunge, L., Mulla, S. S., Yezerets, A., Currier, N. W., Delgass, W. N., and Ribeiroa, F. H. *J. Catal.* **246**, 29 (2007).

Dieselnet. http://www.dieselnet.com (2007).

Donati, G., and Buzzi-Ferraris, G. *Chem. Eng. Sci.* **29**, 1504 (1974).

Dubien, C., Schweich, D., Mabilon, G., Martin, B., and Prigent, M. *Chem. Eng. Sci.* **53**, 471 (1997).

Dvořák, L., Pinkas, P., and Marek, M. *Catal. Today* **20**, 449 (1994).

Epling, W., Campbell, L., Yezerets, A., Currier, N., and Parks, J. *Catal. Rev.* **46**, 163 (2004a).

Epling, W., Parks, J., Campbell, G., Yezerets, A., Currier, N., and Campbell, L. *Catal. Today* **96**, 21 (2004b).

Farrauto, R. J., and Kenneth, E. V. *Appl. Catal. B: Environ.* **10**, 29 (1996).

Finlayson, B. A., "Nonlinear Analysis in Chemical Engineering". McGraw Hill, New York (1980).

Forzatti, P., Castoldi, L., Nova, I., Lietti, L., and Tronconi, E. *Catal. Today* **117**, 316 (2006).

Forzatti, P., Lietti, L., and Tronconi, E., Nitrogen oxides removal, *in* "Industrial Encyclopedia of Catalysis" (I. T. Horvath New York, Wiley (2002).

Froment, G. F., and Bischoff, K. B. "Chemical Reactor Analysis and Design". Wiley, NY (1979).

Froment, G. F., and Bischoff, K. B., "Chemical Reactor Analysis and Design". 2nd edn., Wiley, New York (1990).

Goralski, C. T. Jr., Chanko, T., Lupescu, J., and Ganti, C. SAE Technical Paper 2000-01-0655 (2000).

Groppi, G., Belloli, A., Tronconi, E., and Forzatti, P. *AIChE J.* **41**, 2250 (1995a).

Groppi, G., Belloli, A., Tronconi, E., and Forzatti, P. *Chem. Eng. Sci.* **50**, 2705 (1995b).

Groppi, G., Tronconi, E., and Forzatti, P. *Catal. Rev. Sci. Eng.* **41**, 227 (1999).

GT-POWER. http://www.gtisoft.com/img/broch/broch_gtpower.pdf (2006).

Gulati, S. T., Makkee, M., and Setiabudi, A., *in* "Structured Catalysts and Reactors" (A. Cybulski, and J. A. Moulijn Eds.), pp. 663–700. CRC Taylor & Francis, Boca Raton (2006).

Güthenke, A., Chatterjee, D., Weibel, M., Waldbüßer, N., Kočí, P., Marek, M., and Kubíček, M. *Chem. Eng. Sci.* **62**, 5357–5363 (2007a).

Güthenke, A., Chatterjee, D., Weibel, M., Waldbüßer, N., Thinschmidt, B., Kočí, P., Marek, M., and Kubíček, M. SAE Technical Paper 2007-01-1117 (2007b).

Harmsen, J. M., Hoebink, J. H., and Schouten, J. C. *Ind. Eng. Chem. Res.* **39**, 599 (2000).

Harmsen, J. M., Hoebink, J. H., and Schouten, J. C. *Chem. Eng. Sci.* **56**, 2019 (2001).

Hayes, R. E., Kolaczkowski, S. T., Li, P. K. C., and Awdry, S. *Appl. Catal. B: Environ.* **25**, 93 (2000).

Hayes, R. E., Liu, B., Moxom, R., and Votsmeier, M. *Chem. Eng. Sci.* **59**, 3169 (2004).

Hayes, R. E., Liu, B., and Votsmeier, M. *Chem. Eng. Sci.* **60**, 2037 (2005).

Heck, R. H., Farrauto, R. J., and Gulati, S. T., "Catalytic Air Pollution Control". 2nd edn., Wiley, New York (2002).

Heck, R. H., Wei, J., and Katzer, J. R. *AIChE J.* **22**, 477 (1976).

Hepburn, J. S., Kenney, T., McKenzie, J., Thanasiu, E., and Dearth, M. SAE Technical Paper 982596 (1998).

Hepburn, J. S., Thanasiu, E., Dobson, D. A., and Watkins, W. L. SAE Technical Paper 962051 (1996).

Himmelblau, D. M., "Process Analysis by Statistical Methods". Wiley, New York (1970).

Hoebink, J. H. B. J., van Gemert, R. A., van den Tillaart, J. A. A., and Marin, G. B. *Chem. Eng. Sci.* **55**, 1573 (2000).

Hoebink, J. H. B. J., Harmsen, J. M. A., Scholz, C. M. L., Marin, G. B., and Schouten, J. C., *in* "Structured Catalysts and Reactors" (A. Cybulski, and J. A. Moulijn Eds.), pp. 311–354. CRC Taylor & Francis, Boca Raton (2006).

IFP Institut Francais du Petrole. http://www.ifp.fr (2006).

Jacobs, T., Chatterjee, S., Walker, A. P., Conway, R, Kramer, J., and Mueller-Haas, K. SAE Technical Paper 2006-01-0213 (2006).

Jahn, R., Šnita, D., Kubíček, M., and Marek, M. *Catal. Today* **38**, 39 (1997).

Jahn, R., Šnita, D., Kubíček, M., and Marek, M. *Catal. Today* **70**, 393 (2001).

Jirát, J., Kubíček, M., and Marek, M. *Catal. Today* **53**, 583 (1999a).

Jirát, J., Kubíček, M., and Marek, M. *Chem. Eng. Sci.* **56**, 1597 (2001).

Jirát, J., Štěpánek, F., Kubíček, M., and Marek, M. *Chem. Eng. Sci.* **54**, 2609 (1999b).

Joubert, E., Courtois, X., Marecot, P., Canaff, C., and Duprez, D. *J. Catal.* **243**, 252 (2006).

Kabin, K. S., Khanna, P., Muncrief, R. L., Medhekar, V., and Harold, M. P. *Catal. Today* **114**, 72 (2006).

Kapteijn, F., and Moulijn, J. A. Laboratory reactors, *in* "Handbook of Heterogeneous Catalysis" (G. Ertl, H. Knözinger, and J. Weitkamp, Eds.), vol. 3, p. 1359. VCH, Weinheim, Germany (1997).

Kapteijn, F., Singoredjo, L., Dekker, N. J. J., and Moulijn, J. A. *Ind. Eng. Chem. Res.* **32**, 445 (1993).

Kašpar, J., Fornasiero, P., and Jockey, N. *Catal. Today* **77**, 419 (2003).

Kato, S., Matsuda, S., Kamo, T., Nakajima, F., Kuroda, H., and Narita, T. *J. Phys. Chem.* **85**, 4099 (1981).

Kim, Y-W., Sun, J., Kolmanovsky, I., and Konsol, J. SAE Technical Paper 2003-01-1164 (2003).

Kirchner, T., and Eigenberger, G. *Chem. Eng. Sci.* **51**, 2409 (1996).

Kobayashi, T., Yamada, T., and Kayano, K. SAE Technical Paper 970745 (1997).

Kočí, P. PhD Thesis, Institute of Chemical Technology, Prague (2005).

Kočí, P., Kubíček, M., and Marek, M. *Ind. Eng. Chem. Res.* **43**, 4503 (2004a).

Kočí, P., Kubíček, M., and Marek, M. *Catal. Today* **98**, 345 (2004b).

Kočí, P., Kubíček, M., Marek, M., Maunula, T., and Härkönen, M. *Chem. Eng. J.* **97**, 131 (2004c).

Kočí, P., Nevoral, V., Záhrubský, M., Kubíček, M., and Marek, M. *Chem. Eng. Sci.* **59**, 5597 (2004d).

Kočí, P., Štěpánek, F., Kubíček, M., and Marek, M. *Chem. Eng. Sci.* **61**, 3240 (2006).

Kočí, P., Štěpánek, F., Kubíček, M., and Marek, M. *Chem. Eng. Sci.* **62**, 5380–5385 (2007a).

Kočí, P., Schejbal, M., Trdlička, J., Gregor, T., Kubíček, M., and Marek, M. *Catal. Today* **119**, 64 (2007b).

Koebel, M., and Elsener, M. *Chem. Eng. Sci.* **53**, 657 (1998).

Koebel, M., Elsener, M., and Madia, G. *Ind. Eng. Chem. Res.* **40**, 52–59 (2001).

Koebel, M., Madia, G., and Elsener, M. *Catal. Today* **73**, 239 (2002).

Kojima, S., Baba, N., Matsunaga, S., Senda, K., Katoh, K., and Itoh, T. SAE Technical Paper 2001-01-1297 (2001).

Koltsakis, G. C., Konstantinidis, P. A., and Stamatelos, A. M. *Appl. Catal. B: Environ.* **12**, 161 (1997).

Koltsakis, G. C., and Stamatelos, A. M. *Prog. Energy Combust. Sci.* **23**, 1 (1997).

Koltsakis, G. C., and Stamatelos, A. M. SAE Technical Paper 2000-01-0654 (2000).

Kosek, J., Štěpánek, F., and Marek, M. *Adv. Chem. Eng.* **30**, 137 (2005).

Kruglov, A. V., and Aris, R. *AIChE J.* **41**, 2393 (1995).

Kryl, D., Kočí, P., Kubíček, M., Marek, M., Maunula, T., and Härkönen, M. *Ind. Eng. Chem. Res.* **44**, 9524 (2005).

Kubíček, M., Pinkas, P., Jirát, J., Šnita, D., and Marek, M. *Comp. Chem. Eng.* **21**, 757 (1997).

Kubíček, M., and Marek, M., "Computational Methods in Bifurcation Theory and Dissipative Structures". Springer Verlag, Heidelberg, New York (1983).

Lambrou, P. S., Costa, C. N., Christou, S. Y., and Efstathiou, A. M. *Appl. Catal. B: Environ.* **54**, 237 (2004).

Leclerc, J. P., and Schweich, D., Modelling catalytic monoliths for automobile emission control, *in* "Chemical Reactor Technology for Environmentally Safe Reactors and Products" (H. I. de Lasa, G. Dogu, and A. Ravella, Eds.), pp. 547–575. Kluwer Academic Publishers, Netherlands (1993).

Lie, A. B. K., Hoebink, J. H. B. J., and Marin, G. B. *Chem. Eng. J.* **53**, 47 (1993).

Lietti, L., Forzatti, P., Nova, I., and Tronconi, E. *J. Catal.* **204**, 175 (2001).

Lietti, L., Nova, I., Camurri, S., Tronconi, E., and Forzatti, P. *AIChE J.* **43**, 2559 (1997).

Lietti, L., Nova, I., Tronconi, E., and Forzatti, P., Unsteady-state kinetics of DeNOx-SCR catalysis, *in* "Reaction Engineering for Pollution Prevention" (M. A. Abraham, and R. P. Hesketh Eds.), pp. 85–112. Elsevier Science, Amsterdam (2000).

Madia, G., Koebel, M., Elsener, M., and Wokaun, A. *Ind. Eng. Chem. Res.* **41**, 351 (2002).

Marek, M., and Schreiber, I., "Chaotic Behaviour of Deterministic Dissipative Systems". 2nd edn., Cambrige University Press, Cambridge (1995).

Matlab/Simulink. http://www.mathworks.com (2006).

Matsumoto, S., Ikeda, Y., Suzuki, H., Ogai, M., and Miyoshi, N. *Appl. Catal. B: Environ.* **25**, 115 (2000).

Maunula, T., Vakkilainen, A., Heikkinen, R., and Härkönen, M. SAE Technical Paper 2001-01-3665 (2001).

Mears, D. E. *Ind. Eng. Chem. Des. Dev.* **10**, 541 (1971).

Monolith. http://www.vscht.cz/monolith (2007).

Montreuil, C. N., Williams, S. C., and Adamczyk, A. A. SAE Technical Paper 920096 (1992).

Mukadi, L. S., and Hayes, R. E. *Comput. Chem. Eng.* **26**, 439 (2002).

Muncrief, R. L., Khanna, P., Kabin, K. S., and Harold, M. P. *Catal. Today* **98**, 393 (2004).

Nakatani, K., Hirota, S., Takeshima, S., Itoh, K., Tanaka, T., and Dohmae, K. SAE Technical Paper 2002-01-0957 (2002).

Nibbelke, R. H., Nievergeld, A. J., Hoebink, J. H., and Marin, G. B. *Appl. Catal. B: Environ.* **19**, 245 (1998).

Nova, I., Castoldi, L., Lietti, L., Tronconi, E., Forzatti, P., Prinetto, F., and Ghiotti, G. *J. Catal.* **222**, 377 (2004).

Nova, I., Castoldi, L., Lietti, L., Tronconi, E., Forzatti, P., Prinetto, F., and Ghiotti, G. SAE Technical Paper 2005-01-1085 (2005).

Nova, I., Lietti, L., Tronconi, E., and Forzatti, P. *Catal. Today* **60**, 73 (2000).

Nova, I., Tronconi, E., Ciardelli, C., Chatterjee, D., and Bandl-Konrad, B. *AIChE J.* **52**, 3222 (2006a).

Nova, I., Tronconi, E., Ciardelli, C., Chatterjee, D., and Bandl-Konrad, B. *Catal. Today* **114**, 3 (2006b).

Nova, I., Lietti, L., Castoldi, L., Tronconi, E., and Forzatti, P. *J. Catal.* **239**, 244 (2006c).

Nova, I., Tronconi, E., Ciardelli, C., Chatterjee, D., and Weibel, M. *Topics in Catal.* **42–43**, 43 (2007).

Oh, S. H., and Cavendish, J. C. *Ind. Eng. Chem. Prod. Res. Dev.* **21**, 29 (1982).

Oh, S. H., and Cavendish, J. C. *AIChE J.* **31**, 935 (1985).

Olsson, L., Blint, R. J., and Fridell, E. *Ind. Eng. Chem. Res.* **44**, 3021 (2005).

Olsson, L., Fridell, E., Skoglundh, M., and Andersson, B. *Catal. Today* **73**, 263 (2002).

Olsson, L., Persson, H., Fridell, E., Skoglundh, M., and Andersson, B. *J. Phys. Chem. B* **105**, 6895 (2001).

Olsson, L., Westerberg, B., Persson, H., Fridell, E., Skoglundh, M., and Andersson, B. *J. Phys. Chem. B* **103**, 10433 (1999).

Pihl, J. A., Parks, J. E. II., Daw, C. S., and Root, T. W. SAE Technical Paper 2006-01-3441 (2006).

Pinkas, P., Šnita, D., Kubíček, M., and Marek, M. *Chem. Eng. Sci.* **49**, 5347 (1995).

Poling, B. E., Prausnitz, J. M., and Oconnel, J. P., "The Properties of Gases and Liquids". McGraw-Hill, New York (2001).

Ramanathan, K., Balakotaiah, V., and West, D. H. *Chem. Eng. Sci.* **58**, 1381 (2003).

Rohr, F., Peter, S. D., Lox, E., Kögel, M., Sassi, A., Juste, L., Rigaudeau, C., Belot, G., Gélin, P., and Primet, M. *Appl. Catal. B: Environ.* **56**, 201 (2005).

Sakamoto, Y., Okumura, K., Kizaki, Y., Matsunaga, S., Takahashi, N., and Shinjoh, H. *J. Catal.* **238**, 361 (2006).

Scholz, C. M. L., Gangwal, V. R., de Croon, M. H. J. M., and Schoulen, J. C. *J. Catal.* **245**, 215 (2007).

Schulte-Braucks, R. CAPOC 07 conference, Brussels, Belgium, 30th August (2006).

Shah, R. K., and London, T. C. Flow forced convection in ducts, *in* "Advances in Heat Transfer". Academic Press, New York (1978).

Sharma, M., Harold, M. P., and Balakotaiah, V. *Ind. Eng. Chem. Res.* **44**, 6264 (2005).

Siemund, S., Leclerc, J. P., Schweich, D., Prigent, M., and Castagna, F. *Chem. Eng. Sci.* **51**, 3709 (1996).

Starý, T., Šolcová, O., Schneider, P., and Marek, M. *Chem. Eng. Sci.* **61**, 5934 (2006).

Szanyi, J., Kwak, J., Hanson, J., Wang, C. M., Szailer, T., and Peden, C. H. F. *J. Phys. Chem. B* **109**, 7339–7344 (2005).

Takahashi, N., Shinjoh, H., Iijima, T., Suzuki, T., Yamazaki, K., Yokota, K., Suzuki, H., Miyoshi, N., Matsumoto, S., Tanizawa, T., Tanaka, T., Tateishi, S., and Kasahara, K. *Catal. Today* **27**, 63 (1996).

Tischer, S., and Deutschmann, O. *Catal. Today* **105**, 407 (2005).

Tronconi, E., and Beretta, A. *Catal. Today* **52**, 249 (1999).

Tronconi, E., Cavanna, A., and Forzatti, P. *Ind. Eng. Chem. Res.* **37**, 2341 (1998).

Tronconi, E., and Forzatti, P. *AIChE J.* **38**, 201 (1992).

Tronconi, E., Nova, I., Ciardelli, C., Chatterjee, D., Burkhardt, T., and Bandl-Konrad, B. *Catal. Today* **105**, 529 (2005).

Tronconi, E., Nova, I., Ciardelli, C., Chatterjee, D., and Weibel, M. *J. Catal.* **245**, 1 (2007).

Tuttlies, U., Schmeißer, V., and Eigenberger, G. *Chem. Eng. Sci.* **59**, 4731 (2004).

Twigg, M. V. *Catal. Today* **117**, 407 (2006).

Villa, P. L., Forzatti, P., Buzzi-Ferraris, G., Garone, G., and Pasquon, I. *Ind. Eng. Chem. Prod. Res. Dev.* **24**, 12 (1985).

Villadsen, J. V., and Michelsen, M. L., "Solution of Differential Equation Models by Polynomial Approximation". Prentice Hall, Inc. Englewood Cliffs, New Jersey (1978).

Villadsen, J. V., and Stewart, W. E. *Chem. Eng. Sci.* **22**, 1483 (1967).

Voltz, S., Morgan, C., Liederman, D., and Jacob, S. *Ind. Eng. Chem. Prod. Res. Dev.* **12**, 294 (1973).

Wakao, N., and Smith, J. M. *Chem. Eng. Sci.* **17**, 825 (1962).

Waldbüsser, N. Dissertation D386, Univ. Kaiserslautern (2005).

Wanker, R., Raupenstrauch, H., and Staudinger, G. *Chem. Eng. Sci.* **55**, 4709 (2000).

West, D. H., Balakotaiah, V., and Jovanovic, Z. *Catal. Today* **88**, 3 (2003).

Willey, R. J., Lai, H., and Peri, J. B. *J. Catal.* **130**, 319 (1991).

Wurzenberger, J., and Peters, B. SAE Technical Paper 2003-01-1002 (2003).

Wurzenberger, J., and Wanker, R. Multi-scale SCR modeling, SAE Technical Paper 2005-01-0948 (2005).
Yao, H. C., and Yu Yao, Y. F. *J. Catal.* **86**, 254 (1984).
Yeom, Y. H., Henao, J., Li, M., Sachtler, W. M. H., and Weitz, E. *J. Catal.* **231**, 181 (2005).
Young, L. C., and Finlayson, B. A. *AIChE J.* **22**, 343 (1976).
Zhang, F., Hayes, R. E., and Kolaczkowski, S. T. *Chem. Eng. Res. Des.* **82**, 481 (2004).
Zygourakis, K., and Aris, R. *Chem. Eng. Sci.* **38**, 733 (1983).

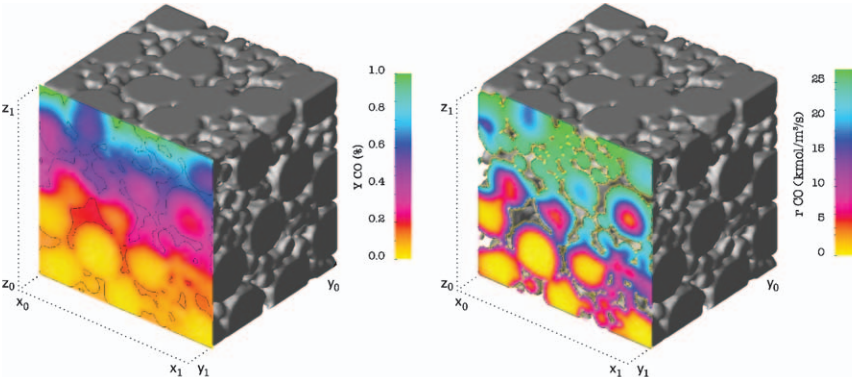

PLATE 2. Typical CO concentration and reaction rate profiles in the porous Pt/γ-Al_2O_3 catalyst reconstructed by particle-packing method. Mean hydraulic diameter of macropores $d_h^M = 300$ nm, macroporosity $\varepsilon^M = 18.1\%$. Free space corresponds to macropores, solid gray corresponds to mesoporous γ-Al_2O_3 with dispersed Pt. Length of the section edge 10 μm. Boundary Z_1:$y_{CO} = 1\%$, $y_{O_2} = 0.5\%$. (a) $T = 513$ K, (b) $T = 533$ K (Kočí *et al.*, 2007a) (for Black and White version, see page 122).

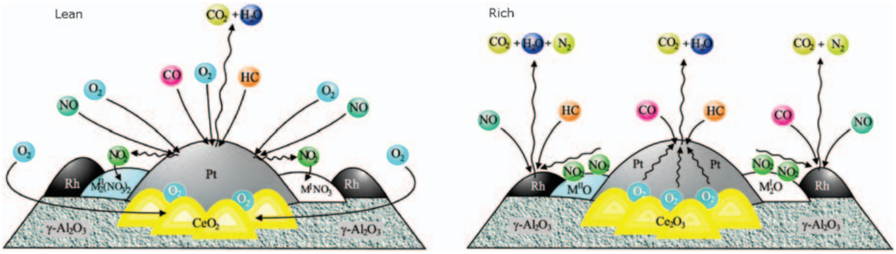

PLATE 3. Scheme of adsorption, desorption and reaction processes on the surface of the NSRC during lean and rich conditions (Kočí, 2005) (for Black and White version, see page 143).

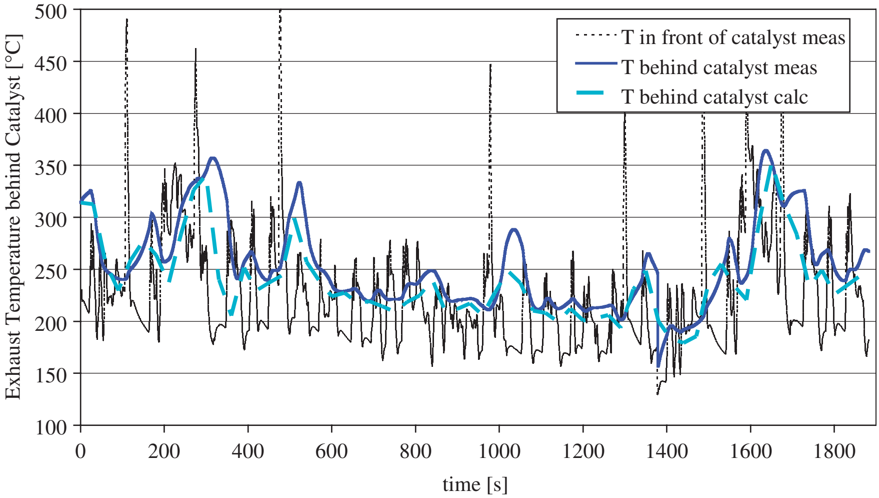

PLATE 4. Validation of the NSRC model for passenger car application—comparison of measured (meas) and calculated (calc) outlet temperatures during the FTP-75 driving cycle; fresh catalyst (Güthenke *et al.*, 2007a) (for Black and White version, see page 158).

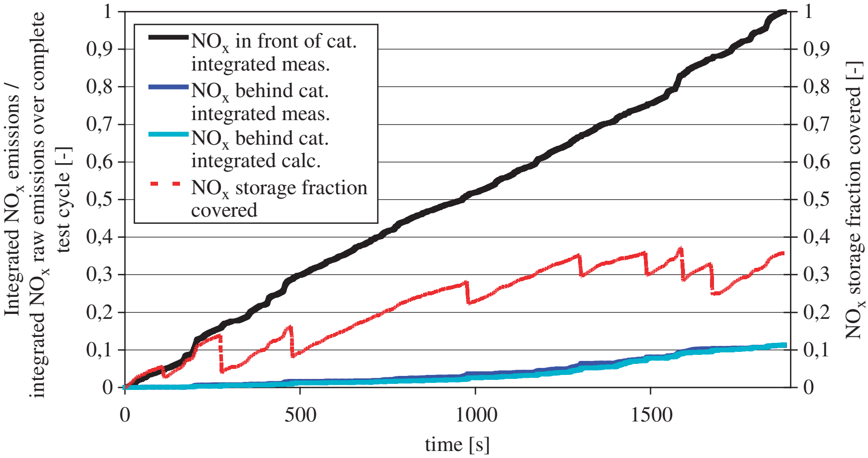

PLATE 5. Validation of the NSRC model for passenger car application—comparison of measured (meas) and calculated (calc) cumulative NO$_x$ emissions for the FTP-75 driving cycle; fresh catalyst (Güthenke *et al*., 2007a). The covered fraction of the NO$_x$ storage capacity (spatially averaged ψ_{NOx}) is calculated by the model. Integral NO$_x$ conversions X evaluated from experiment and simulation data: $X^{exp} = 88.9\%$, $X^{sim} = 88.3\%$ (for Black and White version, see page 159).

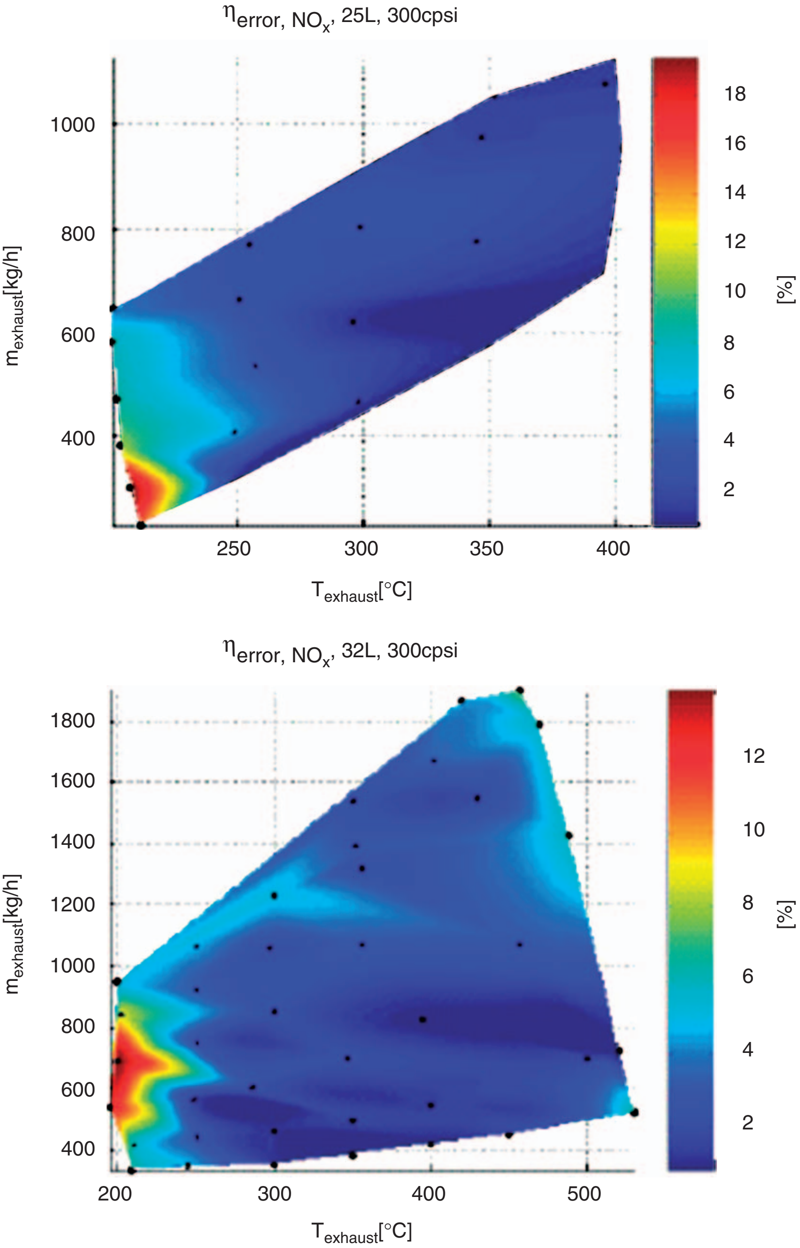

PLATE 6. Mean error for the simulation of the NO_x conversion at steady-state and constant urea dosing conditions as a function of exhausts mass flow and catalyst inlet temperature. Reprinted with permission from SAE Paper # 2005-01-0965 © 2005 *SAE International* (for Black and White version, see page 194).